An organelle with many jobs: Mitochondrial specialization in the retina and RPE

Michelle Marie Giarmarco

A dissertation
submitted in partial fulfillment of the requirements for the degree of

Doctor of Philosophy

University of Washington

2018

Reading Committee:

James B. Hurley, Chair
Susan E. Brockerhoff
Russell N. Van Gelder

Program Authorized to Offer Degree:

Biochemistry

University of Washington

Abstract

An organelle with many jobs: Mitochondrial specialization in the retina and RPE

Michelle Marie Giarmarco

Chair of the Supervisory Committee:

Professor James B. Hurley

Biochemistry

The eye is a complex organ with many tissue and cell types working together to facilitate vision. Photoreceptor cells in the retina initiate vision, converting light into a neuronal signal that is integrated and used to form an image in the brain. These polarized cells have high energy demands that fluctuate with light exposure, and they employ a unique metabolic program to balance energy production and essential anabolic pathways. Neighboring retinal pigment epithelial (RPE) cells and Müller glia cells support photoreceptors with complementary and distinct metabolic programs of their own. Breakdown of these metabolic relationships, and consequent photoreceptor death, is thought to underlie many types of inherited and age-related retinal disease.

We studied metabolic and mitochondrial adaptations in RPE and photoreceptor cells. Using a combination of animal imaging studies and cultured RPE cells, we demonstrated that RPE cells are capable of transporting large amounts of glucose for uptake by the retina. Photoreceptors extract energy from the glucose by converting it to lactate, then they release lactate from the cell. Additionally, we showed that RPE cells

can use lactate to fuel energy production in their mitochondria, which reduces their use of glucose destined for the retina. These findings in the context of recent literature point to distinct metabolic schemes in the RPE and retina. RPE cells have active mitochondria capable of making energy from a wide range of fuels and don't always need to oxidize glucose. Photoreceptors rely heavily on glucose for both immediate energy production and anabolism, but little is known about how these processes are affected by light or subsequently Ca^{2+}. We performed imaging experiments with transgenic zebrafish expressing a fluorescent Ca^{2+} indicator in cones to explore the effects of Ca^{2+} uptake into cone mitochondria. We found that cytosolic Ca^{2+} in cones is separated into two distinct pools on either side of a large dense cluster of mitochondria. In addition to being a potential physical barrier to diffusion of free Ca^{2+}, we found that cone mitochondria take up Ca^{2+} and that this uptake is required to keep the cytosolic pools separate. Ca^{2+} uptake into mitochondria occurs through a uniporter, and could have far-reaching effects on metabolism and other processes necessary for photoreceptor function. Collectively this work highlights some of the mitochondrial adaptations RPE and photoreceptors might employ in a healthy retina. Additionally, a live tissue slice preparation was developed for fluorescent imaging experiments with retinas of zebrafish and mice. This adaptable tool can help answer future questions about metabolism, mitochondrial dynamics, and signaling in the retina.

Table of Contents

List of Figures

Glossary

$[Ca^{2+}]_{ex}$: extracellular Ca^{2+} concentration
$[Ca^{2+}]_{i}$: intracellular Ca^{2+} concentration
$[Ca^{2+}]_{m}$: mitochondrial matrix Ca^{2+} concentration
2-NBDG: (2-(*N*-(7-Nitrobenz-2-oxa-1,3-diazol-4-yl)Amino)-2-Deoxyglucose)
Ca^{2+}: calcium ion
CB: cell body
CNG: cyclic-nucleotide gated
cyto-GCaMP: cone cytosolic Ca^{2+} sensor GCaMP3
cyto-GFP: cone cytosolic GFP
ER: endoplasmic reticulum
ER-GFP: cone endoplasmic reticulum targeted GFP
GAP: glyceraldehyde-3-phosphate
GAPDH: glyceraldehyde-3-phosphate dehydrogenase
GC-MS: gas chromatography-mass spectrometry
GCL: ganglion cell layer
GFAP: glial fibrillary acidic protein
GFP: green fluorescent protein
Glc: glucose
GLUT: glucose transport protein
gnat2: cone transducin alpha promoter (also TαCP)
GS: glutamine synthetase
hfRPE: human fetal RPE
IB: immunoblot
IHC: immunohistochemistry
INL: inner nuclear layer
IPL: inner plexiform layer
IS: inner segment
Lac: lactate
LDH: lactate dehydrogenase
mEC: mouse eyecup
MGC: Müller glia cell
mito-cpYFP: cone mitochondrially targeted circularly-permuted YFP
mito-GCaMP: cone mitochondrially targeted Ca^{2+} sensor GCaMP3
MT-COX1: mitochondrial cytochrome C oxidase

mtDNA: mitochondrial DNA
mRetina: mouse retina
NCKX: plasma membrane Na^+/K^+-Ca^{2+} exchanger
NCX: plasma membrane Na^+/Ca^{2+} exchanger
Nrl: neural retina-specific leucine zipper promoter
ONL: outer nuclear layer
OPL: outer plexiform layer
OS: outer segment
PDE6: generic symbol for photoreceptor cyclic GMP phosphodiesterases
PDE6c: cone phosphodiesterase subunit
PI: propidium iodide
PK: pyruvate kinase
PKM2: pyruvate kinase isoform M2
PMCA: plasma membrane Ca^{2+}-ATPase
PR: photoreceptor
Pyr: pyruvate
Rlbp: retinaldehyde binding protein promoter
RPE: retinal pigment epithelium
SD: standard deviation
SE: standard error of the mean
SEM: scanning electron microscopy
SERCA: sarco/endoplasmic reticulum Ca^{2+}-ATPase
TαCP: cone transducin alpha promoter (also gnat2)
TCA: tricarboxylic acid
tdTomato: tandem dimeric tomato fluorescent protein
Tg: transgenic
Trβ2: thyroid hormone receptor beta 2 promoter
YFP: yellow fluorescent protein

Acknowledgments

Great advisors make graduate school an experience that is transformative beyond a mere research project. The open door and practical advice of Jim Hurley have been instrumental in my growth as a scientist, communicator, and person. Susan Brockerhoff's thoughtful guidance helped me gain a deeper understanding and appreciation for photoreceptor mitochondria. My thesis committee (Russell Van Gelder, Suzanne Hoppins, John Scott, and Bertil Hille) provided useful experimental ideas and mind-opening discussions. Trisha Davis and Erin Kirschner's dedicated work in the Biochemistry department have created a welcoming and open environment for trainees.

A larger community of scientists has bolstered this work with generous contributions of time and brain power. Conversations with Jianhai Du, Eva Ma, Ralph Nelson, Ashley George, Sara Hayden, Ken Lindsay, Jennifer Chao, Abbi Engel, Chris Farnsworth, the lab of David Raible, and Seattle Zebrafish Club inspired several experiments. Stanley Kim and Jeanot Muster in the UW SLU aquatics facility provided dutiful daily care to the animals used in this study. In the UW Vision Core (directed by Maureen Neitz), Ed Parker, Dan Possin, Jing Huang, and Dale Cunningham provided experimental assistance and jokes. I was fortunate to work with many talented undergraduate researchers and technicians in the Hurley and Brockerhoff labs: Gail Stanton, Stephanie Sloat, Jack Zhang, Connor Jankowski, Benjamin Bauer, Ashlee Evans, Vincent Mak, William Ge, and Brian Robbings. Thanks to the next generation of Hurley lab trainees – Mark Kanow, Rachel Hutto, Kristine Tsantilas, and Celia Bisbach – for the great insights and for keeping the retina metabolism spark alive. Critically, friendships with Whitney Cleghorn and Jon Linton kept me sane both at and away from the bench.

My family has been endlessly supportive of my lengthy education, and the early encouragement of Kent Littleton and Esmaeel Naeemi especially shaped my academic development. My sisters blessed me several times over with nieces and nephews whose smiles have shined a bright light during grad school. I am immensely grateful to a wide network of friends in Seattle and beyond for all that we've shared during my academic career. Finally, thanks to Noah for enriching my life continuously with music, adventure, and laughter.

Dedication

To Grammie Marie,
Here's a few pages you never got to read.

Chapter 1

Introduction

The retina and photoreceptors

Eyes provide our windows into the world, and vision is facilitated by an ocular tissue called the retina. The retina lines the inside of the eye and in vertebrates contains millions of highly organized cells with dozens of diverse roles (Figure 1.1A) (Dowling, 1987). Light is captured by specialized neurons called photoreceptors, which have structures dedicated to converting photons into an electric and chemical signal. This signal is relayed to interneurons called bipolar cells, and then onto ganglion cells whose axons form the optic nerve. At each relay step in the retina, horizontal and amacrine cells respectively provide feedback and encode the information that leaves the eye through the optic nerve. The optic nerve projects to visual regions of the brain, where information from both retinas is decoded and integrated into the perception of an image.

Two types of photoreceptors absorb photons to initiate the visual responses that lead to this perception: rods, which facilitate vision under dim light conditions, and cones, which enable vision in bright light and discernment of colors. Both types of photoreceptor share a polarized morphology (Figure 1.1B). Light is captured at the outer segment (OS), stacks of renewable membranous disks which house the machinery needed for phototransduction. The inner segment (IS) contains a dense cluster of mitochondria directly below the OS, an extensive network of endoplasmic reticulum (ER), and the nucleus. At the synapse, vesicles containing the neurotransmitter glutamate are released from an intricate ribbon structure onto downstream bipolar cells. Rods and cones differ in the shape and organization of their OS, as well as in their phototransduction machinery. For example, rods use a protein called rhodopsin to very sensitively capture photons; cones use similar opsin proteins to capture photons from specific colors of light.

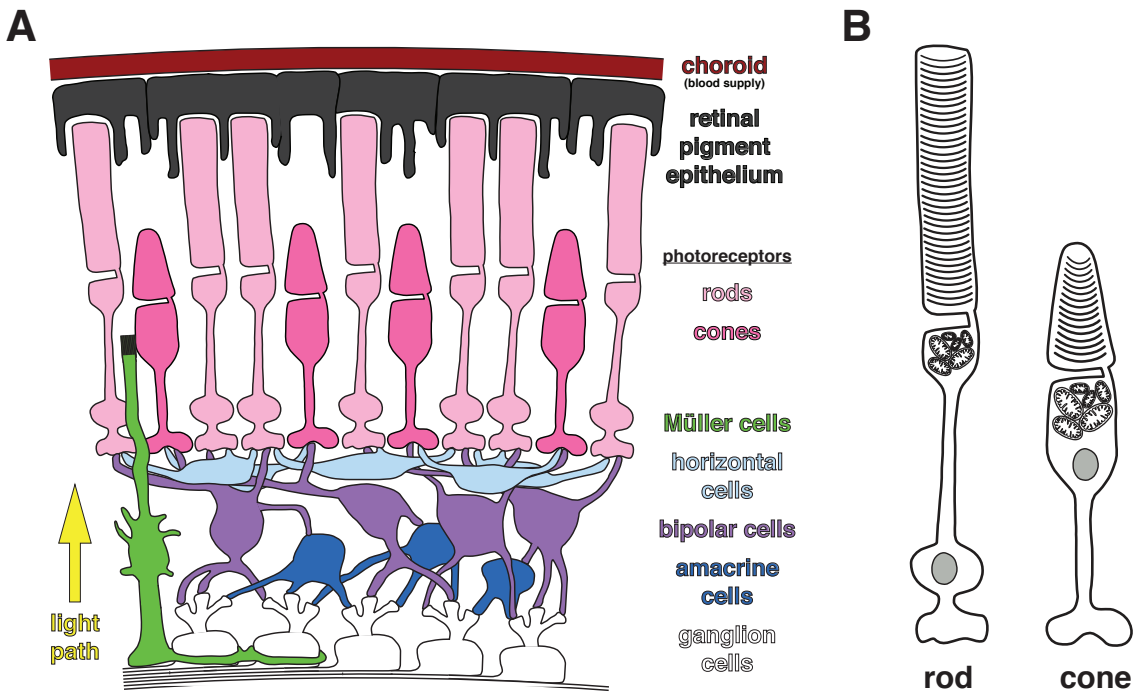

Figure 1.1. Schematics of the vertebrate retina (A) and photoreceptors (B).

Several other types of cells support photoreceptors. The retina pigment epithelium (RPE) is a tight monolayer of polarized, pigmented cells adjacent to photoreceptors that directly support phototransduction (Strauss, 1995). The pigment absorbs scattered photons, which improves visual fidelity and mitigates light-induced damage to neurons. Further, the RPE forms a barrier between the blood supply and retina, and at light onset RPE cells engulf and degrade the oldest OS disks (LaVail, 1976). (Note: In some literature the term *retina* includes both the neurosensory retina and the RPE; in this work *retina* refers specifically to the neurosensory retina.) In the retina, large Müller glia cells (MGCs) span across several retinal layers and serve vital roles in nutrient synthesis, pH balance, and responses to retinal damage (Vecino et al., 2015). MGCs make intimate contacts with photoreceptor IS and synapses, and in some fish species MGCs can de-differentiate and become photoreceptors following photoreceptor loss (Lenkowski and Raymond, 2014).

All healthy photoreceptors are capable of renewing their OS disks, but photoreceptors of most species including humans are terminally differentiated and cannot be easily

regenerated if the cell dies. Photoreceptor health is paramount to human vision, and hundreds of mutations affecting photoreceptor development, structure or function are associated with heritable blindness (Hanein et al., 2004; Phelan and Bok, 2000; Rattner et al., 1999). In some blinding diseases only one type of photoreceptor (i.e. rods or cones) is affected, but eventually nearby healthy cells also sicken and die (Aït-Ali et al., 2015; Punzo et al., 2009). To develop strategies to preserve these healthy photoreceptors, we must first understand how photoreceptors function normally in a retina in the context of neighboring cells.

Zebrafish as a model organism to study the retina

The progression and prevention of blinding diseases in a living eye cannot be studied using retinas cultured in a dish. In even the best culture conditions the eye's natural nutrient delivery system breaks down, and retinal cells lose their unique identities and eventually die. Thus, model organisms are necessary to meaningfully study the retina. Mice (Chang et al., 2002), rats (Mullen and LaVail, 1976), non-human primates (Dowling and Boycott, 1966) and even pigs (Wang et al., 2016) have been used as model organisms in vision research, sharing a similar retinal organization common to all vertebrates. However, retinas of these animals are enriched >90% with rods, which hampers the study of cones. In recent years zebrafish, whose retinas are enriched ~70% with cones (Raymond et al., 2014), have emerged as a tractable model for vision research particularly in cones (Brockerhoff et al., 1998; Lieschke and Currie, 2007).

Like other vertebrates, zebrafish share the retinal organization and cell morphology depicted in Figure 1.1. However, unlike in mammalian retinas MGCs can dedifferentiate to replace photoreceptors if the retina is damaged (Lenkowski and Raymond, 2014). Zebrafish are easily and inexpensively reared and develop rapidly with a fully-formed stereotypical vertebrate retina at 4 days of age (Fadool, 2003). Additionally, they are amenable to transgenesis (Kwan et al., 2007) and can be rendered transparent via chemical (Karlsson et al., 2001) or genetic (Antinucci and Hindges, 2016) means.

These features combined with genetically encoded fluorescent biosensors have made zebrafish a useful tool to examine the effects of Ca^{2+} (Ma et al., 2013), hydrogen peroxide (Niethammer et al., 2009), apoptotic activation (Andrews et al., 2016) and ATP (Kioka et al., 2014) in a living organism. This is especially valuable for studying heterogeneous tissues such as the retina, where effects from a small subset of cell types may be overlooked in experiments done using traditional biochemical methods. Instead, individual cells can be targeted for imaging studies to determine how specific cell types behave in a complicated milieu.

Ca^{2+} roles and handling in photoreceptors

Ca^{2+} ions are critical for relaying signals in nearly all cells, and in photoreceptors they also play a key role in phototransduction. In darkness, Ca^{2+} and Na^{+} ions constantly flow through the cell; Ca^{2+} stimulates their influx through cyclic nucleotide-gated (CNG) channels in the OS (Dizhoor, 2000; Kawamura and Murakami, 1991). This depolarized signal is transduced to the IS, where L-type voltage gated Ca^{2+} channels facilitate further Ca^{2+} influx locally which ultimately stimulates synaptic vesicle release (Thoreson et al., 2004). In light, phototransduction results in closure of CNG channels in the OS, net extrusion of Ca^{2+}, hyperpolarization of the plasma membrane and cessation of synaptic activity. Concentrations of Ca^{2+} in the OS are estimated to be 10-20 times higher in darkness than in light (Krizaj and Copenhagen, 2002).

Photoreceptors use an elaborate system of ion channels and pumps across membranes of several organelles to tightly regulate Ca^{2+} levels. As part of the light response, plasma membrane ion exchangers for Na^{+}/Ca^{2+} (NCX) and Na^{+}/K^{+}-Ca^{2+} (NCKX) rapidly extrude Ca^{2+} from the IS and OS, respectively, and the Ca^{2+}-ATPase (PMCA) extrudes Ca^{2+} at the synapse (Krizaj and Copenhagen, 1998). Complicated networks of ER and mitochondria help to sequester and release additional cytosolic Ca^{2+}. It is thought that the ER mediates Ca^{2+} signaling between the IS and the synapse (Chen et al., 2015; Van Hook and Thoreson, 2014), while mitochondria buffer high levels of OS Ca^{2+} from the rest of the cell (Giarmarco et al., 2017; Szikra and Krizaj, 2007). Ca^{2+} concentration

is so closely controlled in photoreceptors that it can stabilize even as the cell dies from a genetic defect in phototransduction (Ma et al., 2013).

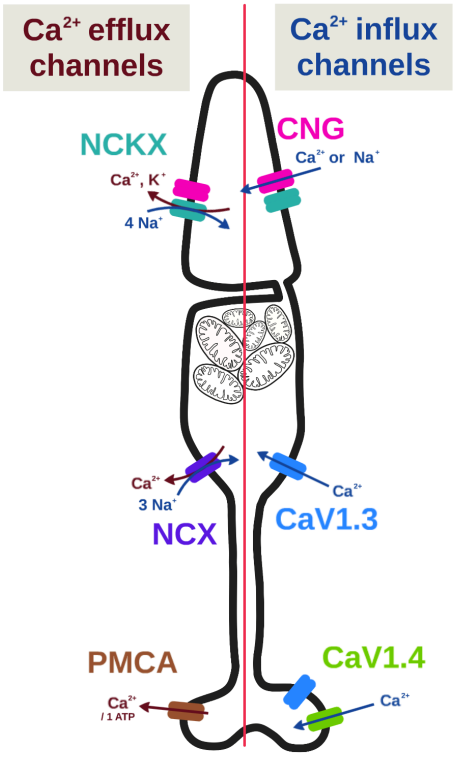

Figure 1.2. Schematic of plasma membrane Ca^{2+} channels on a cone photoreceptor. Left: efflux channels Na^+/K^+-Ca^{2+} exchanger (NCKX), Na^+/Ca^{2+} exchanger (NCX), and Ca^{2+}-ATPase (PMCA). Right: influx cyclic nucleotide-gated (CNG) and L-type voltage gated (CaV1.3 and CaV1.4) Ca^{2+} channels.

In most cells Ca^{2+} has far-reaching effects on gene expression and viability, but also very specific effects on organelles. For example, Ca^{2+} can directly stimulate mitochondrial energy production by increasing activity of enzymes in the TCA cycle (Wan et al., 1989) and shuttling NADH equivalents into mitochondria to fuel the electron transport chain (Contreras et al., 2007). In the ER Ca^{2+} mediates protein sorting (Booth and Koch, 1989) and trafficking (Beckers and Balch, 1989), and Ca^{2+} can be transferred between ER and mitochondria at contact sites (Csordás et al., 2010). Ca^{2+} overload of ER and mitochondria is a critical trigger for cell death (Orrenius et al., 2003). In photoreceptors it is not fully understood how Ca^{2+} regulates these processes, or how extensive ER-mitochondrial contacts may be.

Metabolism in the retina and RPE

Phototransduction, maintaining ion gradients, and OS disk and synaptic vesicle synthesis and cycling put unique energetic strains on photoreceptors. It has been suggested that photoreceptors consume more ATP than any other type of cell (Laughlin et al., 1998), and that retinas consume more ATP in darkness than in light (Okawa et al., 2008). Glucose is the most important fuel for making ATP in the retina (Hurley et al., 2015), and it enters cells in the retina and RPE through glucose-specific transport proteins called GLUTs (Gospe et al., 2010; Mantych et al., 1993; Takagi et al., 1994).

In all vertebrate retinas, glucose is supplied by a blood vessel called the choriocapillaris at the outer retina adjacent to the RPE (Figure 1.1). The RPE helps to form a blood-retina barrier, and closely controls what molecules or ions reach the retina (Ennis et al., 1982; Törnquist et al., 1990). GLUTs on RPE cells translocate glucose from the choriocapillaris, through the cytosol, and out into the retina (Lehmann et al., 2014; Rizzolo, 2008). The retina creates a sink for glucose, facilitating its export from RPE cells down a concentration gradient (Adler and Southwick, 1992).

Once in the cell, glucose can be metabolized in two ways to make ATP (see Figure 1.3): aerobically – using oxygen to completely oxidize glucose and make a large amount of energy – and anaerobically – incompletely oxidizing glucose in glycolysis to make a small amount of energy without oxygen. In the 1920s, Warburg and Krebs observed that retinas, like cancer cells, rely heavily on glycolysis even when oxygen is abundant (Krebs, 1927; Warburg et al., 1924). "Aerobic glycolysis" is a metabolic scheme (Figure 1.3B) where most glucose is converted to lactate; NADH is used to make some ATP in the electron transport chain, and pools of pyruvate and other intermediates can be used as molecular building blocks. Most glucose that reaches a retina undergoes aerobic glycolysis and is converted to lactate which can be exported from cells (Ames et al., 1992; Winkler et al., 2008). Retinas lacking photoreceptors make less lactate (Du et al., 2016a), but there is debate about whether MGCs are also a source of lactate (Poitry-Yamate et al., 1995).

Photoreceptors have high ATP demands and active mitochondria, but aerobic glycolysis is a relatively inefficient way to produce ATP (Figure 1.3). Several factors may contribute to aerobic glycolysis in photoreceptors. Pyruvate and intermediates from glycolysis can be used in biosynthetic pathways needed to make lipids and proteins for new OS discs (Chinchore et al., 2017). Converting glucose to lactate generates NADH that may aid synthesis of purine nucleotides needed for phototransduction (Du et al., 2013b). Secreting lactate may also increase the amount of glucose that reaches photoreceptors (Kanow et al., 2017) due to a unique metabolic relationship with the RPE.

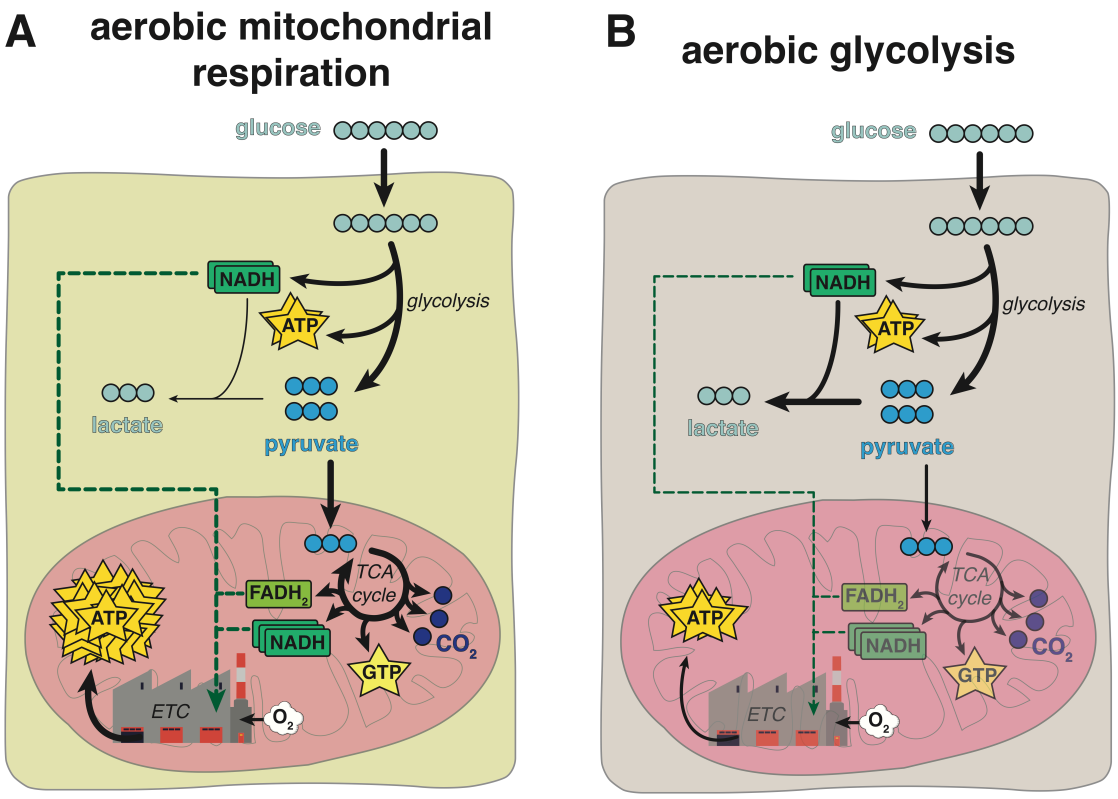

Figure 1.3. Overviews of aerobic mitochondrial respiration (A) and aerobic glycolysis (B). In aerobic mitochondrial respiration (A), pyruvate from glycolysis is fully oxidized in mitochondria to generate reducing equivalents to feed the electron transport chain and make large amounts of ATP. In aerobic glycolysis (B), most pyruvate is instead converted to lactate, which generates some NADH and subsequently ATP. Circles represent carbon atoms with darker blue carbons being more oxidized; stars represent energy-carrying molecules; green boxes represent reducing equivalents.

While photoreceptors get most of their ATP from aerobic glycolysis, RPE cells rely more on mitochondrial respiration to produce ATP using glucose, lactate or amino acids as fuels (Figure 1.3A) (Chao et al., 2017; Kanow et al., 2017). The OS discs engulfed daily by RPE cells also provide a pool of energy-rich fatty acids that can be oxidized by mitochondria (Reyes-Reveles et al., 2017). In comparison, photoreceptors rely more anaerobic glycolysis for anabolism (Chinchore et al., 2017), a paradigm that points to fundamental differences in RPE and photoreceptor mitochondria.

Mitochondria and human retinal disease

Mitochondria in the RPE and retina have adapted to favor distinct metabolic pathways that uniquely couple energy production and cellular function. Photoreceptors perform glycolysis to make NADH and pyruvate, but only about 5% of the pyruvate is used along with NADH to make ATP in mitochondria (Figure 1.3B) (Wang et al., 1997a; Winkler et al., 2008). However, even this small amount of pyruvate can produce about half of the cell's ATP (Ames et al., 1992) because mitochondrial respiration is so much more efficient than glycolysis at producing ATP. RPE cells rely more on canonical mitochondrial respiration (Figure 1.3A) through the oxidation of fuels like glucose, lactate, amino acids and fatty acids (Chao et al., 2017; Kanow et al., 2017; Reyes-Reveles et al., 2017). Metabolic disruptions in even a subset of retinal cells can result in metabolic crises in neighboring cells (Aït-Ali et al., 2015), cell death and ultimately blindness.

Mitochondrial diseases make up a broad class of disorders that commonly manifest in muscular, cardiac, and/or visual abnormalities. Mutations in genomic DNA which affect important mitochondrial pathways such as the electron transport chain or mitochondrial DNA (mtDNA) synthesis are associated with several optic atrophies (Scharfe et al., 2009). Deletions or duplications in mtDNA itself are associated with vision disorders like Kearns-Sayre syndrome, Leber hereditary optic neuropathy, and retinitis pigmentosa (Lefevere et al., 2017). Mitochondrial impairment makes cells more glycolytic (Schon et al., 2012); if RPE become more glycolytic less glucose may reach the retina and the neurons starve (Kurihara et al., 2016; Zhao et al., 2011a).

Without an efficient proofreading enzyme, mutations in mtDNA can accumulate throughout life, and are thought to contribute to some forms of age-related macular degeneration (AMD) by impairing mitochondrial respiration in RPE cells (SanGiovanni et al., 2009; Terluk et al., 2015). Antioxidants and mitochondrial viability factors mitigate RPE cell death in an AMD model (Nashine et al., 2017), but it is unknown how these factors affect metabolism in the context of an eye. The study of mtDNA mutations in

AMD is complicated by mitochondrial heteroplasmy and confounding genomic DNA mutations (Ferrington et al., 2016).

Restoring the delicate metabolic balance between the retina and RPE has been suggested as a broad therapy for many types of retinal diseases affecting mitochondria either directly or indirectly. Photoreceptor starvation is a hallmark of many retinal degenerative diseases (Punzo et al., 2009), and in model organisms it can be delayed by supplying exogenous glucose (Wang et al., 2016) or enhancing glycolysis in photoreceptors (Venkatesh et al., 2015; Zhang et al., 2016). Conversely, stimulating glycolysis (Kurihara et al., 2016) or impairing mitochondrial respiration (Zhao et al., 2011a) in RPE cells causes photoreceptors to degenerate. Together these studies suggest that unique mitochondrial populations and metabolic relationships between RPE and photoreceptor cells are necessary for retinal health.

Chapter 2

Biochemical adaptations of the retina and retinal pigment epithelium support a metabolic ecosystem in the vertebrate eye

Introduction

Mutations in any of more than 140 genes can cause photoreceptors in a vertebrate retina to degenerate (Bramall et al., 2010). Much has been gained by studying those genes and specific therapeutic strategies based on their functions are being developed (Sengillo et al., 2017). However, the biochemical diversity of those genes also suggests that the consequences of their loss or gain of function may converge onto a few essential metabolic processes (Punzo et al., 2009; Zhang et al., 2016). A more general understanding of what photoreceptors need to survive could lead to broadly applicable therapeutic strategies. With that in mind, we have been investigating the fundamental nature of energy metabolism in the retina and in the retinal pigment epithelium (RPE) (Du et al., 2013a; 2013b; 2016a; 2015; 2016b; Lindsay et al., 2014; Linton et al., 2010).

The sugar glucose fuels the outer retina and comes from the choroidal blood, but it first must traverse the RPE. The RPE is a monolayer of polarized cells between the choroid and retina that functions as a blood-retina barrier. RPE cells, bound together by tight junctions, express specific transporter proteins on their opposing basolateral and apical surfaces (Lehmann et al., 2014). Glucose from the choroid enters RPE cells through transporters on the basolateral surface. If metabolic enzymes within the RPE cell do not consume it, the glucose moves down a concentration gradient toward the apical surface and exits through transporters to the retina.

Most glucose that reaches the retina is consumed in glycolysis and converted to lactate. In the 1920's Warburg and Krebs identified both retinas and tumors as relying mostly on 'aerobic glycolysis' (Krebs, 1927; Warburg et al., 1924), a type of metabolism that converts glucose to lactate even when O_2 is available (Figure 1.3B). Photoreceptors in the outer retina are the likeliest site of aerobic glycolysis (Chinchore et al., 2017; Du et

al., 2016a; Lindsay et al., 2014; Medrano and Fox, 1995; Wang et al., 1997b; Winkler, 1981). The importance of aerobic glycolysis for photoreceptor survival and function is not yet clear, but it is thought to support anabolic activity (Chinchore et al., 2017; Rajala et al., 2016; Rueda et al., 2016; Venkatesh et al., 2015; Zhang et al., 2016).

Energy metabolism in RPE cells is strikingly different from photoreceptors. RPE cells are specialized for a type of mitochondrial energy metabolism called reductive carboxylation (Du et al., 2016b) that can support redox homeostasis. The reliance of RPE on mitochondrial metabolism is in contrast to aerobic glycolysis in photoreceptors, and this motivated us to directly compare the metabolic features of retina and RPE.

Recent reports used genetic manipulations to qualitatively alter energy metabolism either in photoreceptors or in RPE cells *in vivo*. In one study, glycolysis in rods was enhanced by blocking expression of SIRT6 (Zhang et al., 2016). Another study enhanced glycolysis in cones by activating mTORC1 (Venkatesh et al., 2015). Both found that more glycolytic photoreceptors are more robust; degeneration of photoreceptors was delayed in retinas afflicted by a mutation associated with retinitis pigmentosa (Venkatesh et al., 2015; Zhang et al., 2016). In contrast, when glycolysis in RPE cells was enhanced by knocking out VHL (Kurihara et al., 2016) or by knocking out an essential mitochondrial transcription factor (Zhao et al., 2011a), the neighboring photoreceptors died.

These *in vivo* findings are seemingly contradictory when considered only from a cell autonomous perspective. Why does enhancing glycolysis benefit some cells and endanger others? Here we propose a context for those findings: the retina and RPE function as a metabolic ecosystem. We show that photoreceptors are the primary cells in the retina that take up glucose. Photoreceptors convert glucose to lactate, which then fuels neighboring cells in the retina. We report that lactate can suppress glycolysis in RPE cells, protecting glucose so that more of it can reach the retina. Based on this evidence, we propose a model in which each cell of the retina and RPE performs an essential metabolic function that promotes survival of the retina-RPE ecosystem.

Results

Photoreceptors express a glucose transporter.

Cells need a membrane protein to take up glucose, so we evaluated expression of glucose transporters in mouse tissues using immunoblot (Figure 2.1A). Consistent with previous findings (Badr et al., 2000; Gospe et al., 2010) we found that retina and RPE express GLUT1, and confirmed that the protein immunoreactive with the GLUT1 antibody is membrane associated (Figure 2.1B). GLUT3 was detected only in brain. GLUT4 was detected in heart and muscle as expected, but not in the retina.

Immunohistochemistry (IHC) of mouse retinas shows that GLUT1 immunoreactivity overlaps with cytochrome oxidase subunit 1 (MT-COX1) (Figure 2.1C), which identifies rod inner segments by the unique elongated shape of their mitochondria (Figure 2.1E). We examined the ultrastructure of this region using serial block face scanning electron microscopy (SEM), which revealed that rod mitochondria extend beyond the ends of the Müller glial cell (MGC) apical processes (Figure 2.1E). These fine structures are devoid of mitochondria, and small spherical mitochondria line up within the MGCs along the outer limiting membrane, just beneath the apical processes (Figure 2.1F and arrowheads in Figure 2.1C).

To visualize MGCs specifically, we labeled them with an antibody to glutamine synthetase (GS) in Figure 2.1D. These long cells extend from the outer limiting membrane to the ganglion cells (see Figure 1), and dual labeling showed that most GLUT1 immunoreactivity in MGCs is in the inner retina (Figure 2.1D). GLUT1 immunoreactivity also overlaps with a marker specific for rod photoreceptors, rod arrestin (Figure 2.1G), and with GFP expressed from the rod-specific Nrl promoter (Figure 2.1H). The distribution of GLUT1 immunoreactivity supports the idea that photoreceptors can take up glucose released from the apical side of the RPE.

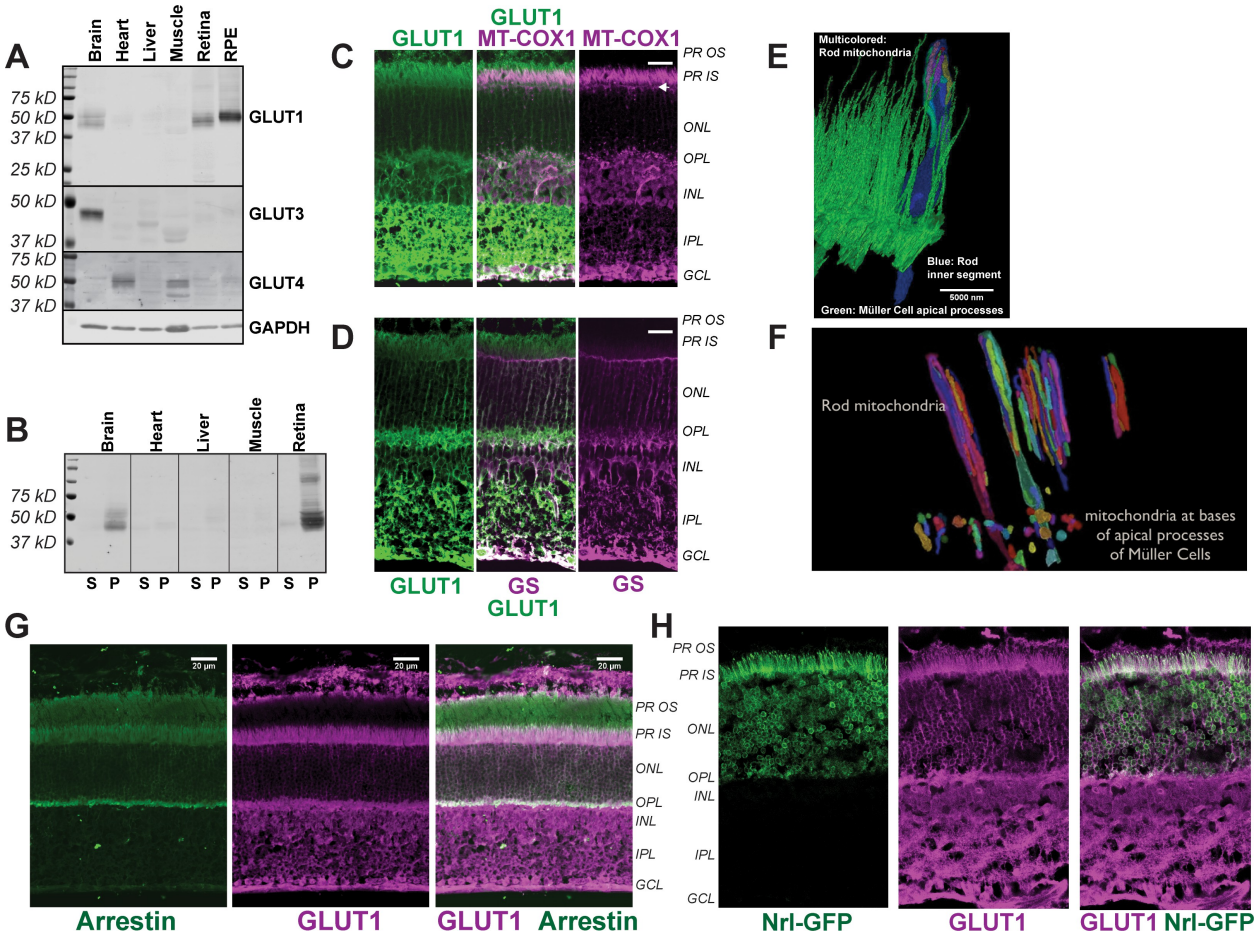

Figure 2.1. Distribution of GLUT1 in retina. (A) Immunoblot analysis of mouse tissue homogenates confirms GLUT1 is a major glucose transporter in retina and RPE. 1 mg protein was loaded per lane. No antibodies that we could validate were available for GLUT2; the Human Protein Atlas reports no GLUT2 mRNA transcripts in retina (Uhlén et al., 2015). The blot shown is representative of 3 experiments. (B) Evidence that the protein immunoreactive with the GLUT1 antibody is membrane associated. Equivalent percentages of total supernatant (S) and total pellet (P) were probed with the GLUT1 antibody. (C) GLUT1 immunoreactivity in mouse retina. Rod inner segments are identified by their mitochondria labeled with mitochondrial cytochrome oxidase antibody (MT-COX1). White arrowhead indicates the layer of MGC mitochondria. (D) MGCs identified by glutamine synthetase (GS) immunoreactivity. (E) Serial block face SEM of mouse retina. The inner segment of one rod cell is shown in blue with its mitochondria multi-colored; green structures are MGC apical processes. (F) Differences in rod and MGC mitochondrial in mouse retina, with small MGC mitochondria located just below the outer limiting membrane. For clarity not all of the mitochondria are shown. (G) Distributions of rod arrestin and GLUT1 in a partially light-adapted mouse retina. (H) Distributions of GLUT1 and GFP expressed from the rod-specific Nrl promoter. PR OS, photoreceptor outer segment; PR IS photoreceptor inner segment; ONL, outer nuclear layer; OPL, outer plexiform layer; INL inner nuclear layer; IPL inner plexiform layer; GCL, ganglion cell layer. Scale bars in C, D and G represent 20 µm.

Dietary glucose enters the retina primarily through photoreceptors.

To determine which retinal cells take up glucose in an eye of a living animal, we used oral gavage to introduce a fluorescent derivative of 2-deoxy glucose (2-NBDG) (Yoshioka et al., 1996) into stomachs of mice. We harvested the retinas either 20 or 60 min after gavage, mounted them on filter paper, and cut 300–400 μm slices for imaging by confocal microscopy (Giarmarco et al., 2017; 2018). 2-NBDG fluorescence is strongest in the photoreceptor layer (Figure 2.2A), and surprisingly stronger in the outer retina than in the inner retina even though mouse inner retinas are vascularized. 2-NBDG fluorescence does not overlap with MGCs, visualized by transgenic expression of tdTomato (Wohl and Reh, 2016), though in rare instances there was overlap at MGC end feet. The results summarized and quantified in Figure 2.2C show that glucose reaching the outer retina is taken up primarily by photoreceptors.

The images in Figure 2.2A are of live unfixed mouse retinas where most of the photoreceptors are rods. To resolve whether cones also import 2-NBDG, we similarly introduced 2-NBDG by oral gavage into adult zebrafish, whose retinas are more enriched with cones (Raymond et al., 2014). 30 min after gavage, cones in a retinal slice are intensely fluorescent (Figure 2.2B). As in mouse retinas, there was little 2-NBDG uptake into MGCs, which in these retinas were marked with tdTomato expressed from a GFAP promoter (Shin et al., 2014). Data quantified in Figure 2.2D indicate that cones can also take up glucose from the blood.

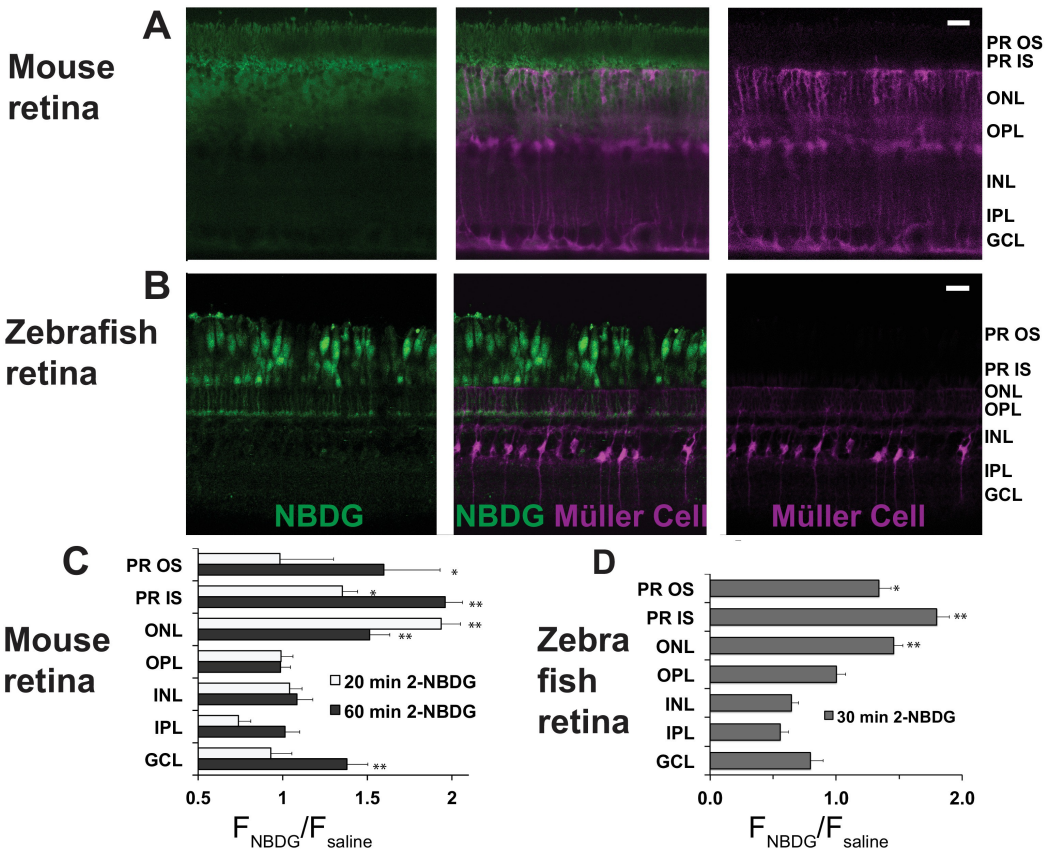

Figure 2.2. Fluorescent glucose (2-NBDG) accumulates in photoreceptors after oral gavage. (A) 2-NBDG (green) accumulation in a mouse retina 20 min after oral gavage. MGCs are identified by tdTomato expression in cells in which the Rlbp1 promoter is active. (B) 2-NBDG accumulation in a zebrafish retina 30 min after oral gavage. MGCs are identified by tdTomato expressed from the GFAP promoter. Labels on the right of panels A and B represent approximate positions of the retinal layers. (C) Quantification of 2-NBDG fluorescence from mouse retinas (n = 5 animals, 17 slices for 20 min 2-NBDG; 3 animals, 8 slices for 1 hr 2-NBDG; 3 animals, 8 slices for saline). F_{NBDG}/F_{saline} compares fluorescence from retinas of mice gavaged with 2-NBDG vs. with saline. Error bars report SE. (D) Quantification of 2-NBDG fluorescence from zebrafish retinas (3 animals, 8 slices for 30 min 2- NBDG; 2 animals, 3 slices for saline). PR OS, photoreceptor outer segments; PR IS, photoreceptor inner segments; ONL, outer nuclear layer; OPL, outer plexiform layer; INL, inner nuclear layer; IPL, inner plexiform layer; GCL, ganglion cell layer. Scale bars represent 20 μm. * indicates $p<0.05$ and ** indicates $p<0.01$ for the comparison of F_{NBDG} to F_{saline}.

Carbons from glucose are metabolized in RPE cells differently than in retina

Most of the glucose taken up into a retina is used to make lactic acid (Du et al., 2016a; Krebs, 1927; Medrano and Fox, 1995; Wang et al., 1997b; Winkler, 1981). In the eye of a living animal, glucose from the choroidal blood first must first pass through the RPE cell monolayer before it can reach the retina. We hypothesized that the energy metabolism of RPE cells might minimize their consumption of glucose, maximizing the amount of glucose passing through to the retina.

To compare glucose metabolism in RPE and retina we initially used two preparations, mouse retina (mRetina) and cultured human fetal RPE cells (hfRPE). The retinas were freshly dissected from mouse eyes. hfRPE cells were grown 4–6 weeks in culture to form a monolayer with tight junctions and a transepithelial resistance similar to native human RPE (>200 Ω*cm^2). Due to its similarity to native RPE cells, this hfRPE preparation has been widely used to study RPE metabolism and to model RPE-related diseases such as age-related macular degeneration (Ablonczy et al., 2011; Adijanto and Philp, 2014; Blenkinsop et al., 2015; Johnson et al., 2011; Sonoda et al., 2009).

We added ^{13}C labeled glucose to both preparations and then used gas chromatography-mass spectrometry (GC-MS) (Du et al., 2015) to compare incorporation of ^{13}C into glycolytic and other intermediates. The pattern of ^{13}C labeling from the [1,2] ^{13}C glucose isotopomer can be used to distinguish metabolites generated by glycolysis versus the pentose phosphate pathway (Metallo et al., 2009). Metabolites with one ^{13}C ('m1') are generated from glucose oxidation in the pentose phosphate pathway, whereas metabolites with two ^{13}C ('m2') are produced when glucose enters glycolysis. In a previous report (Du et al., 2016b) we used [1,2] ^{13}C glucose to show that <2% of metabolic flux from glucose goes through the pentose phosphate pathway in both mRetina and hfRPE.

Consistent with retinal reliance on aerobic glycolysis, total lactate and succinate are more abundant in mRetina than in hfRPE, whereas citrate and a-ketoglutarate are more abundant in hfRPE (Figure 2.3A). In a time course, the initial rate at which ^{13}C from

glucose incorporates into the intracellular pool of lactate is at least eight times faster in mRetina than in hfRPE (Figure 2.3B). Citrate and a-ketoglutarate pools are larger and fill more gradually in hfRPE cells than in retina, indicating a large oxidative metabolic capacity of RPE mitochondria. It is important to note that interpretation of retinal metabolic flux in Figure 2.3 is complicated by the presence of multiple cell types and multiple compartments within each cell type.

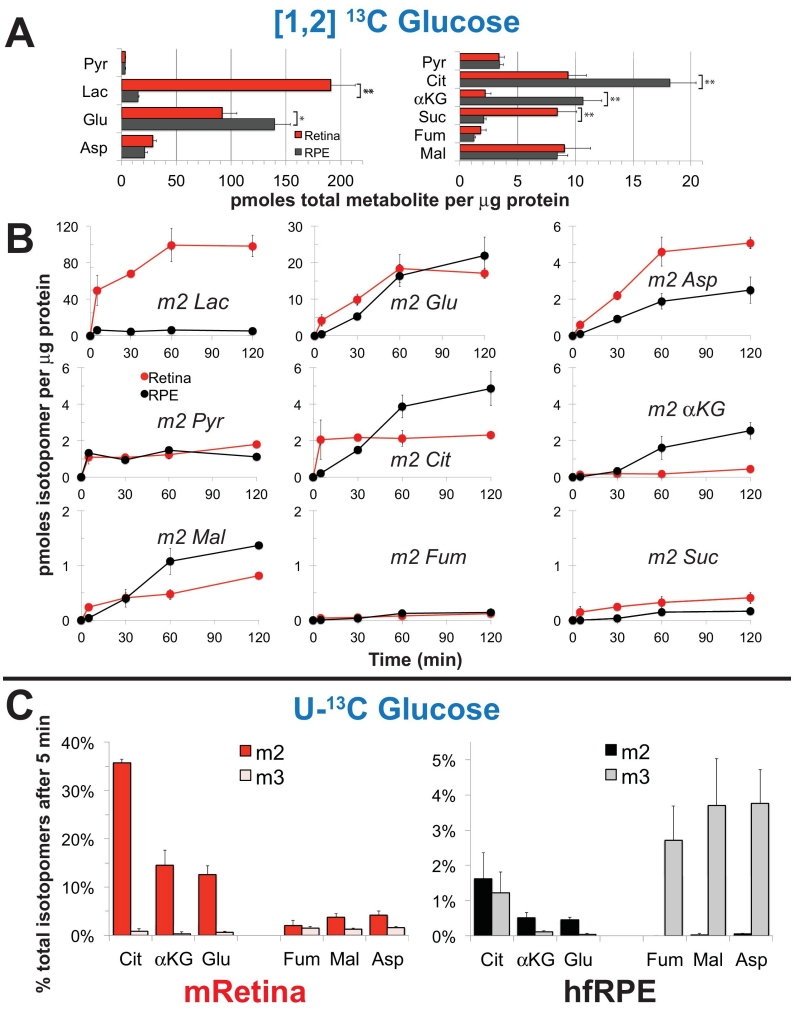

Figure 2.3. Differences in metabolic flux in retina and RPE. (A) Total metabolite levels (pmoles per mg protein) in mRetina (red) and hfRPE (black). Note the different scales for the left and right panels. n = 11; *p<0.05 and **p<0.01. (B) Incorporation of ^{13}C from [1,2] ^{13}C glucose into metabolites in mRetina and hfRPE cells (pmoles per mg protein). Each of the isotopomers shown is derived from glucose metabolized by glycolysis. Note the different scales for the top, middle and bottom panels. (n = 3 for each time point; error bars represent SD) (C) Incorporation in mRetina and hfRPE cells of ^{13}C from 5 mM U-^{13}C glucose into metabolites after 5 min. The % of total isotopomers that are m2 and m3 are shown.

Pyruvate resulting from glycolysis must be decarboxylated to fuel oxidative metabolism in mitochondria. To compare relative rates of pyruvate carboxylation and decarboxylation, we incubated mRetina and hfRPE with U-^{13}C glucose. Mitochondrial intermediates with two ^{13}C ('m2') are produced by decarboxylation of pyruvate, whereas those with three ^{13}C ('m3') are made from carboxylation of pyruvate. (See Figure 2.5B for an overview of these pathways.) Decarboxylation of pyruvate predominates in

mRetina, whereas carboxylation is more prominent in hfRPE (Figure 2.3C), suggesting that retina and RPE cells metabolize glucose differently. RPE cells also use reductive carboxylation an alternative pathway to make NADPH (Du et al., 2016b). We propose that these adaptations minimize consumption of glucose in RPE cells so they can maximize transport of glucose from the choroid to the retina.

Confirmation of metabolic specializations of the retina and RPE in a mouse eye

The cultured hfRPE cell is a well characterized model that has been used to evaluate RPE metabolism (Adijanto and Philp, 2014), as well as to study diseases like age-related macular degeneration (Johnson et al., 2011). *In vitro* studies have focused on cultured hfRPE cells because RPE cells isolated from adult eyes can de-differentiate in culture. However, cultured adult human RPE is not better than hfRPE as a representation of native RPE (Blenkinsop et al., 2015) in terms of transepithelial resistance and gene expression. hfRPE cultures used in this study are of a similar age in culture as those in other published studies.

Nevertheless, it is important to confirm that the metabolic differences between mRetina and hfRPE reported in Figure 2.3 reflect bona fide differences between retina and RPE in an eye. We performed metabolic analyses using isolated mRetina and a mouse eyecup (mEC) preparation in which the RPE remained intact after the retina was removed. Although the choroid and sclera are included in the mEC, the RPE layer is more metabolically active than the sclera and it is accessible to added metabolites. We incubated freshly separated retinas and mECs in medium containing glucose, then analyzed metabolites by GC-MS. The total lactate/citrate ratio in mRetina is nearly 30 times higher than in mEC (Figure 2.4A), similar to the comparison of mRetina and hfRPE.

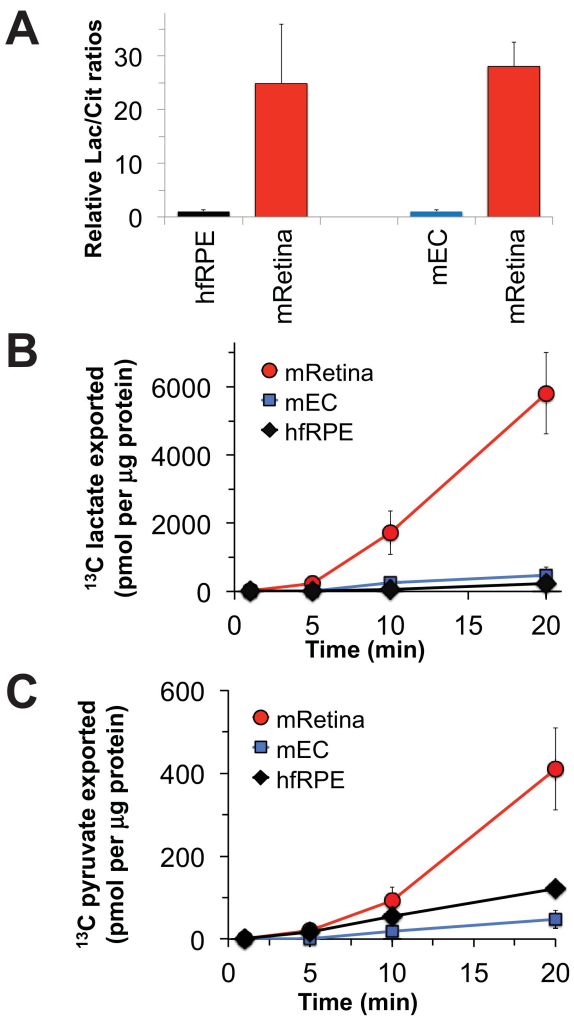

Figure 2.4. Comparisons of metabolic flux in mouse retina (mRetina), mouse eyecup (mEC), and human fetal RPE (hfRPE). (A) Ratios of total intracellular lactate/citrate in both hfRPE and mEC are about 1/25 of the lactate/citrate ratio in mRetina. (B) Accumulation of m3 ^{13}C lactate in the medium in which either mRetina (n = 4), mEC (n = 4) or hfRPE (n = 3) were incubated with 5 mM U-^{13}C glucose. (C) Accumulation of m3 ^{13}C pyruvate in the media in which either mRetina (n = 4), mEC (n = 4) or hfRPE (n = 3) were incubated with 5 mM U-^{13}C glucose. Error bars report SE.

The data shown in Figure 2.3 and 2.4A report the amounts of intracellular metabolites, but metabolites made from glucose, most notably lactate, could be exported to the medium. To quantify exported metabolites, we incubated mRetinas, mECs and hfRPE cells with U-^{13}C glucose and used GC-MS to quantify ^{13}C labeled lactate and pyruvate as they accumulated in the medium (Figures 2.4B, 2.4C). mRetinas, hfRPE cells and mECs exported ^{13}C lactate and ^{13}C pyruvate, but mRetina releases ^{13}C lactate into the medium ~20 times faster than either hfRPE or mEC.

RPE cells can use lactate as a fuel

We previously confirmed that mouse retinas convert glucose into lactate (Du et al., 2016a) and retinas release more lactate than other neuronal tissues (Du et al., 2013b). Figures 2.3 and 2.4 in this report show that mouse retinas produce and release more lactate than RPE cells. To determine if RPE cells are capable of using lactate exported

from a retina as an alternative fuel, we incubated hfRPE cell monolayers with either 5 mM U-^{13}C glucose or 10 mM U-^{13}C lactate/1 mM unlabeled glucose. After 5 or 10 min, incorporation of ^{13}C into metabolites was quantified with GC-MS. hfRPE cells incorporate ^{13}C rapidly into pyruvate from both ^{13}C glucose and ^{13}C lactate (Figure 2.5A). However, ^{13}C from lactate accumulates at least 20 times faster into citrate pools than ^{13}C from glucose. Substantial amounts of 'm3' labeled malate (Figure 2.5B) confirm that pyruvate carboxylation is a major metabolic pathway in hfRPE.

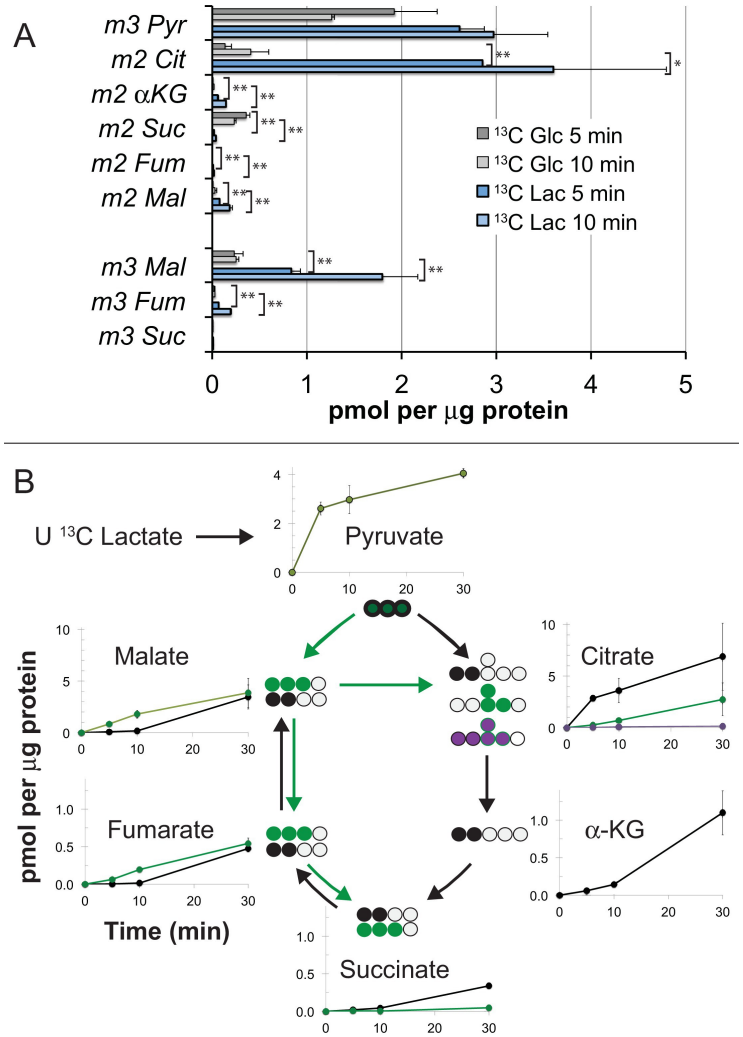

Figure 2.5. Incorporation of ^{13}C from lactate into metabolic intermediates in hfRPE cells. (A) Comparison of initial rates of labeling (at 5 and 10 min after introduction of labeled fuel) from 5 mM U-^{13}C glucose vs. from 10 mM U-^{13}C lactate (with 1 mM unlabeled glucose also present). Citrate and malate take up label faster from lactate than from glucose. (B) Time courses of incorporation of ^{13}C from 10 mM U-^{13}C lactate (with 1 mM unlabeled glucose also present) into hfRPE metabolites accompanied by schematic illustrations of the labeled species in the context of the TCA cycle. (n = 2–3 for each time point; error bars represent range or SD).

To confirm that mEC can also utilize lactate, we compared incorporation of ^{13}C from U-^{13}C lactate into metabolic intermediates in hfRPE, mRetina and mEC. Compared to mRetina, hfRPE and mEC incorporated more 'm3' malate, aspartate and fumarate (Figure 2.6). Lactate metabolism in hfRPE is more similar to mEC than mRetina, and is indicative of pyruvate carboxylation.

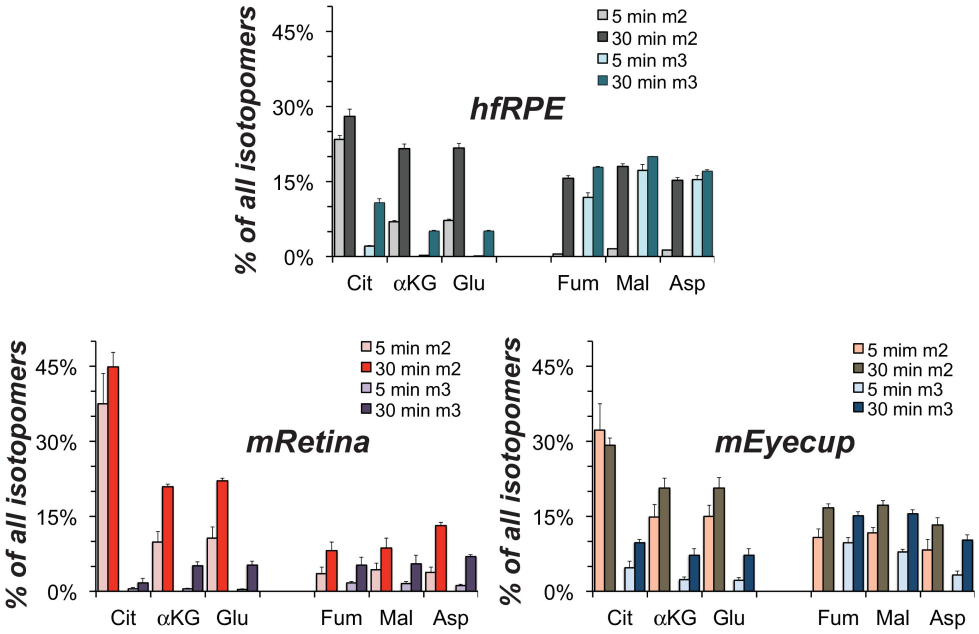

Figure 2.6. Comparison of lactate metabolism in hfRPE with lactate metabolism in mouse retinas and mouse eyecups with retinas removed. The high relative abundance of m3 metabolites derived from carboxylation reactions and the high abundance of fumarate, malate and aspartate in hfRPE cells resemble the metabolite distributions in the RPE enriched eyecup more than the distributions in retina. Each preparation was incubated with 10 mM U-^{13}C lactate for the 5 or 30 min and metabolites were extracted, derivatized and quantified by GC-MS. (n = 2 for hfRPE, n = 3 for mEyecup and n = 4 for mRetina; error bars represent range or SD).

Lactate can suppress glucose catabolism in RPE cells

Figures 2.5 and 2.6 show that RPE cells can consume lactate as fuel, and we next asked if lactate could suppress consumption of glucose. We hypothesized (Figure 2.7A) that lactate dehydrogenase (LDH) in RPE cells uses lactate to reduce cytosolic NAD^+ to NADH as it does in other cells (Hung et al., 2011). Since NAD^+ is required for glycolysis, depletion of NAD^+ by lactate and LDH could reduce glucose consumption.

We tested the effect of bathing hfRPE cells in lactate on their conversion of NAD^+ into NADH using a perifusion apparatus with an inverted microscope to measure total NADH fluorescence (Santos et al., 2017) from hfRPE monolayers. After equilibrating cells with 5.5 mM glucose, the perifusion medium was changed to supply 5.5 mM glucose with varying concentrations of lactate and pyruvate (Figure 2.7B, top). Lactate in the medium substantially increases NADH fluorescence, whereas pyruvate drives it to its

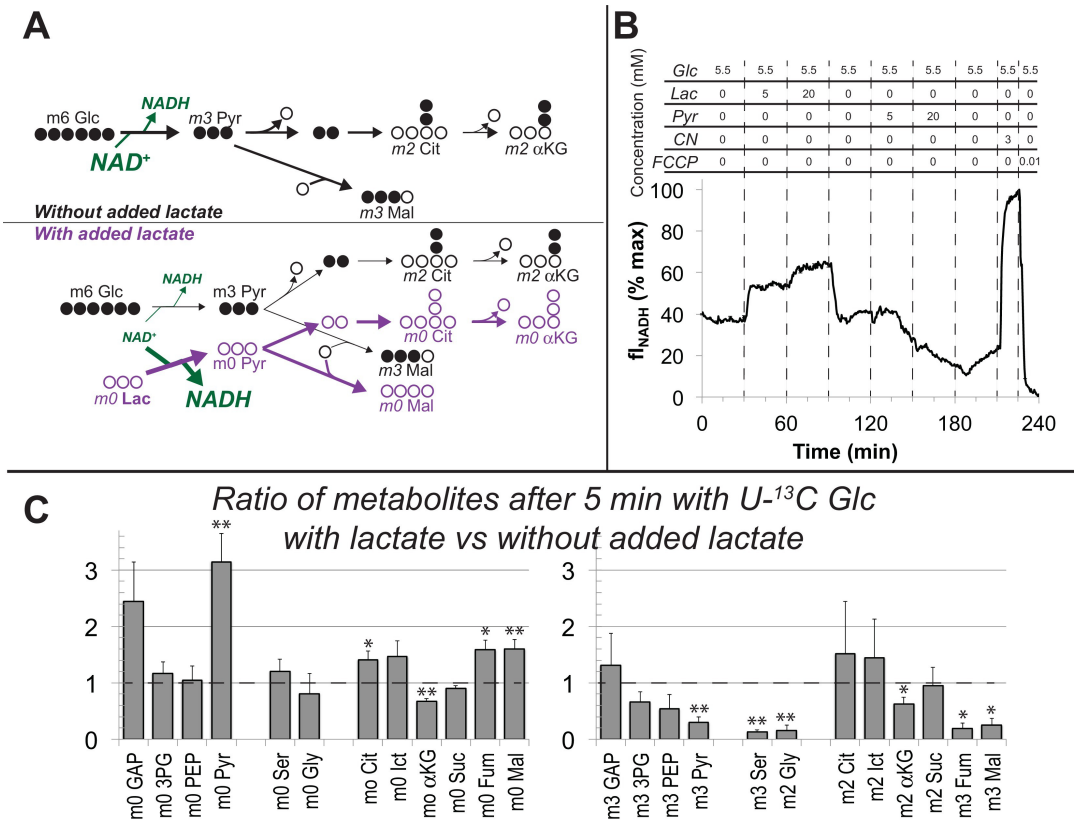

Figure 2.7. Lactate suppresses oxidation of glucose by hfRPE cells.
(A) Schematic prediction of how U-^{13}C Glc ('m6 Glc') would be metabolized without lactate (top) vs. with lactate (bottom). We hypothesized that lactate would suppress glycolysis of m6 Glc by depleting NAD^+ and that unlabeled (m0) pyruvate and TCA cycle intermediates would become more abundant. (B) Effect of lactate and pyruvate on total cellular NADH measured by fluorescence in a monolayer of hfRPE cells. The trace shows the average from 3 individual cells and is representative of 3 experiments. (C) Ratios of metabolites after 5 min incubation with U-^{13}C Glc in the presence or absence of unlabeled lactate (20 mM). Left, lactate substantially increases the total amounts of unlabeled (m0) GAP, pyruvate, citrate, isocitrate, fumarate and malate in hfRPE cells. Right, lactate suppresses the incorporation of ^{13}C from 5 mM ^{13}C Glc into glycolytic and TCA intermediates. (n = 3; error bars represent SE, * indicates $p<0.05$ and ** indicates $p<0.01$ for the comparison of with vs. without added unlabeled lactate)

oxidized state (Figure 2.7B, bottom). These results confirm that in RPE cells, exogenous lactate can deplete NAD^+ by reducing it to NADH.

To determine if lactate-induced NAD^+ depletion suppresses glycolysis in hfRPE cells, we incubated hfRPE cell monolayers with 5 mM U-^{13}C glucose in the absence or presence of unlabeled lactate, then used GC-MS to quantify incorporation of ^{13}C from glucose into glycolytic and TCA cycle intermediates. 20 mM lactate was selected based

on previous measurements of retina and RPE (Kolko et al., 2015; Matschinsky et al., 1968), and because native RPE in an eye is exposed to high levels of lactate released from the retina. Unlabeled lactate increases pools of unlabeled pyruvate, citrate, isocitrate, fumarate and malate (Figure 2.7C, left). Consistent with the results in Figure 2.5, carbons from lactate are incorporated rapidly into the TCA cycle through both pyruvate carboxylation and decarboxylation.

Addition of unlabeled lactate also causes accumulation of glyceraldehyde-3-phosphate (GAP), the triose phosphate immediately upstream of the glyceraldehyde-3-phosphate dehydrogenase (GAPDH) reaction that requires NAD^+. Lactate diminishes incorporation of ^{13}C from U-^{13}C glucose into intermediates downstream of the GAPDH reaction (Figure 2.7C, right), consistent with suppressed GAPDH activity. Lactate does not diminish incorporation of ^{13}C from glucose into 'm2' citrate or isocitrate, perhaps reflective of enhanced TCA cycle activity from anaplerotic supplementation of unlabeled intermediates (Figure 2.7C, left). We conclude that exogenous lactate can suppress glycolysis in hfRPE cells.

20 mM lactate seems non-physiological because it is higher than the <2–2.5 mM concentration normally in human serum (Wacharasint et al., 2012), and the 7–16 mM range in mouse serum (Burgess and Sylven, 1962). We found similar suppression of glycolysis using 10 mM lactate; formation of 'm3', but not 'm0' glycolytic intermediates was diminished (Figure 2.8A,B). We also measured the effect of pyruvate, which drives formation of oxidized NAD^+ (Figure 2.7B). Pyruvate and its amino derivative, alanine, cause redistributions in the relative amounts of specific glycolytic and mitochondrial intermediates (Figure 2.8C–F).

Lactate can enhance transport of glucose across a monolayer of hfRPE cells

By suppressing glycolysis (Figures 2.7, 2.8), we hypothesized that lactate can enhance the net flow of glucose across the RPE. The simplest version of this hypothesis is that lactate minimizes consumption of glucose, so that more glucose can translocate from the basolateral to the apical side of the RPE.

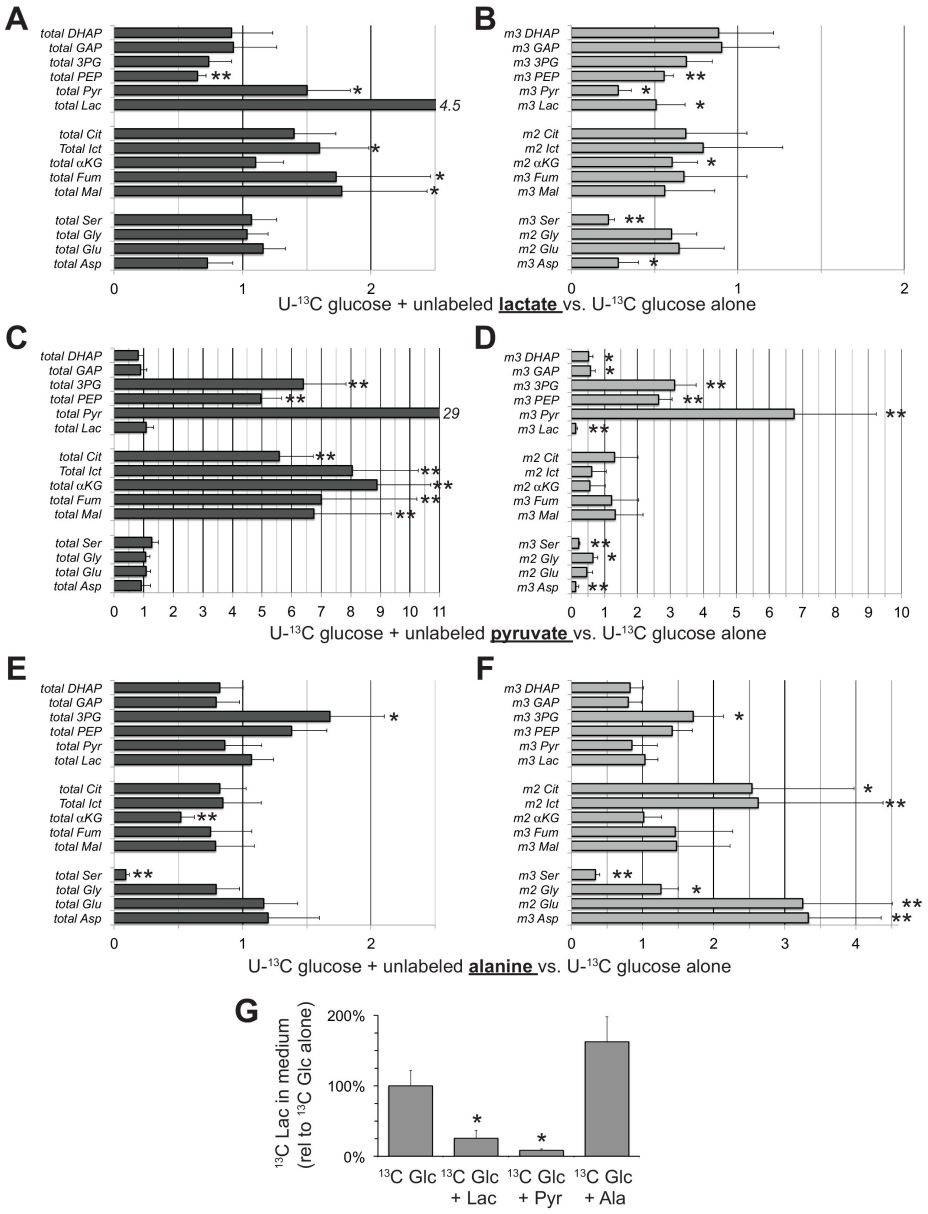

Figure 2.8. Effects of lactate, pyruvate and alanine on metabolic flux from U-^{13}C glucose in hfRPE cells. Each bar graph compares the ratio of metabolites with vs. without the addition of 10 mM of either unlabeled lactate (A,B) pyruvate (C,D) or alanine (E,F). A, C and E report the ratios for the total of all isotopomers of each metabolite, and B, D and F report the ratios for specific labeled metabolites (m2 or m3). Panel G shows the effects of adding unlabeled lactate, pyruvate or alanine on the release of ^{13}C lactate generated by glycolysis of U-^{13}C glucose. Metabolites were extracted, derivatized and quantified after 5 min incubation with 5 mM U-^{13}C glucose (n = 3) or 5 mM U-^{13}C glucose plus 10 mM unlabeled lactate (n = 3), pyruvate (n = 3) or alanine (n = 3). Error bars report SD. *p<0.05; **p<0.01.

To test this hypothesis, we measured the influence of lactate on transport of glucose across a monolayer of hfRPE cells. We grew hfRPE cells on transwell filters to confluence in a sealed monolayer, then added U-^{13}C glucose to the basolateral chamber where RPE cells would face the choroidal blood supply in an eye. GC-MS was used to quantify accumulation of ^{13}C glucose in the apical chamber, where RPE

cells normally would face a lactate-rich retina. We performed this experiment in the presence or absence of 10 mM unlabeled lactate on the apical side (Figure 2.9A). Unlabeled lactate in the apical medium substantially increases the accumulation of ^{13}C glucose on the apical side (Figures 2.9B, C), an effect more pronounced with 2 mM (Figure 2.9F) instead of 5 mM ^{13}C glucose (Figure 2.9E). Unlabeled lactate in the apical compartment also suppresses accumulation of ^{13}C pyruvate and ^{13}C lactate on the apical side (Figure 2.9B, C). These results are consistent with exogenous lactate suppressing of glycolysis in the RPE.

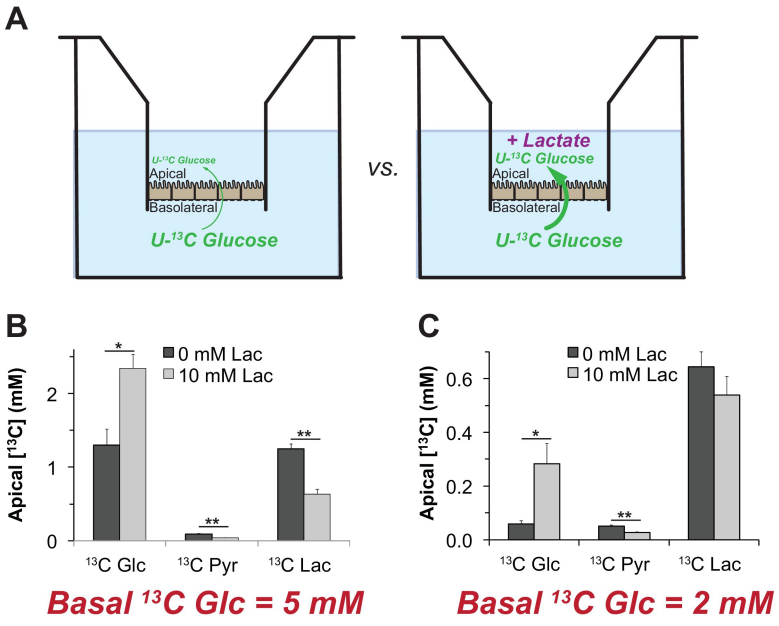

Figure 2.9. Lactate can enhance transport of glucose across a monolayer of RPE cells. (A) Strategy to evaluate the effect of lactate on transport of glucose across a monolayer of RPE cells. We hypothesized that without lactate (left) glycolysis consumes glucose before it can cross the RPE cell monolayer. With lactate on the apical side (right) glycolysis would be partially suppressed so more glucose can cross the monolayer without being consumed by glycolysis. (B,C) Glucose on the apical side after 8 hr. These panels compare the concentrations of ^{13}C Glc, ^{13}C Pyr and ^{13}C Lac in the apical chamber 8 hr after 5 mM (B) or 2 mM (C) ^{13}C Glc was added to the basolateral chamber (n = 3).

We focused on effects of lactate because it is more physiologically relevant than pyruvate or alanine. In separate experiments with mouse retinas we found that pyruvate is released from mouse retinas release pyruvate at only 6.7 ± 2.3% the rate of lactate release, and alanine is released at only 0.4 ± 0.1% of that rate (SD, n = 13). Together these findings suggest that high concentrations of lactate released from the retina can hinder glycolysis in the RPE so that more glucose reaches the retina.

Discussion

Model for a network of metabolic interdependence between the retina and RPE

Figure 2.10 summarizes the retina-RPE metabolic ecosystem model. We propose that lactate from photoreceptors suppresses glycolysis in the RPE so more glucose can reach the retina.

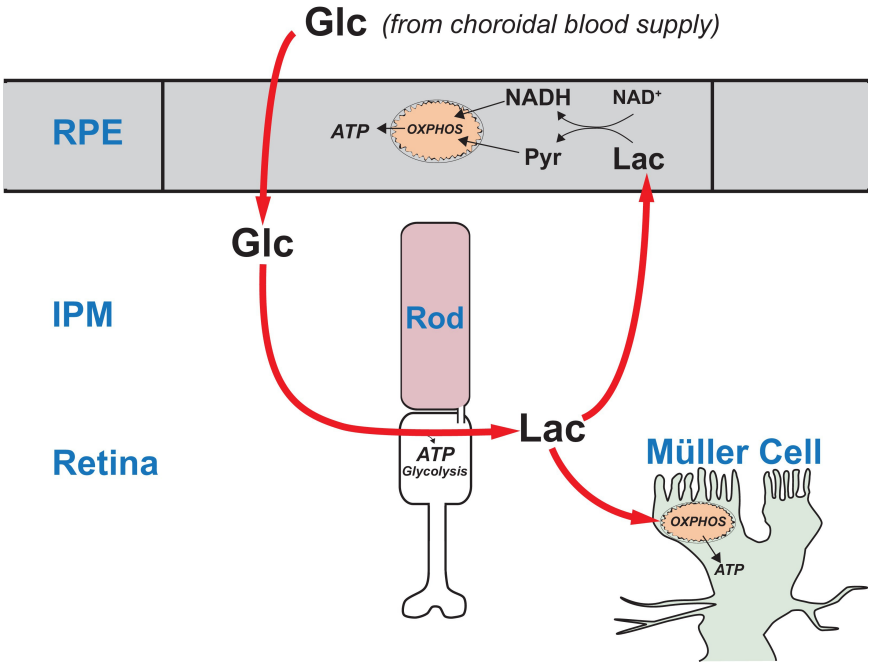

Figure 2.10. A working model that describes the flow of metabolic energy in the retina-RPE ecosystem. Photoreceptors convert glucose into lactate and release the lactate into the interphotoreceptor matrix (IPM). Lactate suppresses glycolysis in RPE cells by depleting NAD^+. Lactate also fuels metabolic activity in Müller cells, which lack key enzymes that would be required for glycolysis.

Previous evidence that cells in the retina have specific metabolic roles

Photoreceptors but not MGCs appear to have the enzymes and transporters needed for glycolysis. Pyruvate kinase catalyzes the last step of glycolysis and is highly enriched in photoreceptors (Casson et al., 2016; Chinchore et al., 2017; Lindsay et al., 2014; Rajala et al., 2016; Rueda et al., 2016) but not MGCs in mouse retina (Lindsay et al., 2014). MGCs also do not express hexokinase (Rueda et al., 2016), the enzyme required for the first step of glycolysis. Furthermore, lactate, rather than glucose, is the most effective source (Lindsay et al., 2014) of carbon for glutamine synthesis by MGCs (Riepe and Norenburg, 1977) in mouse retinas.

Based on these observations, we proposed that MGCs in a retina are fueled by lactate from photoreceptors (Hurley et al., 2015). The findings in this report further suggest the

central metabolic role of photoreceptors in retinal energy metabolism is to convert glucose to lactate, which both RPE and MGCs can use as fuel (Figure 2.10).

Significance of aerobic glycolysis in the retina

Aerobic glycolysis in photoreceptors is thought to enhance their anabolic capacity (Chinchore et al., 2017; Lindsay et al., 2014; Rajala et al., 2016) but our model suggests an additional purpose. In the laminated structure of an eye, the RPE separates the retina from its nutrient source. To maintain their glucose supply, we propose that photoreceptors must produce and release lactate to fuel MGCs and suppress glycolysis in the RPE.

The relationship between the 'retinal ecosystem' model and recent *in vivo* findings from genetically altered photoreceptors and RPE

In RPE cells *in vitro*, glucose is metabolized differently in the presence of additional fuels like lactate, pyruvate and alanine (Figures 2.7 and 2.8), and lactate can protect glucose from consumption (Figures 2.9B, C). However, more direct evidence is needed to validate the model in Figure 2.10 in a living animal, including genetic manipulations of photoreceptor and RPE cells and *in vivo* analyses of their phenotypes. Consistent with the model, recent genetic studies reported that photoreceptors engineered to be more glycolytic are more robust, while photoreceptors degenerate when glycolysis is enhanced in RPE cells (Kurihara et al., 2016; Venkatesh et al., 2015; Zhang et al., 2016; Zhao et al., 2011b). When photoreceptors are more glycolytic they produce more lactate, which suppresses glycolysis in the RPE; more glucose reaches the retina.

The concept of a metabolic ecosystem and its relationship to retinal disease

The model in Figure 2.10 could explain the linkage between age-related macular degeneration and accumulation of mitochondrial DNA damage in RPE cells (Terluk et al., 2015). When RPE mitochondria fail the cells become more dependent on glycolysis, and photoreceptors may starve if insufficient glucose reaches the retina.

The concept of a metabolic ecosystem also has implications for other types of retinal disease. Mutations in rod-specific genes cause both rods and then cones to degenerate, even though the cones are not affected directly by the mutation (Punzo et al., 2012). One reason is that loss of a cone viability factor normally produced by rods may contribute to cone degeneration (Aït-Ali et al., 2015). Another factor may also contribute to the secondary loss of cones: a retina without rods makes less lactate (Du et al., 2016a).

We have shown in this report that, without lactate to suppress glycolysis, RPE cells oxidize more glucose. This may explain why healthy rods and cones are shorter and dysmorphic in an environment where most of the surrounding photoreceptors have degenerated (Koch et al., 2017; Lewis et al., 2010). The loss of lactate production in rod-deficient retinas may limit the rate at which glucose can reach cones. This is consistent with starvation of cones (Punzo et al., 2009) and accumulation of 2-NBDG in RPE cells (Wang et al., 2016) when rods degenerate. Further, an alternative supply of glucose can rescue those cones from degeneration (Wang et al., 2016).

The importance of other fuels in the metabolic ecosystem

This study highlights one way that RPE, photoreceptors and MGCs can work together as an ecosystem of metabolically specialized and interdependent cells. Our investigation focused on lactate because so much of it is exported from the retina, but glycogen (Senanayake et al., 2006), fatty acids (Joyal et al., 2016; Reyes-Reveles et al., 2017), ketone bodies (Adijanto and Philp, 2014), glutamine (Du et al., 2016b), proline (Chao et al., 2017), and metabolites from other metabolic pathways (Chao et al., 2017; Rueda et al., 2016) also must contribute significantly to this metabolic ecosystem. Future investigations should optimize conditions to reliably quantify the kinetics of glucose transport across RPE cells.

It also will be important to evaluate glucose transport across RPE cells in the context of intracellular glycogen. Based on previous findings (Senanayake et al., 2006) it is likely that glycogen in RPE cells functions as a glucose buffer that acts either directly in the

glucose transport pathway or as a side pathway. Experiments that exploit the availability of ^{12}C and ^{13}C isotopomers of glucose may divulge the role that glycogen plays in glucose transport across RPE cells.

Recent studies showed that oxidation of fatty acids by the RPE can supply the retina with ketone bodies (Adijanto and Philp, 2014), and that RPE can oxidize fatty acids from photoreceptor phagocytosis (Reyes-Reveles et al., 2017). Like lactate, fatty acids may also suppress glucose consumption by the RPE. Altogether, these studies suggest that energy homeostasis in retina and RPE relies on a complex and specialized interplay between metabolically distinct cells. A better understanding of this metabolic ecosystem could be used to develop general therapeutic strategies that are effective for multiple types of retinal degenerative diseases.

Materials & Methods

Animals

All research was authorized by the University of Washington Institutional Animal Care and Use Committee. Mice in the C57BL/6J background were maintained in the University of Washington South Lake Union vivarium at 27.5 °C on a 14 hr/10 hr light-dark cycle. C57BL/6J does not carry the rd8 mutation in the Crb1 gene (Mattapallil et al., 2012). Transgenic mice expressing eGFP under the Nrl promoter (Akimoto et al., 2006) (RRID:IMSR_JAX:021232), or tdTomato under the Rlbp-CRE promoter (Wohl and Reh, 2016) were described previously.

Transgenic heterozygote zebrafish in the AB background were maintained in the University of Washington South Lake Union aquatics facility at 27.5 °C on a 14 hr/10 hr light-dark cycle. Fish used for experiments were male and female siblings between 12–24 months old. A transgenic line stably expressing tdTomato in Müller cells (GFAP:tdTomato) was described previously (Shin et al., 2014). Prior to gavage experiments, fish were fasted >18 hr and dark-adapted >12 hr.

Antibodies

Arrestin1, D9F2 (from Larry Donoso and Cheryl Craft)	IHC:	1:200
GLUT1, (AbCam, ab115730; RRID:AB_10903230)	IB:	1:200,000, 0.86 ng/mL
	IHC	1:1000, 0.17 mg/mL
GLUT3, (AbCam, ab41525; RRID:AB_732609)	IB:	1:5000, 0.136 mg/mL
GLUT4, (AbCam, ab654; RRID:AB_305554)	IB:	1:5000
Glutamine synthetase, (Millipore, MAB302; RRID:AB_2110656)		
	IHC:	1:1000
MTCO1 (Abcam, ab14705; RRID:AB_2084810)	IHC:	1:2000

Tissue preparations for immunoblotting

Frozen tissue samples were homogenized in RIPA buffer (150 mM NaCl, 1% Triton X-100, 0.05% sodium deoxycholate, 0.1% SDS, 50 mM Tris, pH 8.0) with a mixed phosphatase and protease inhibitor cocktail (ThermoFisher 88668), briefly sonicated, then rocked at 4 °C for 30 min. Samples were then spun at 13,300 RPM at 4 °C for 15 min, and the supernatant was normalized for loading by BCA assay to 20 mg/tissue. RPE protein lysate was prepared according to a described protocol (Wei et al., 2016). To prepare membrane fractions, frozen tissue samples were homogenized in PBS (0.14 M, pH 7.4) with a mixed phosphatase/protease inhibitor cocktail, then rocked at 4 °C for 30 min. Samples were then spun at 45,000 rpm at 4 °C, the supernatant (cytosolic fraction) drawn off and saved, and the pellet (membrane fraction) resuspended in an equal volume of PBS. After mixing with 5X Laemmli loading buffer, 1 mL benzonase (Millipore 70746) was added. Each tissue was then loaded with equal volumes of cytosolic and membrane fraction.

Immunoblotting

Samples were run on 12%, self-cast acrylamide gels and transferred onto PVDF membranes (Millipore IPFL00010). Following protein transfer, membranes were blocked with LI-COR Odyssey Blocking Buffer (LI-COR, 927–40000) for 1 hr at room temperature. Primary antibodies were diluted in blocking buffer and incubated overnight at 4 °C. Membranes were washed, incubated with secondary antibody (LI-COR IRDye

800CW, 926–32210, (RRID:AB_621842), and 926–32211, (RRID:AB_ 621843),1:5000 1 hr at room temperature, and washed again. Imaging was performed using the LI-COR Odyssey CLx Imaging System (RRID:SCR_014579).

Immunohistochemistry

Retinal eyecups were micro-dissected from C57BL/6J mice and were fixed in 4% paraformaldehyde in PBS, rinsed with PBS, incubated in a sucrose gradient (5%, 10%, and 20%), embedded into OCT and cryosectioned at 20 µm. Mouse sections were washed in PBS, then blocked in IHC buffer (5% normal donkey serum diluted in PBS with 2 mg/mL BSA and 0.3% Triton X-100) for 1 hr. Primary antibodies were diluted in IHC blocking buffer as specified, and applied to blocked cryosections overnight at 4℃. Secondary antibodies were diluted at 1:3000 in IHC blocking buffer, and applied to mouse retina sections for 1 hr in darkness. Sections were washed in PBS three times, and mounted with SouthernBiotech Fluoromount-G (Fisher Scientific) under glass coverslips and visualized using a Leica SP8 confocal microscope with a 63X oil objective. Images were acquired at a 4096x4096 pixel resolution with a 12-bit depth using Leica LAS-X software (RRID:SCR_013673).

RPE cell culture

Human fetal eyes with a gestational age of 16–20 weeks were harvested and shipped overnight on ice in RPMI media containing antibiotics from Advanced Bioscience Resources Inc. (Alameda, CA). Dissections of fetal tissue were performed within 24 hr of procurement and followed a modified version of the dissection protocol in order to isolate the retinal pigment epithelium (RPE) (Sonoda et al., 2009). The fetal RPE sheets were incubated at 37 °C with 5% CO_2 and cultured in RPE media. The RPE media consisted of Minimum Essential Medium alpha (Life Technologies) supplemented with 5% (vol/vol) fetal bovine serum (Atlanta Biologicals), N1-Supplement (Sigma-Aldrich), Nonessential Amino Acids (Gibco), and a Penicillin-Streptomycin solution (Gibco). Isolated fetal RPE reached confluency about 3–4 weeks after dissection and was then passaged using a 0.25% Trypsin-EDTA solution (Gibco) and passed through a 40 µm nylon cell strainer (BD Falcon) in order to collect a suspension of single cells. After counting, the RPE cells were plated onto 0.3 cm^2 cell culture inserts (Falcon)

coated with Matrigel (Corning) at a seeding density of 100,000 cells per insert. Cells grown on these inserts were cultured in RPE media containing 1% (vol/vol) FBS. Transepithelial resistance was measured weekly after 2 weeks in culture using a Millicell ERS-2 Epithelial Volt-Ohm Meter (Millipore).

Oral gavage

Mice were fasted overnight in the dark, and gavaged the next morning in ambient light. A micro- syringe fitted with a 22 gauge 1.5" straight 1.25 mm ball-tip needle was used to orally administer 100 µL of either saline or 50 mM 2-NBDG (Invitrogen, Carlsbad, CA) dissolved in water. Successfully gavaged mice were returned to darkness during the 2-NBDG incubation period.

Zebrafish were gavaged using methods described previously (Collymore et al., 2013) under red light. Briefly, overnight fasted adult zebrafish were anaesthetized >1 min with 150 mg/mL MS-222 in fish water. Fish were placed in a slit cut in a cellulose sponge soaked with MS-222 solution, and the sponge was rotated to orient the fish mouth up. A micro-syringe fitted with thin, flexible 1 mm OD plastic tubing was used to orally administer 5 µL of either fish water or 30 mM 2-NBDG. Gavaged fish were immediately placed into a recovery tank of fresh fish water and monitored briefly using a UV flashlight for regurgitation of 2-NBDG. Successfully gavaged fish were returned to darkness during the 2-NBDG incubation period.

Tissue slicing and imaging

Gavaged mice were euthanized by asphyxiation with CO_2. Zebrafish were euthanized in an ice bath followed by cervical dislocation. Euthanized animals were enucleated, and the retinas dissected away under red light into cold Ringer's solution (133 mM NaCl, 2.5 mM KCl, 1.5 mM NaH_2PO_4, 2 mM $CaCl_2$, 1.5 mM $MgCl_2$, 10 mM HEPES, 10 mM D-glucose, 1 mM sodium lactate, 0.5 mM L-glutamine, 0.5 mM reduced glutathione, 0.5 mM sodium pyruvate, 0.3 mM sodium ascorbate, pH 7.4). Isolated retinas were mounted on filter paper (0.45 µm pore, mixed cellulose, Millipore) and flattened with gentle suction. After peeling away remaining RPE, flat-mounted retinas were sliced into 300–400 µm slices using a tissue slicer (Stoelting). Slices were rotated 90° and the

filter paper edges buried in strips of wax on a coverslip for imaging at room temperature. Fresh retinal slices were imaged at room temperature using a Leica SP8 confocal microscope with a 40X water objective; excitation/emission wavelengths were 488/525–575 nm for 2-NBDG, and 559/580–630 nm for tdTomato. Leica LAS-X (RRID:SCR_013673) software was used to acquire images at 2048 x 2048 pixel resolution with 12 bit depth, and Z-stacks imaged every 0.5 µm over a tissue depth of 10–30 µm.

Image analysis

ImageJ software (RRID:SCR_002285) was used for quantification of 2-NBDG fluorescence in fresh retinal slices. 10 slices of each Z-stack were maximum intensity projected, and retinal layers were identified by morphology and expression of transgenic markers. For every slice, 3 small uniformly sized rectangular regions of interest (ROIs) were placed randomly in each retinal layer, and mean fluorescence intensity of each ROI was measured. Average 2-NBDG fluorescence in each layer was divided by the autofluorescence of corresponding retinal layers from animals gavaged with saline or water.

Metabolic flux analysis

Isolated mouse retina or confluent human fetal RPE cells were changed into pre-warmed Krebs-Ringer bicarbonate buffer (KRB) containing, depending on the experiment, [1,2] ^{13}C glucose, U-^{13}C glucose, or U-^{13}C lactate (Sigma) as described elsewhere (Du et al., 2013b; 2015; 2016b). Both retinas and RPE cells were incubated for the specified time points. Metabolites from each time point were extracted and analyzed by gas chromatography mass spectrometry (GC-MS, Agilent 7890/5975C) as described in detail (Du et al., 2013a; 2013b).

Measurement of U-^{13}C glucose transport across hfRPE cells on transwell filters

After maturation for 4–6 weeks in culture, hfRPE cells grown on transwell filters (Millicell HA 0.45 µm pore size 0.6 cm^2) were changed into 500 µL of DMEM containing 1% FBS on each side. 5 mM U-^{13}C glucose (Cambridge Isotope Laboratories) was included in the medium in the basolateral side while various concentrations of sodium lactate were

added to the apical side, while maintaining a constant pH. Apical side medium was collected at 8 hr to analyze the transported U-^{13}C glucose by liquid chromatography coupled with triple quadrupole mass spectrometry (Waters Xevo TQ Tandem mass spectrometer with a Waters ACQUITY system with UPLC) as reported in detail (Du et al., 2015).

Live-cell imaging NAD(P)H autofluorescence

Cultured hfRPE cells were attached to cover slips that were previously coated with a thin layer of Matrigel (Corning, Corning NY) diluted 1:30 1–2 days prior to the imaging experiment. NAD(P)H was imaged and quantified similarly to a previous study (Jung et al., 2009). Cells were perifused with KRB (supplemented with 0.1% bovine serum albumin and 1% penicillin streptomycin fungizone (Invitrogen)) at a flow rate of ~0.1 mL/min at 37 °C on the stage of a Nikon Eclipse TE-200 inverted microscope. Fluorescence imaging of NAD(P)H was measured with emission detected at 460 nm by a CoolSnap HQ2 CCD camera (Photometrics, Tucson, AZ) through a 40X Super Fluor Nikon objective (DIC H/N2) during excitation at 360 nm via a Xenon lamp (Lambda LS-1620, Sutter Instrument Company, Novato, CA). NAD(P)H fluorescence integration time was 50 msec. The software package Elements (Nikon) was used to drive the data acquisition. At the completion of each protocol, the steady-state levels of relative fluorescence (RFU) during exposure of KCN and subsequently FCCP were measured and this data was used to normalize the RFU data. The normalization of the NAD(P)H signal was as a percent of RFU_{FCCP} and RFU_{KCN}, defined as 0% and 100% respectively for each cell.

Serial block face SEM

Mouse eyes were enucleated, the anterior half was dissected away, and the eyecup was cut in half. Tissue was fixed in 4% glutaraldehyde in 0.1 M sodium cacodylate buffer, pH 7.2, at room temperature (RT), then stored overnight at 4 °C. Samples were washed 4 times in sodium cacodylate buffer, postfixed in osmium ferrocyanide (2% osmium tetroxide/3% potassium ferrocyanide in buffer) for 1 hr on ice, washed, incubated in 1% thiocarbohydrazide for 20 min, and washed again. After incubation in 2% osmium tetroxide for 30 min at RT, samples were washed and en bloc stained with

1% aqueous uranyl acetate overnight at 4 °C. Samples were finally washed and en bloc stained with Walton's lead aspartate for 30 min at 60 °C, dehydrated in a graded ethanol series, and embedded in Durcupan resin. Serial sections were cut at 60 nm thickness and imaged with 6 nm pixel size using a Zeiss Sigma VP scanning electron microscope fitted with a Gatan 3View2XP ultramicrotome apparatus. Imaged stacks were concatenated and aligned using TrakEM2 (RRID:SCR_008954). Unless stated otherwise, five washes with water were used for all wash steps.

Statistical analyses

R (RRID:SCR_001905) with R Commander was used to perform one-way ANOVA for NBDG gavage experiments.

Reproducibility

Each set of data has been reproduced the number of times (n) described in each figure legend. 'n' refers to the number of retinas, eyecups or hfRPE wells that were analyzed. We did not make comparisons between mutant animals so n refers to the number of technical replicates, not the number of biological replicates.

Acknowledgments

The work described in this chapter was published in eLife. The other authors that contributed to this study were Mark A. Kanow (first author), Connor SR Jankowski, Kristine Tsantilas, Abbi L. Engel, Jianhai Du, Jonathan D. Linton, Christopher C. Farnsworth, Stephanie R. Sloat, Austin Rountree, Ian R. Sweet, Ken J. Lindsay, Edward D. Parker, Susan E. Brockerhoff, Martin Sadilek, Jennifer R. Chao, James B Hurley. This study was supported by funding from NIH EY06641 and NIH EY017863 to JBH, NIH EY026020 to SEB, NEI core grant EY001730 and P30 DK-17047 (Cell Function Analysis Core), NSF GRFP 2013158531 and NIH NEI 5T32EY007031 to MMG and NIH EY026030 to JRC.

Chapter 3

Mitochondria maintain distinct Ca^{2+} pools in cone photoreceptors

Introduction

Vertebrate retinal photoreceptors are specialized neurons that initiate vision by transducing light into an electrical signal. These highly polarized cells are comprised of three physiologically discrete regions: 1) the outer segment containing phototransduction machinery, 2) the cell body where proteins are synthesized and trafficked, and 3) the synapse which releases neurotransmitter onto downstream neurons (Dowling, 1987).

Calcium ions (Ca^{2+}) regulate key pathways in each photoreceptor compartment. At the outer segment, extreme changes in intracellular free Ca^{2+} concentration ($[Ca^{2+}]_i$) mediate phototransduction response recovery that causes a change in membrane potential (Dizhoor, 2000; Gorczyca et al., 1995; Kawamura and Murakami, 1991). In the cell body, Ca^{2+} is stored in mitochondria and endoplasmic reticulum (ER), where it can influence metabolism (Du et al., 2016a; Glancy et al., 2015; Jouaville et al., 1999; Wan et al., 1989) and protein trafficking (Beckers and Balch, 1989; Booth and Koch, 1989). At the synapse, Ca^{2+} influx is critical for release of glutamate-containing synaptic vesicles (Heidelberger et al., 2005; Rieke and Schwartz, 1996; Schmitz, 2014; Thoreson et al., 2004). Given the distinct roles of Ca^{2+} in each photoreceptor compartment, tight control of Ca^{2+} domains is crucial for normal cell function.

Mitochondrial Ca^{2+} uptake results in variety of physiological outcomes, including fundamental processes like protein acetylation in endothelial cells (Marcu et al., 2014). In neurons, mitochondria buffer Ca^{2+} in areas of high axonal firing to produce ATP (MacAskill et al., 2009) and mitigate excitotoxicity via the mitochondrial Ca^{2+} uniporter (MCU) (Qiu et al., 2013; Wang et al., 2015). In muscle, mitochondrial Ca^{2+} couples

metabolic output to contraction (Kwong and Perry, 2015) and influences muscle size (Mammucari et al., 2015). Past studies have indicated that photoreceptor mitochondria can act as a Ca^{2+} sink, particularly in cones, and it has been suggested that mitochondria may shield the cell body and synapse from potentially harmful high $[Ca^{2+}]_i$ in the outer segment (Szikra and Krizaj, 2007).

Photoreceptor mitochondria are spatially and biochemically poised to regulate cellular Ca^{2+}. Electron microscopy of cones reveals abundant mitochondria within the ellipsoid region of the cell body, just below the outer segment (Masuda et al., 2016; Tarboush et al., 2012). Mitochondria in other tissues are capable of storing large amounts of Ca^{2+} as inorganic phosphate salts (Greenawalt et al., 1964). The MCU is thought to be the primary entry point for Ca^{2+} into the mitochondrial matrix in all cells (De Stefani et al., 2011) although this has not been shown for photoreceptors.

We evaluated the role of mitochondria in maintaining distinct Ca^{2+} domains. We used serial block-face scanning electron microscopy (SEM) to assemble the 3-D morphology of the zebrafish cone ellipsoid. A dense cluster of mitochondria extends to the plasma membrane directly between the outer segment and cell body. We further developed a method to visualize Ca^{2+} dynamics in live retinal slices from adult zebrafish. By manipulating $[Ca^{2+}]_i$ in the presence of a genetically-encoded fluorescent Ca^{2+} reporter, we found that cone mitochondria act via the MCU to segregate outer segment and cell body Ca^{2+} pools. This finding suggests a significant role for cone mitochondria in the Ca^{2+} compartmentalization that is required for proper function and regulation of core cellular processes like phototransduction and metabolism.

Results

A genetically encoded Ca^{2+} reporter senses cytosolic $[Ca^{2+}]$ in zebrafish cones

Larval zebrafish cones display cytosolic Ca^{2+} transients heterogeneous in magnitude and duration (Ma et al., 2013). To understand normal Ca^{2+} dynamics in adult zebrafish cones, we analyzed $[Ca^{2+}]_i$ changes using fresh retinal slices from adult zebrafish stably

expressing the genetically encoded Ca^{2+} sensor GCaMP3 in cone photoreceptor cytosol (cyto-GCaMP) (Figure 3.1A). Photoreceptors in retinal slices do not take up the stain propidium iodide for at least 4 hours, indicating that the cells remain viable (data not shown). Confocal time-lapse imaging of slices revealed that adult cones undergo Ca^{2+} transients in the synapse and cell body similar to larval cones (Figure 3.1B,C).

To determine whether $[Ca^{2+}]_i$ is sensitive to extracellular Ca^{2+} concentration ($[Ca^{2+}]_{ex}$), we time-lapse imaged cyto-GCaMP retinal slices while using perfusion to exchange the surrounding 2 mM Ca^{2+} Ringer's solution with Ca^{2+}-free solution containing 0.4 μM EGTA (Figure 3.1E,F). Initial removal of extracellular Ca^{2+} transiently, but robustly, increased cyto-GCaMP fluorescence, indicating possible Ca^{2+} release from internal stores (Figure 3.1E, arrowheads). When $[Ca^{2+}]_{ex}$ was returned to 2 mM, Ca^{2+} influx into the synapse and cell body increased cyto-GCaMP fluorescence 1.5 ± 0.2 fold and 2.7 ± 0.3 fold, respectively (15 min timepoint, Figure 3.1E,F). A second washout and return to 2 mM Ca^{2+} raised $[Ca^{2+}]_i$ in all compartments (at 22 min, outer segment, 2.5 ± 0.3 fold; cell body, 2.9 ± 0.3 fold; synapse, 1.6 ± 0.2 fold). Further, each cell compartment responded with unique kinetics and amplitude, indicating that Ca^{2+} in cones is not one continuous pool. To confirm that changes in cyto-GCaMP fluorescence report $[Ca^{2+}]_i$, we showed that fluorescence of cones expressing cytosolic eGFP (cyto-GFP, Figure 3.1D) (Kennedy et al., 2007) is not sensitive to fluctuations in $[Ca^{2+}]_{ex}$ (Figure 3.1E, dashed lines).

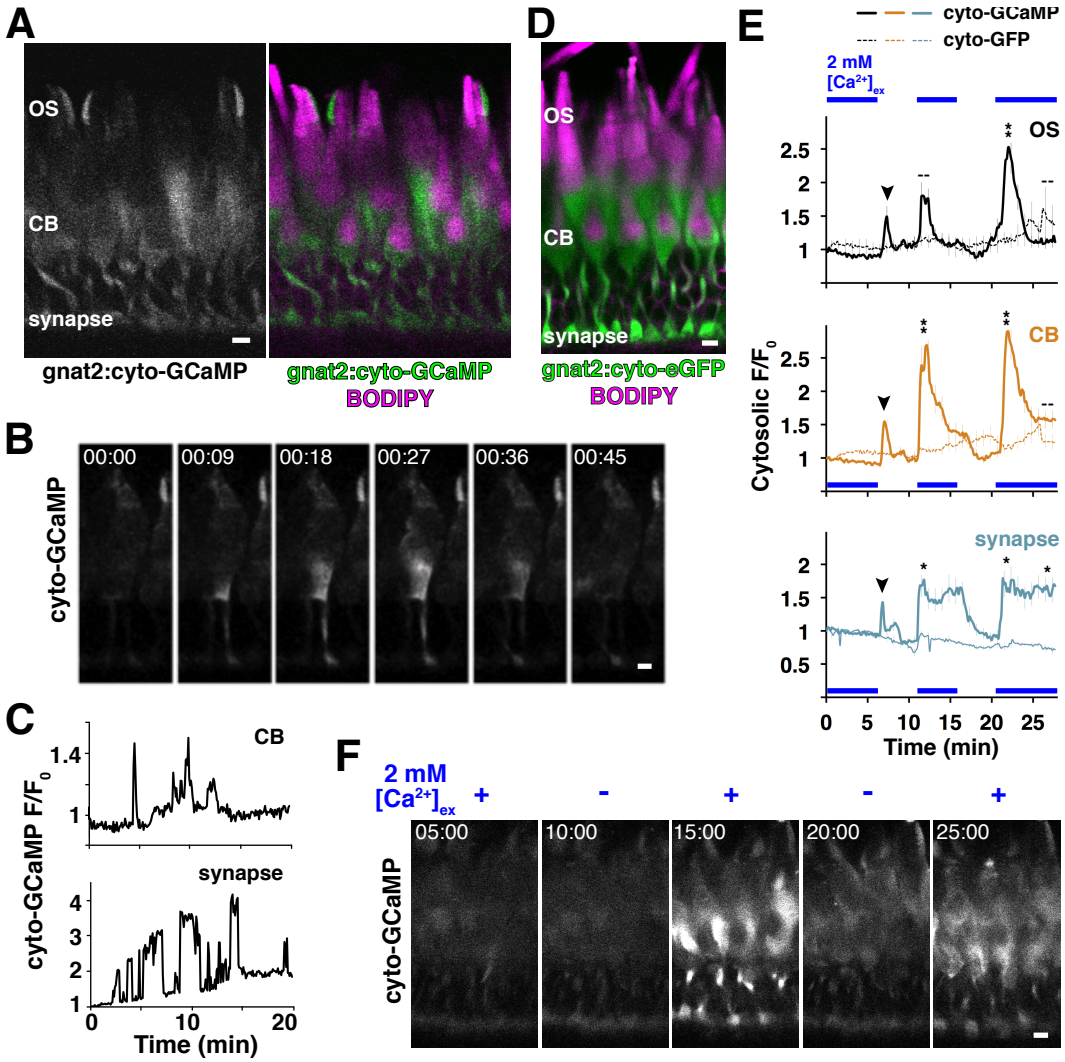

Figure 3.1. Cone photoreceptors undergo transient Ca^{2+} flashes and are sensitive to extracellular Ca^{2+} flux. (A) Representative confocal image of *in situ* retinal slice from transgenic dark-adapted zebrafish expressing cyto-GCaMP in cones (left) and overlaid with BODIPY membrane stain (right). Areas of bright cyto-GCaMP fluorescence in the outer segment layer appear to be the zebrafish accessory outer segment. (B) Montage of confocal images depicting spontaneous cyto-GCaMP Ca^{2+} flash in a single cone. (C) Graphs showing discrete and spontaneous Ca^{2+} flashes in the synapse and cell body of a single cone over 20 min. (D) Representative confocal image of retinal slice from transgenic dark-adapted zebrafish expressing cyto-GFP in cone PRs (green) stained with BODIPY membrane stain (magenta). (E) Mean fluorescence responses of cone compartments during consecutive washouts of extracellular Ca^{2+} with buffer containing 0.4 µM EGTA. Solid lines, cyto-GCaMP (3 experiments; n for OS = 27, CB = 31, synapse = 40). Dashed lines, cyto-GFP control (1 experiment; n for OS = 15, CB = 15, synapse = 18). Blue bars, presence of 2 mM extracellular Ca^{2+}. Arrowheads indicate transient burst of Ca^{2+} in all compartments following initial Ca^{2+} washout. One-way ANOVA was performed at 12:00, 22:00 and 27:00 for cyto-GCaMP v. cyto-GFP; * = $p < 0.05$; ** = $p < 0.001$; -- = not significant.

(F) Montage of confocal images depicting cyto-GCaMP responses to Ca^{2+} washout quantified in (E). Error bars represent SE; n represents number of single cells analyzed. Scale bars = 5 μm; timescale = min:sec. OS, outer segment; CB, cell body.

$[Ca^{2+}]$ in the mitochondrial matrix is influenced by cytosolic $[Ca^{2+}]$

Mitochondria can buffer Ca^{2+}, an activity vital to homeostasis in neurons (Esterberg et al., 2014; Qiu et al., 2013). To monitor free Ca^{2+} concentration within the mitochondrial matrix ($[Ca^{2+}]_m$) of cones, we used transgenic zebrafish that stably express GCaMP3 targeted to the matrix of cone mitochondria (mito-GCaMP, Figure 3.2A). Under basal time-lapse imaging conditions, mito-GCaMP retinal slices and flat-mounts displayed no fluctuation of fluorescence (data not shown), and mitochondria remained clustered at the base of the outer segment. Alternating $[Ca^{2+}]_{ex}$ from 2 to 0 mM induced modest but significant changes in $[Ca^{2+}]_m$ throughout the entire cluster (Figure 3.2C,D). Given that identical conditions elicit large changes in cyto-GCaMP, these data suggest that mitochondria can take up free cytosolic Ca^{2+}, although mito-GCaMP responses were generally slower. In contrast, zebrafish retinas expressing circularly-permuted YFP in cone mitochondria (mito-cpYFP, Figure 3.2B), which is not directly sensitive to Ca^{2+} (Wang et al., 2008), did not respond to altering $[Ca^{2+}]_{ex}$ (Figure 3.2C, dashed lines).

In other cells, Ca^{2+} flows into mitochondria through the MCU (Williams et al., 2013), so we asked if the MCU is responsible for mitochondrial Ca^{2+} uptake in cones. We imaged 3-D stacks of mito-GCaMP retinal slices incubated for 1 hour in either Ringer's solution or 10 μM Ru360, a specific inhibitor of the MCU (Baughman et al., 2011; Kirichok et al., 2004; Matlib et al., 1998). Mito-GCaMP fluorescence of individual cells was measured at the center of the mitochondrial cluster (Figure 3.2E). Ru360 treatment decreased absolute GCaMP fluorescence of mitochondrial clusters by 25.4 ± 7.1% (Figure 3.2E). Similar to other cells, Ca^{2+} uptake into cone mitochondria appears to occur through the MCU. 1 hour Ru360 incubation also altered baseline fluorescence of cyto-GCaMP retinal slices, decreasing outer segment signal 20.1 ± 11.0%, and increasing cell body and synaptic fluorescence 56.9 ± 6.9% and 16.2 ± 12.5%, respectively (Figure 3.2E). This suggests that Ca^{2+} homeostasis throughout the cell is influenced by mitochondrial Ca^{2+} uptake.

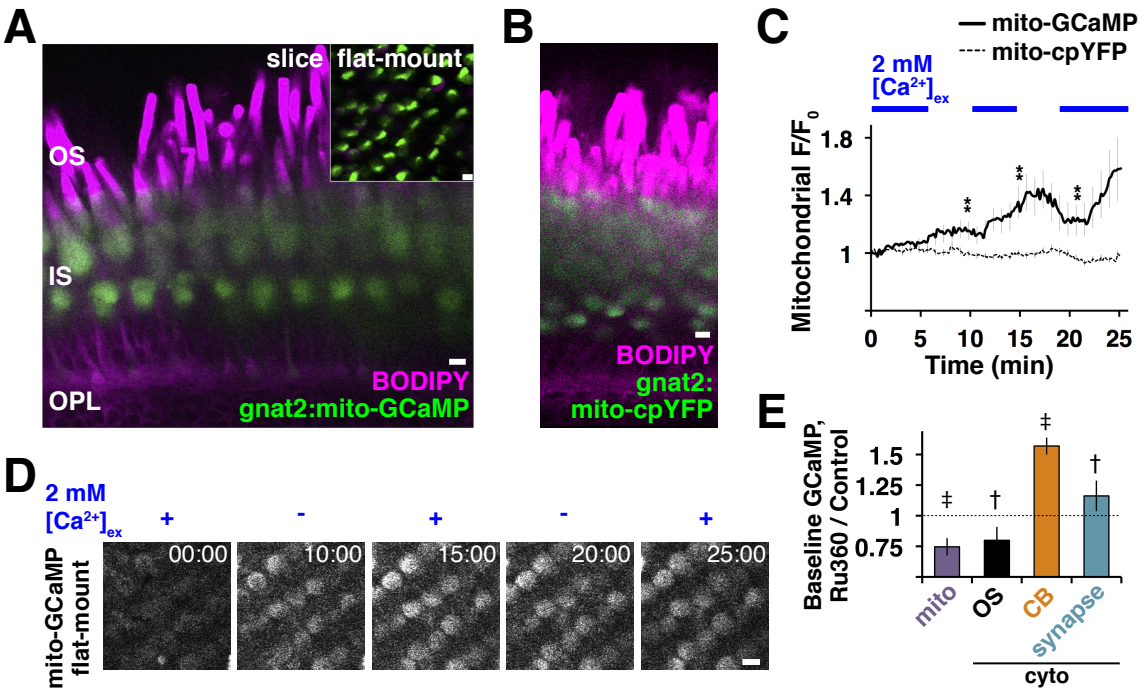

Figure 3.2. Cone mitochondria buffer intracellular Ca^{2+}. (A) Representative confocal images of *in situ* slice or flat-mount (inset) from transgenic dark-adapted zebrafish expressing mito-GCaMP in cone PRs (green) and stained with BODIPY membrane stain (magenta). (B) Representative confocal image of retinal slice from transgenic dark-adapted zebrafish expressing mito-cpYFP in cone PRs (green) stained with BODIPY membrane stain (magenta). (C) Mean fluorescence responses of cone mitochondria during consecutive washouts of extracellular Ca^{2+} with buffer containing 0.4 µM EGTA. Solid lines, mito-GCaMP (4 experiments; n = 45 cells). Dashed lines, mito-cpYFP control (4 experiments; n = 56 cells). Blue bars, presence of 2 mM extracellular Ca^{2+}. One-way ANOVA was performed at 10:00, 15:00, and 22:00 for mito-GCaMP v. mito-cpYFP; ** = $p < 0.001$. (D) Montage of flat-mount confocal images depicting mito-GCaMP Ca^{2+} responses quantified in (C). (E) Bar graph depicting mean baseline mito- and cyto-GCaMP fluorescence changes resulting from Ru360 preincubation (n for mitochondria = 15 experiments, 143 cells per condition; for OS = 3 experiments, 39 cells per condition; for CB = 3 experiments, 25 cells per condition; for synapse = 3 experiments, 24 cells per condition). Two-tailed T-tests were performed for each compartment for GCaMP control v. GCaMP Ru360; † = $p < 0.05$, ‡ = $p < 0.001$. Error bars represent SE. Scale bars = 5 µm; timescale = min:sec. OS, outer segment; IS, inner segment; OPL, outer plexiform layer; CB, cell body.

The cone ellipsoid contains a tight cluster of mitochondria

In photoreceptors, the unique morphology and localization of mitochondria (Tarboush et al., 2012; 2014) suggest they can influence Ca^{2+} homeostasis even more than in other cells. To understand the 3-D arrangement of mitochondria within the ellipsoid region of cones, we performed serial block-face SEM of adult zebrafish retina (Figure 3.3A). Mitochondria in zebrafish cones form a tight cluster in the ellipsoid just below the connecting cilium and outer segment. The mitochondrial cluster is comprised of ~80 individual mitochondria densely packed together with the outer membranes of individual mitochondria directly adjacent to one another (Figure 3.3B). A 3-D reconstruction shows that the cluster occupies the majority of the cell volume between the outer segment and cell body (Figure 3.3C). The abundance and very tight juxtaposition of the mitochondria supports the hypothesis that the mitochondrial cluster in zebrafish cones can act as a barrier to diffusion between the outer segment and cell body.

Contacts between ER and mitochondria facilitate mitochondrial Ca^{2+} uptake in many cell types (Rowland and Voeltz, 2012). ER in photoreceptors is confined to the synapse and cell body (Mercurio and Holtzman, 1982), and we evaluated the extent of interactions between ER and mitochondria in the cell body. Using adult zebrafish from a transgenic line expressing GFP targeted to cone ER (ER-GFP) (George et al., 2014), we found that the ER forms a basket-like network underneath the mitochondrial cluster, but does not appear to enter into the tight cluster of mitochondria (Figure 3.3D). Furthermore, in SEM images used for 3-D reconstruction we did not find evidence of ER within the mitochondria cluster, nor between the outer segment and apical face of the mitochondrial cluster (Figure 3.3B).

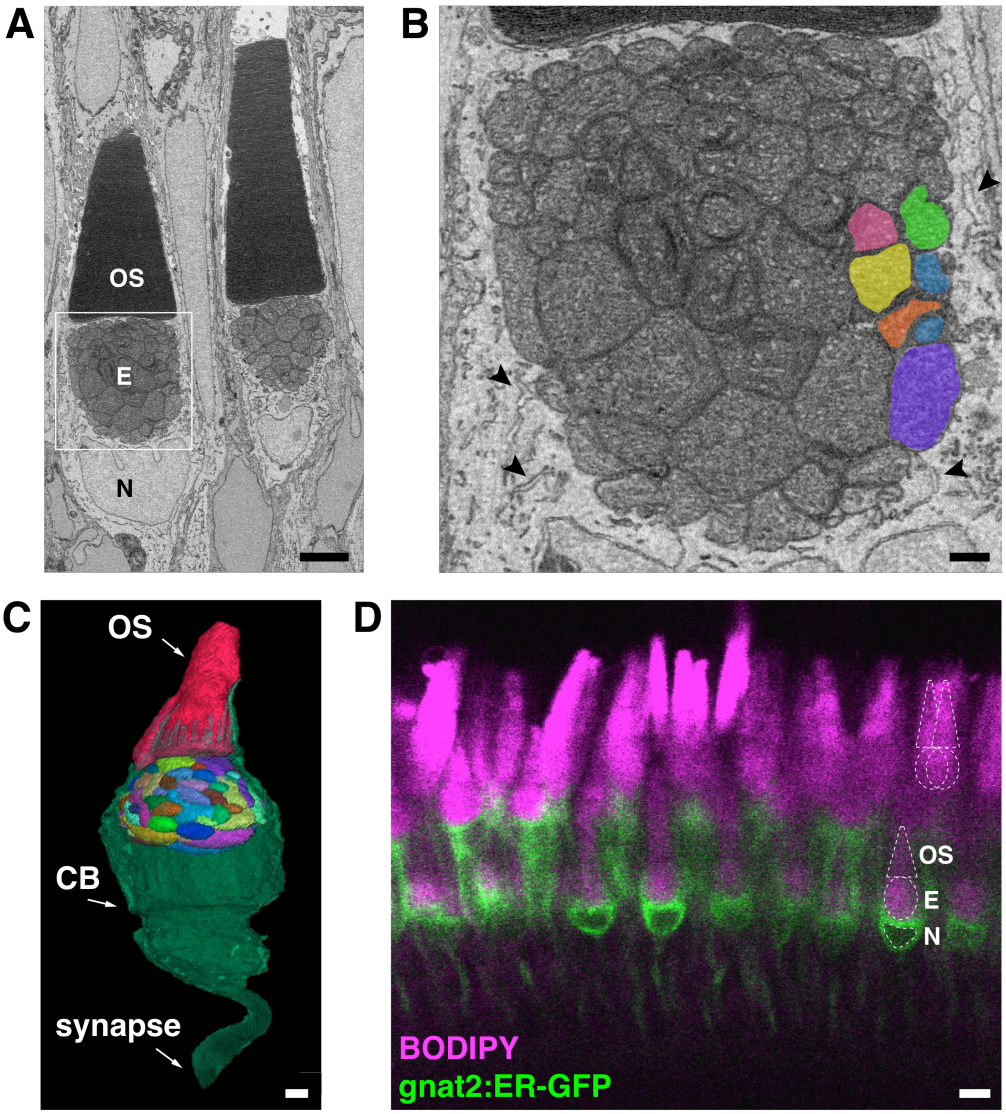

Figure 3.3. Cone mitochondria densely pack the interface between the inner and outer segments. (A) SEM image of two zebrafish cones showing dense packing of the mitochondrial cluster. (B) Zoom of boxed region in (A) showing the center of the mitochondrial cluster. Endoplasmic reticulum is indicated with arrowheads; matrices of six individual mitochondria are colored. (C) 3-D reconstruction from serial block-face SEM of an adult zebrafish cone; individual mitochondria are uniquely colored and outer segment is colored red. The tip of the outer segment and cone pedicle were not rendered in this image. (D) Representative confocal image of *in situ* transgenic zebrafish retinal slice expressing ER-targeted GFP in cones (green) and stained with BODIPY membrane stain (magenta). Scale bar in (A) = 10 μm; (B) = 2 μm; (C) = 1 μm; (D) = 5 μm. E, ellipsoid; N, nucleus; OS, outer segment; CB, cell body.

Ca^{2+} confinement to the inner segment is mediated by mitochondria.

To evaluate Ca^{2+} compartmentalization, we used two strategies to specifically increase inner segment $[Ca^{2+}]_i$. We depolarized cones by perfusing retinal sections with Ringer's solution containing elevated [KCl] while time-lapse imaging (Figure 3.4A, top). Depolarization of the plasma membrane activates L-type voltage gated Ca^{2+} channels at the synapse and cell body (Kourennyi and Barnes, 2000; Lee et al., 2015; Taylor and Morgans, 1998), allowing Ca^{2+} to flow into those compartments. We found that increasing extracellular [KCl] from 2.5 to 10 mM evoked more than a 2-fold rise in cyto-GCaMP fluorescence in the synapse and cell body, but notably no increase in fluorescence in the outer segment (Figure 3.4B, light solid lines). A modest 13 ± 3% increase in mito-GCaMP fluorescence persisted 5 minutes after increasing extracellular [KCl] (Table 3.1), suggesting mitochondria are capable of Ca^{2+} uptake from the cell body pool, perhaps via ER. Cyto-GFP (Figure 3.4B, dashed lines) and mito-cpYFP (Table 3.1) retinal slices were insensitive to KCl.

We hypothesized that reducing Ca^{2+} uptake into cone mitochondria could attenuate Ca^{2+} compartmentalization and lead to increases in outer segment $[Ca^{2+}]_i$, so we preincubated cyto-GCaMP retinal slices in Ru360, then depolarized them with 10 mM KCl (Figure 3.4A, bottom arrowheads). Outer segment fluorescence transiently increased 1.80 ± 0.04 fold compared to untreated slices (Figure 3.4B, dark solid lines), but synapse $[Ca^{2+}]_i$ was unaffected by Ru360. This is consistent with the absence of mitochondria at the zebrafish cone synaptic terminal (see Figure 3.2A), unlike in other teleost ribbon synapses (Zenisek & Matthews, 2000). 10 minutes following KCl depolarization, Ru360 treatment decreased cell body fluorescence slightly (1.41 ± 0.09 fold versus 1.18 ± 0.03 fold, $p = 0.045$), perhaps indicative of enhanced cell body Ca^{2+} extrusion through now-accessible rapid Na^+/K^+-Ca^{2+} exchangers on the outer segment. Redistribution of Ca^{2+} into the outer segment following Ru360 treatment suggests that compartmentalization requires efficient uptake of Ca^{2+} by mitochondria through the MCU.

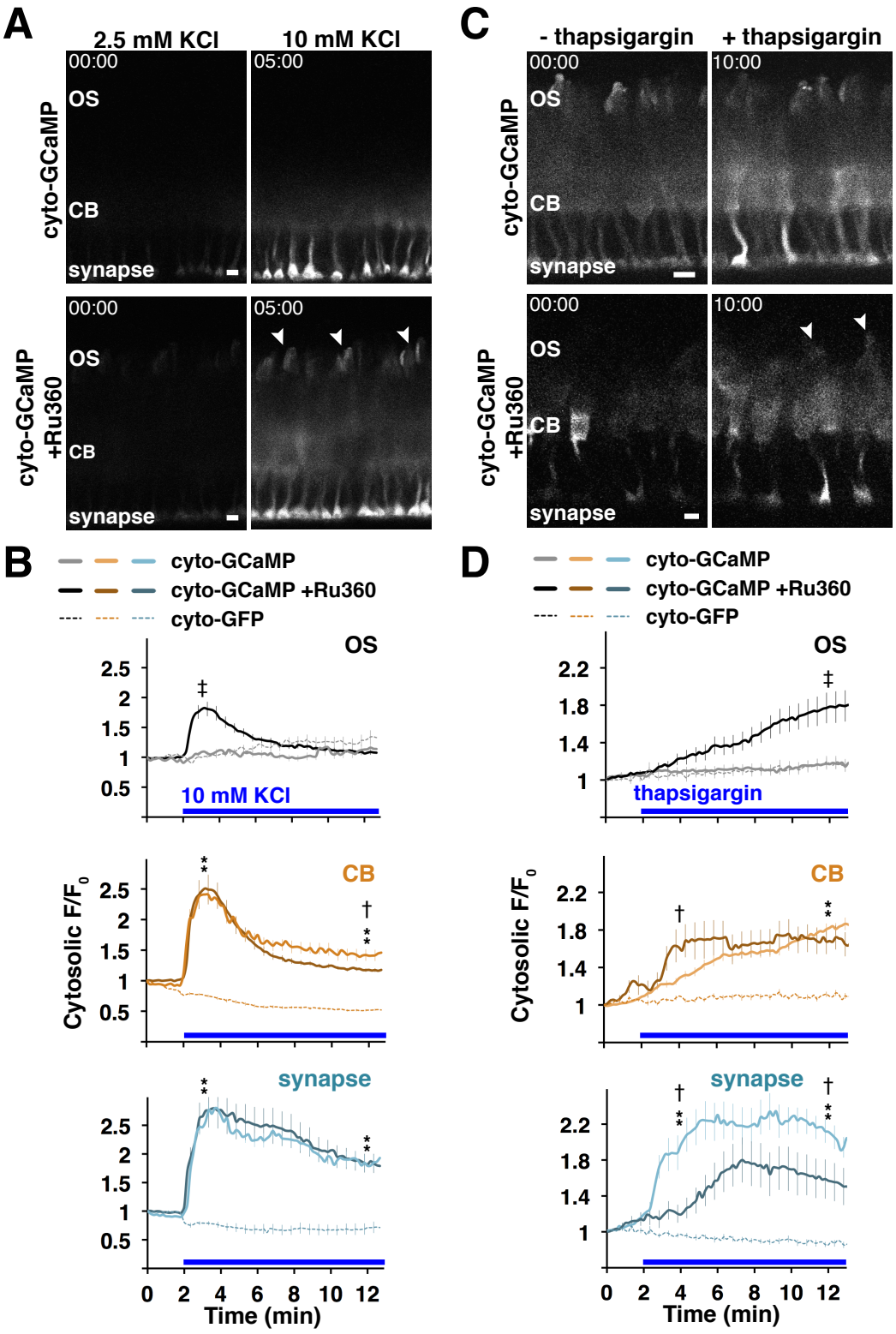

Figure 3.4. Cytosolic Ca^{2+} from the inner segment is isolated from the outer segment. (A) Representative confocal image of *in situ* retinal slices from transgenic dark-adapted zebrafish expressing cyto-GCaMP in cones before and after increasing extracellular [KCl] from 2.5 to 10 mM. Top, control; bottom, 1h preincubation with 10

μM Ru360. Arrowheads indicate single outer segments containing redistributed Ca^{2+}. (B) Mean fluorescence responses of single cone OS (top), CB (middle), and synapses (bottom) during KCl depolarization. Light solid lines, cyto-GCaMP control (4 experiments; n for OS = 47, CB = 44, synapses = 53). Dark solid lines, cyto-GCaMP with Ru360 preincubation (3 experiments; n for OS = 43, CB = 36, synapses = 34). Dashed lines, cyto-GFP control (2 experiments; n for OS = 20, CB = 20, synapses = 20). Blue bars, presence of 10 mM extracellular KCl. (C) Representative confocal image of cyto-GCaMP expressing retinal slices before and after treatment with 1 μM thapsigargin, an inhibitor of ER Ca^{2+} uptake. Top, control; bottom, Ru360 preincubation. Arrowheads indicate single outer segments containing redistributed Ca^{2+}. (D) Mean fluorescence responses of single cone OS (top), CB (middle), and synapses (bottom) during thapsigargin treatment. Light solid lines, cyto-GCaMP control (3 experiments; n for OS = 29, CB = 27, synapses = 30). Dark solid lines, cyto-GCaMP with Ru360 preincubation (3 experiments; n for OS = 29, CB = 37, synapses = 33). Dashed lines, cyto-GFP control (2 experiments; n for OS = 20, CB = 20, synapses = 20). Blue bars, presence of 1 μM thapsigargin. One-way ANOVA was performed at 03:00 and 12:00 for cyto-GCaMP v. cyto-GFP (** = $p < 0.001$) and cyto-GCaMP control v. cyto-GCaMP Ru360 († = $p < 0.05$, ‡ = $p < 0.001$). Error bars represent SE; n represents number of single cells analyzed. Scale bars = 5 μm; timescale = min:sec. OS, outer segment; CB, cell body.

Given the distinct localization of cone ER in the cell body and synapse (George et al., 2014), we hypothesized that blocking ER Ca^{2+} uptake would increase cytosolic $[Ca^{2+}]_i$ in those compartments. While time-lapse imaging, cyto-GCaMP retinal slices were treated with thapsigargin, a sarco-endoplasmic reticulum Ca^{2+} ATPase (SERCA) inhibitor that blocks pumping of Ca^{2+} into the ER (Figure 3.4C, top) (Lytton et al., 1991). Thapsigargin caused rapid and sustained apparent $[Ca^{2+}]_i$ increase in the synapse, where ER regulates Ca^{2+} levels that mediate synaptic vesicle release (Chen et al., 2015), and in the cell body (Figure 3.4D, light solid lines). Thapsigargin also increased mito-GCaMP fluorescence 14 ± 7% 5 minutes after treatment (Table 3.1). However there was no change in outer segment cyto-GCaMP fluorescence indicating that, consistent with ER localization presented in Figure 3D, ER does not directly affect outer segment $[Ca^{2+}]_i$.

We again wondered if mitochondrial Ca^{2+} uptake was insulating the outer segment from cell body $[Ca^{2+}]_i$ fluctuations. When mitochondrial Ca^{2+} uptake is reduced with Ru360, we detected modest but steady apparent increases in outer segment $[Ca^{2+}]_i$ following thapsigargin treatment (Figure 3.4C, bottom arrowheads; Figure 3.4D, dark solid lines).

Thapsigargin did not elicit fluorescence changes in our control indicators, cyto-GFP (Figure 3.4D, dashed lines) and mito-cpYFP (Table 3.1). Together, these results suggest that MCU enables mitochondria to sequester cell body Ca^{2+} and prevent its flow to the outer segment.

Table 3.1. Mitochondrial fluorescence changes of retinal slices following 5 min treatment with Ca^{2+} modulators.

Condition	mito-cpYFP F/F_0, ± SE	mito-GCaMP F/F_0, ± SE	[a] p =
KCl	0.86 ± 0.02 ([b]n = 61)	1.13 ± 0.03 (n = 28)	0.005
thapsigargin	0.86 ± 0.03 (n = 31)	1.14 ± 0.07 (n = 65)	0.038
Na^+ depletion	1.64 ± 0.06 (n = 21)	1.40 ± 0.04 (n = 72)	—
KB-R7943	0.74 ± 0.04 (n = 20)	1.07 ± 0.03 (n = 42)	0.002
sildenafil	0.86 ± 0.08 (n = 37)	1.10 ± 0.05 (n = 60)	0.072
[c]KB-R7943 + sildenafil	—	1.38 ± 0.06 (n = 72)	0.0002
[c]KB-R7943, [c]Ru360 + sildenafil	—	1.09 ± 0.05 (n = 30)	0.003
DMSO	—	0.89 ± 0.04 (n = 9)	—

[a] paired T-test for mito-GCaMP treatment v. DMSO, two-tailed, 99% confidence interval
[b] n indicates number of single mitochondrial clusters
[c] preincubation

Na^+/K^+-Ca^{2+} exchanger activity maintains low outer segment $[Ca^{2+}]_i$.

At the cone plasma membrane, ion exchangers release intracellular Ca^{2+} and bring in extracellular Na^+. The Na^+/K^+-Ca^{2+} exchanger NCKX has high activity and is localized exclusively at the outer segment to support rapid Ca^{2+} clearance during phototransduction. A lower-affinity Na^+-Ca^{2+} exchanger, NCX1, localizes to cone inner segments, but most Ca^{2+} extrusion from the inner segment and synapse happens through plasma membrane Ca^{2+}-ATPases (PMCA) confined to those compartments (Johnson et al., 2007; Krizaj and Copenhagen, 1998). We asked whether mitochondrial Ca^{2+} buffering plays a role in the functional disparity of extrusion mechanisms,

contributing to Ca^{2+} compartmentalization in cones, and used two strategies to address this.

First, we inhibited Ca^{2+} efflux through the plasma membrane exchangers by using perfusion to bathe GCaMP retinal slices in Ringer's solution devoid of Na^+ (Schnetkamp et al., 1991) while time-lapse imaging (Figure 3.5A). Isotonic depletion of Na^+ from the bath caused robust and very rapid increases in cyto-GCaMP fluorescence that initiated at the outer segment and propagated gradually into the cell body, with only a modest and very slow increase in the synapse (Figure 3.5B, solid lines). These findings indicate that outer segment $[Ca^{2+}]_i$ can be maintained at high levels independently of inner segment $[Ca^{2+}]_i$. Na^+ depletion also increased fluorescence of both mito-GCaMP and mito-cpYFP retinal slices (Table 3.1), indicative of changes in mitochondrial membrane potential.

Second, we treated cyto-GCaMP retinal slices with an inhibitor of Na^+/Ca^{2+} exchangers, KB-R7943 (Iwamoto et al., 1996; Vinberg et al., 2015) while time-lapse imaging (Figure 3.5C). Similar to Na^+ depletion, blocking Ca^{2+} extrusion from the exchangers elicited a rapid and sustained increase in outer segment cyto-GCaMP fluorescence followed by a slower increase in the cell body, and only a small, transient response at the synapse (Figure 3.5D, solid lines). Consistent with reports of KB-R7943 promoting mitochondrial Ca^{2+} retention (Wiczer et al., 2014), mito-GCaMP fluorescence rose 7 ± 3% after 5 minutes in KB-R7943, a small but significant increase compared to DMSO alone (Table 3.1). Cyto-GFP retinal slices were unaffected by Na^+ depletion and KB-R7943 (Figures 3.5B and 3.5D, dashed lines). Together, these results suggest that extrusion is compartmentalized, and demonstrate that flow of cytosolic Ca^{2+} between the outer segment and the cell body is regulated.

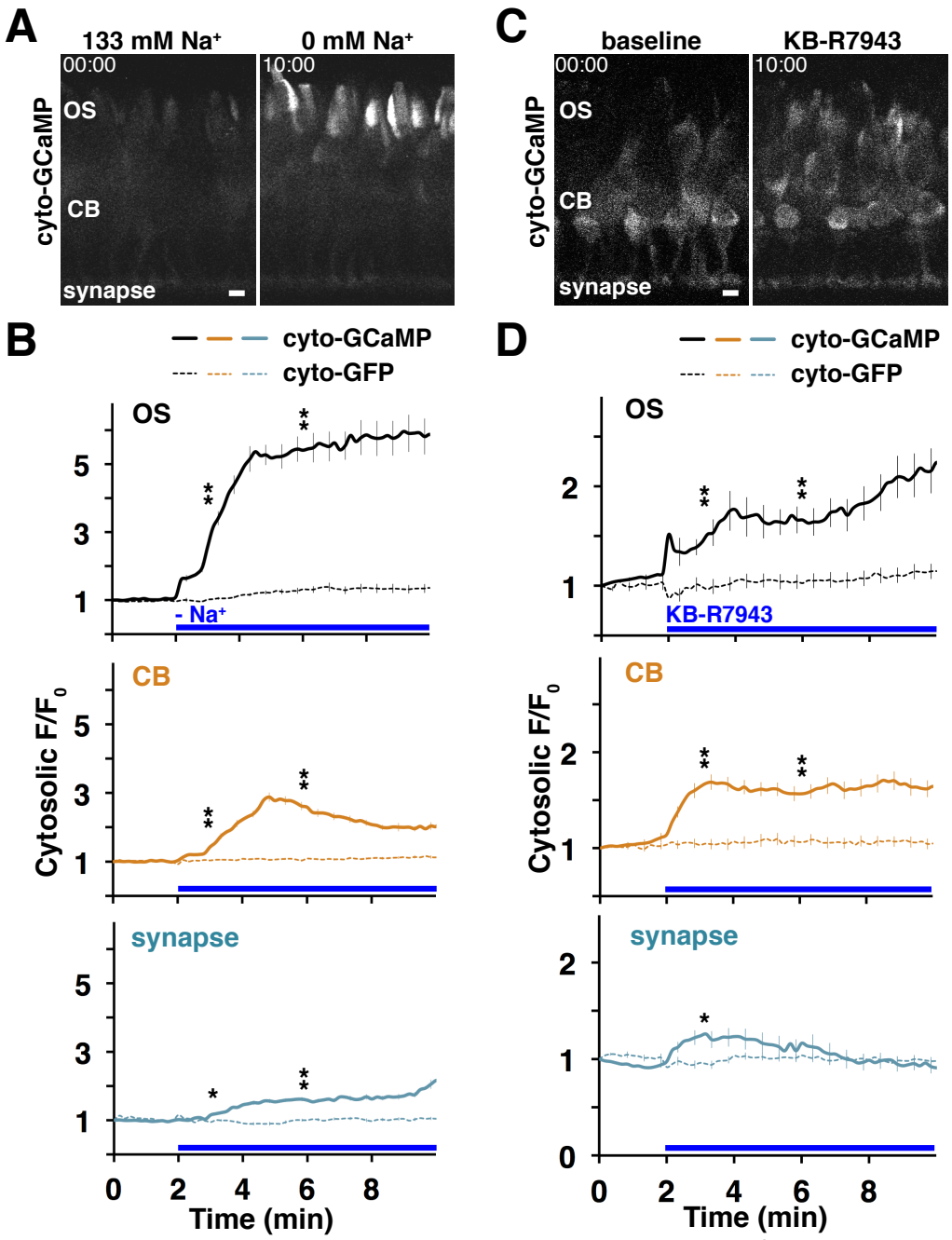

Figure 3.5. Plasma membrane ion exchange can mediate $[Ca^{2+}]_i$ in the cell body and outer segment. (A) Representative confocal image of *in situ* retinal slice from transgenic dark-adapted zebrafish expressing cyto-GCaMP in cones before (left) and after (right) depletion of extracellular Na^+ to halt Ca^{2+} extrusion via Na^+/Ca^{2+} exchangers. (B) Mean fluorescence responses of cone OS (top), CB (middle), and synapses (bottom) during extracellular Na^+ depletion. Solid lines, cyto-GCaMP (3 experiments; n for OS = 77, CB = 68, synapses = 77). Dashed lines, cyto-GFP control (2 experiments; n for OS = 52, CB = 39, synapses = 47). Blue bars, presence of isotonic Na^+-free Ringer's solution. (C) Representative confocal image of cyto-GCaMP expressing retinal slice before (left) and after (right) treatment with 100 μM KB-R7943,

an inhibitor of plasma membrane Na^+/Ca^{2+} exchangers. (D) Mean fluorescence responses of cone OS (top), CB (middle), and synapses (bottom) during KB-R7943 treatment. Solid lines, cyto-GCaMP (3 experiments; n for OS = 19, CB = 30, synapses = 30). Dashed lines, cyto-GFP control (3 experiments; n for OS = 30, CB = 30, synapses = 30). Blue bars, presence of 100 µM KB-R7943. One-way ANOVA was performed at 03:00 and 06:00 for cyto-GCaMP v. cyto-GFP (* = $p < 0.05$; ** = $p < 0.001$). Error bars represent SE; n represents number of single cells analyzed. Scale bars = 5 µm; timescale = min:sec. OS, outer segment; CB, cell body.

Cone mitochondria buffer Ca^{2+} from the outer segment

To establish whether mitochondria buffer outer segment Ca^{2+}, we used sildenafil, an inhibitor of the phosphodiesterase PDE6 (Zhang et al., 2005), to increase outer segment $[Ca^{2+}]_i$ selectively. PDE6 inhibition causes cGMP to build up in the outer segment, opening more cGMP-gated channels and allowing outer segment Ca^{2+} accumulate. Accordingly, treating cyto-GCaMP retina slices with sildenafil brought on a sustained increase in outer segment fluorescence (Figure 3.6A, top). The addition of sildenafil also causes transient increases in both cell body and synapse $[Ca^{2+}]_i$ because influx of cations into the outer segment depolarizes the cell (Figure 3.6B, solid lines). This Ca^{2+} burst diminishes in the cell body and synapse within 5 minutes, but outer segment $[Ca^{2+}]_i$ remains elevated ~ 2-fold. Sildenafil had no effect on fluorescence of cyto-GFP retinal slices (Figure 3.6B, dashed lines).

When mito-GCaMP or mito-cpYFP retinal slices were treated with sildenafil, we noticed an apparent elongation of mitochondrial clusters (Figure 3.6A, bottom), similar to morphological changes brought on by retinomotor movements in prolonged darkness (Burnside et al., 1993). Mito-GCaMP fluorescence of a region at the center of the cluster increased slightly (Figure 3.6F, light solid line), but this change was not significant compared to the vehicle DMSO alone ($p = 0.07$, Table 3.1). Mito-cpYFP fluorescence was insensitive to sildenafil.

To address the possibility of elevated outer segment $[Ca^{2+}]_i$ simply being extruded via NCKX, we performed two-step perfusion experiments. While time-lapse imaging, we first treated retinal slices with the Na^+/Ca^{2+} exchanger inhibitor KB-R7943, allowed

$[Ca^{2+}]_i$ to stabilize for 5 minutes, then applied sildenafil (Figure 3.6C, top row). Subsequent application of sildenafil resulted in larger overall fold changes in cyto-GCaMP fluorescence for all compartments (Figure 3.6D, dashed lines), and a sustained increase in the cell body consistent with inhibition of Ca^{2+} extrusion.

In a similar experiment, mito-GCaMP retinal slices were pretreated with KB-R7943 for 10 minutes then treated with sildenafil (Figure 3.6E, top). This caused a dramatic increase in mito-GCaMP fluorescence (Figure 3.6F, dashed line), suggesting that cone mitochondria can accumulate Ca^{2+} when outer segment $[Ca^{2+}]_i$ is very high. To determine whether this Ca^{2+} uptake is mediated by MCU, we repeated this experiment using retinal slices first preincubated in Ru360 (Figure 3.6E, bottom). 1 hour Ru360 preincubation followed by 10 minutes of additional KB-R7943 preincubation abolished mitochondrial Ca^{2+} uptake (Figure 3.6F, solid dark line), suggesting that this pool of Ca^{2+} enters mitochondria via the MCU.

Finally, we asked how MCU activity was mediating cytosolic Ca^{2+} pools. Using cyto-GCaMP retinal slices preincubated in Ru360, we again performed two-step perfusion experiments with KB-R7943 and sildenafil (Figure 3.6C, bottom row). With both mitochondrial Ca^{2+} uptake and plasma membrane Ca^{2+} extrusion blocked, cyto-GCaMP fluorescence depicted rapid and large increases of $[Ca^{2+}]_i$ in all compartments of the cell (Figure 3.6D, solid lines). Despite their magnitude these large Ca^{2+} bursts were cleared from the cytosol of all compartments, including the outer segment, within minutes. Considering that similar conditions elicit no increase in mito-GCaMP fluorescence (Figure 3.6F, solid dark line), when Na^+/Ca^{2+} exchange is inhibited and $[Ca^{2+}]_i$ is very high activation of PMCA could provide an exit route for cytosolic Ca^{2+}. Although PMCA localizes at the inner segment and synapse (Krizaj et al., 2002), absent MCU activity outer segment Ca^{2+} appears to redistribute throughout the cell.

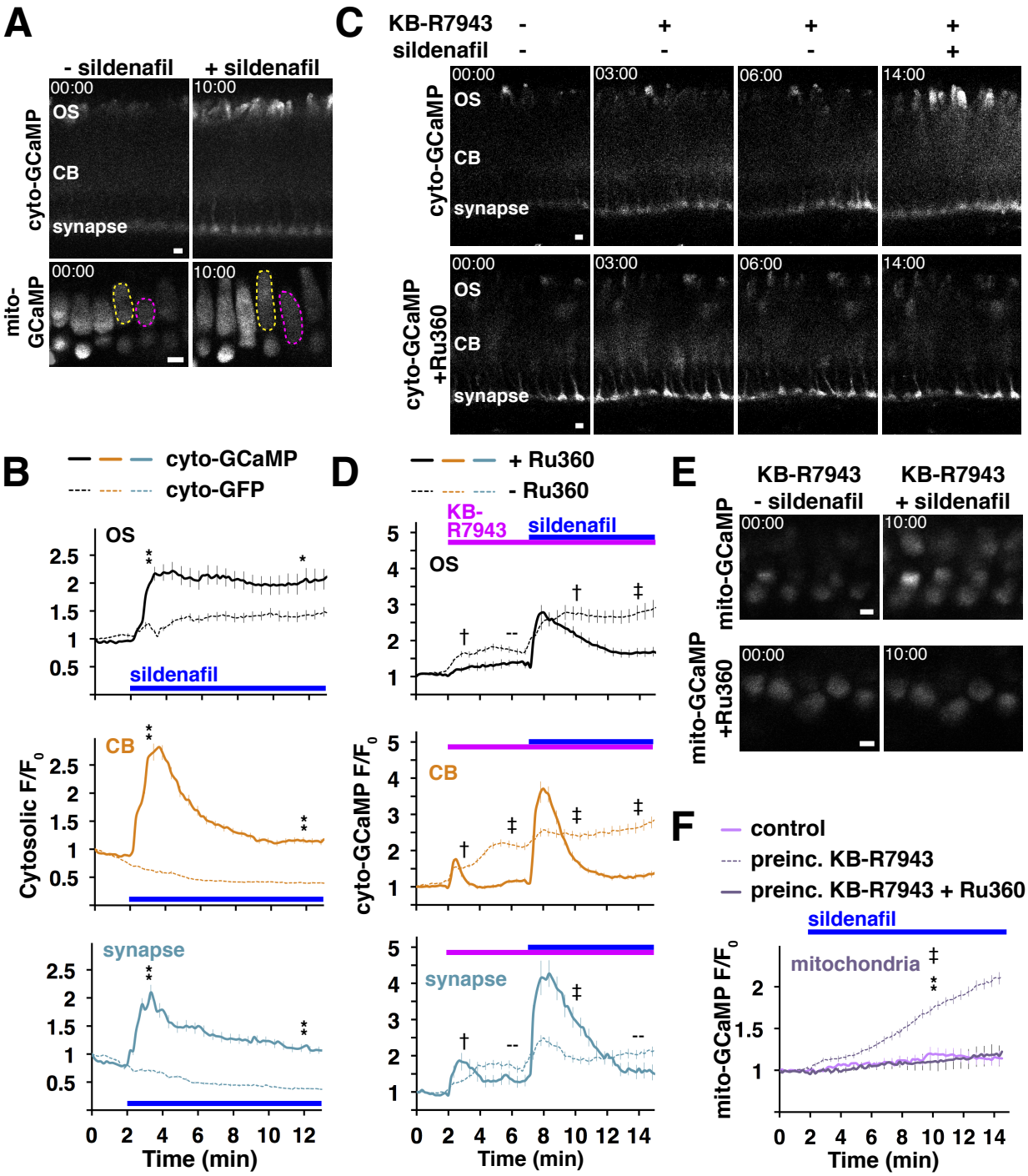

Figure 3.6. Cone mitochondria buffer Ca^{2+} from the outer segment. (A) Representative confocal image of *in situ* retinal slices from transgenic dark-adapted zebrafish expressing GCaMP in cones before (left) and after (right) treatment with 25 µM sildenafil. Top, cyto-GCaMP; bottom, mito-GCaMP with two cone ellipsoids outlined. (B) Mean fluorescence responses of single cone OS (top), CB (middle), and synapses (bottom) during sildenafil treatment. Solid lines, cyto-GCaMP (5 experiments; n for OS = 39, CB = 48, synapses = 50). Dashed lines, cyto-GFP control (2 experiments; n for OS = 20, CB = 20, synapses = 20). Blue bars, presence of 25 µM

sildenafil. One-way ANOVA was performed at 03:00 and 12:00 for cyto-GCaMP v cyto-GFP; * = $p < 0.05$, ** = $p < 0.001$. (C) Confocal image montages of cone cyto-GCaMP expressing retinal slices during sequential treatment with 100 µM KB-R7943, then 25 µM sildenafil. Top, control; bottom, Ru360 preincubation. (D) Mean cyto-GCaMP responses of single cone OS (top), CB (middle), and synapses (bottom) during sildenafil treatment. Solid lines, Ru360 preincubation (3 experiments; n for OS = 40, CB = 38, synapses = 29). Dashed lines, control (6 experiments; n for OS = 65, CB = 69, synapses = 75). Magenta bars, presence of 100 µM KB-R7943; blue bars, presence of 25 µM sildenafil. One-way ANOVA was performed at 03:00, 06:00, 10:00 and 14:00 for cyto-GCaMP control v. cyto-GCaMP Ru360; † = $p < 0.05$, ‡ = $p < 0.001$.
(E) Representative confocal images of cone mito-GCaMP expressing retinal slices preincubated in KB-R7943 before (left) and after (right) treatment with 25 µM sildenafil. Top, mito-GCaMP control; bottom, mito-GCaMP with additional Ru360 preincubation. (F) Mean mito-GCaMP responses from mitochondrial clusters of single cones during sildenafil treatment. Solid light lines, control (6 experiments; n = 60 cells). Dashed lines, KB-R7943 preincubation (5 experiments; n = 76 cells). Solid dark lines, combined KB-R7943 and Ru360 preincubation (3 experiments; n = 30 cells). Magenta bars, presence of 100 µM KB-R7943; blue bars, presence of 25 µM sildenafil. One-way ANOVA was performed at 03:00 and 10:00 for mito-GCaMP control v. KB-R7943 pretreatment (** = $p < 1\times10^{-5}$) and mito-GCaMP KB-R7943 pretreatment v. KB-R7943 with Ru360 pretreatment (‡ = $p < 1\times10^{-5}$). Error bars represent SE; n represents number of single cells analyzed. Scale bars = 5 µm; timescale = min:sec. OS, outer segment; CB, cell body.

These data suggest that mitochondrial Ca^{2+} buffering can insulate the inner segment from a high $[Ca^{2+}]_i$ pool in the outer segment. Under extreme conditions $[Ca^{2+}]_i$ may become high enough to activate MCU in cones, and ER may facilitate Ca^{2+} uptake into a subset of mitochondria. Altogether, our findings show that mitochondria can take up Ca^{2+} from both the outer segment and cell body, effectively separating the two compartments from each other.

Discussion

Compartmentalization of Ca^{2+} has functional implications (Augustine et al., 2003; Yang et al., 2016). In photoreceptors Ca^{2+} has distinct roles and concentrations in different parts of the cell (Krizaj and Copenhagen, 1998; Sampath et al., 1999). Ca^{2+} influences phototransduction in the outer segment, where $[Ca^{2+}]_i$ ranges from 20-50 nM in light to 300-500 nM in darkness (Krizaj and Copenhagen, 2002). In the adjacent cell body, $[Ca^{2+}]_i$ is in the tens of nM range (Krizaj and Copenhagen, 1998), and Ca^{2+} regulates

vital cellular processes such as metabolism (Du et al., 2013b; Glancy and Balaban, 2012; Llorente-Folch et al., 2013; Satrústegui et al., 2007; Wan et al., 1989). How Ca^{2+} concentrations under different physiological conditions are maintained in functionally distinct compartments in polarized neurons, such as photoreceptors, is not understood.

Here we report direct experimental evidence that mitochondria can create functionally and spatially restricted domains of Ca^{2+} in photoreceptors. Using serial block-face SEM and confocal microscopy we establish that within the ellipsoid region of zebrafish cones, a large and tight cluster of many individual mitochondria forms a diffusion barrier between the cell body and outer segment. The cluster is partially surrounded but not permeated by the ER, known to facilitate Ca^{2+} transfer into mitochondria. We show that mitochondria take up Ca^{2+} in response to changes in $[Ca^{2+}]_i$ in both the cell body and outer segment. Preventing Ca^{2+} uptake by blocking MCU function disrupts the formation of distinct cellular Ca^{2+} domains.

Mitochondria of zebrafish cones are poised to buffer Ca^{2+} from either the cell body or the outer segment. Photoreceptor mitochondria are large (Kim et al., 2005; Masuda et al., 2016) and heterogeneous (Tarboush et al., 2014). Our 3-D reconstruction of the ellipsoid region of a zebrafish cone shows that the mitochondrial cluster consists of ~80 tightly packed mitochondria extending nearly to the plasma membrane. This type of structure could act as a physical barrier that restricts flow of ions between the cell body and outer segment; our findings support this idea. We demonstrate that mitochondrial Ca^{2+} levels increase when we selectively increase either outer segment or cell body $[Ca^{2+}]_i$, and that this transfer of Ca^{2+} into mitochondria is at least partially mediated by the MCU. Blocking MCU activity reduced the ability of cone mitochondria to buffer Ca^{2+} and led to a redistribution of cytosolic Ca^{2+} throughout the cell.

The MCU is a complex consisting of the pore-forming MCU subunit and a number of Ca^{2+}-sensitive regulatory proteins that tightly control Ca^{2+} uptake into mitochondria (reviewed by (Kamer and Mootha, 2015). This protein complex is thought to be the primary route by which Ca^{2+} enters mitochondria, and when it is knocked out Ca^{2+} uptake into mitochondria is greatly reduced (Pan et al., 2013). From studies in other

tissues, the affinity of the MCU for Ca^{2+} appears weak, reported to be between 10-25 μM $[Ca^{2+}]_i$ (Gunter and Gunter, 2001; Williams et al., 2013). Expression of activating and deactivating MCU subunits can influence MCU activity and varies widely among cell types (Geiger et al., 2013; Murgia and Rizzuto, 2015), but the stoichiometry of these key regulators in the photoreceptor MCU complex is not known.

ER may facilitate Ca^{2+} uptake into cone mitochondria facing the cell body. In many cell types, a dynamic and extensive network of ER-mitochondrial contacts enables mitochondrial Ca^{2+} uptake by concentrating Ca^{2+} at these junctions (Hamasaki et al., 2013; Rutter and Pinton, 2014). IP_3 receptors on the ER surface release Ca^{2+} immediately adjacent to mitochondria (Rowland and Voeltz, 2012) generating high localized Ca^{2+} concentrations. Ca^{2+} then passes through voltage-dependent anion channels (VDACs) in the outer mitochondrial membrane generating domains of high $[Ca^{2+}]_i$ that are sufficient for activation of the MCU (Contreras et al., 2010; Qi et al., 2015).

We found that the ER of zebrafish cones surrounds only the basal and lateral parts of the mitochondrial cluster, but does not appear to penetrate the cluster or extend between the apical side and outer segment. This finding is generally consistent with a previous analysis of ER in amphibian cones (Mercurio and Holtzman, 1982). For the subset of cone mitochondria facing the cell body, where $[Ca^{2+}]_i$ is tens of nM, Ca^{2+} uptake likely occurs at or near ER contact sites. Consistent with this, when we depolarize cones with KCl or block ER Ca^{2+} uptake via SERCA there is no effect on outer segment $[Ca^{2+}]_i$, while synaptic, inner segment and mitochondrial Ca^{2+} levels increase. Further, recent work showed that Ca^{2+} moves freely through the ER enabling bidirectional flow of Ca^{2+} between the cell body and the synapse (Chen et al., 2015). This would provide a potential route for synaptic Ca^{2+} to enter mitochondria via MCU

Mitochondrial Ca^{2+} uptake insulates the cell body from high outer segment $[Ca^{2+}]_i$. The physiological range of free $[Ca^{2+}]_i$ in the outer segment under peak signaling conditions is in the range of tens to hundreds of nM (Krizaj and Copenhagen, 2002), below the affinity of MCU. In addition, plasma membrane Ca^{2+} extrusion from the outer segment

via NCKX is significantly faster than extrusion of Ca^{2+} out of the cell body via NCX or PMCA (Krizaj and Copenhagen, 1998) . This would suggest that under normal physiological conditions, outer segment Ca^{2+} is removed primarily through outer segment NCKX (Krizaj et al., 2002) and may not depend on mitochondrial Ca^{2+} buffering. Our results suggest that mitochondria mediate high outer segment $[Ca^{2+}]_i$ that might occur during photoreceptor disease.

We found a large capacity for mitochondrial Ca^{2+} buffering under pharmacological conditions that both blocked Ca^{2+} extrusion and forced outer segment Ca^{2+} influx to mimic darkness. These conditions elicited an outer segment $[Ca^{2+}]_i$ increase that approached saturation of our cytosolic Ca^{2+} sensor, and increased fluorescence of the mitochondrial Ca^{2+} sensor nearly 2-fold, the largest change seen in this study. Higher resolution imaging methods and detailed information about MCU localization across the mitochondrial cluster are needed to address whether outer segment Ca^{2+} enters mitochondria directly near the base of the ciliary stalk, or must first diffuse laterally toward the ER to be taken up into mitochondria.

The course of retinal degeneration could be influenced by mitochondrial Ca^{2+} uptake. Our results suggest that mitochondrial Ca^{2+} buffering plays an integral role in photoreceptor survival during degenerations marked by elevated outer segment $[Ca^{2+}]_i$. The *pde6c*^{w59} zebrafish model, which lacks cone PDE6 (Stearns et al., 2007), undergoes retinal degeneration that was predicted to occur via increased cytosolic $[Ca^{2+}]_i$. Interestingly, cytosolic $[Ca^{2+}]_i$ was not increased during cell death (Ma et al., 2013), and our results suggest that elevated outer segment $[Ca^{2+}]_i$ brought on by the mutation may have been buffered by mitochondria. Examination of Ca^{2+} uptake by mitochondria in retinal disease models will define the contributions of mitochondrial Ca^{2+} buffering to disease progression and degeneration.

Photoreceptors of *Nckx1*$^{-/-}$ mice, which lack rod outer segment NCKX, degenerate very slowly, showing thinning of retinal layers over the course of one year (Vinberg et al., 2015). These mice exhibit a delayed recovery of rod photoresponse. Absent an efflux route at the plasma membrane, Ca^{2+} can still slowly leave the outer segment. A recent

study of *Nckx2*$^{-/-}$ mice lacking cone outer segment NCKX demonstrated a similar delay in recovery of cone photoresponse but cones do not degenerate (Sakurai et al., 2016). Taken together, these studies are consistent with a previous observation that cone mitochondria may have more Ca^{2+} buffering capacity than rods (Szikra and Krizaj, 2007). We found that cone mitochondria can accumulate Ca^{2+} via MCU, which could contribute to photoresponse recovery in these mutants. Knockout models lacking the MCU and modulators of mitochondrial Ca^{2+} uptake will help determine whether Ca^{2+} uptake by mitochondria influences photoresponse recovery.

In summary, cone photoreceptor mitochondria can influence $[Ca^{2+}]_i$ in the cell body and outer segment. This is important for isolating functional information within distinct photoreceptor compartments. Ca^{2+} buffered by mitochondria located on the cell body side of the cluster may regulate protein synthesis and metabolic processes through protein acetylation and NADH production. Mitochondrial Ca^{2+} buffering from the outer segment may be a small but important component of light adaptation, as recovery of photocurrent following sustained increases in light could be influenced by mitochondrial uptake of outer segment Ca^{2+}. Ca^{2+} buffering via mitochondria could also influence the health and survival of photoreceptors during degeneration due to disease-causing mutations. Future studies should evaluate the contributions of mitochondrial Ca^{2+} import to photoreceptor metabolism, light adaptation, and disease.

Materials & Methods

Zebrafish maintenance

Research was authorized by the University of Washington Institutional Animal Care and Use Committee. Transgenic heterozygotes in the AB or Roy$^{-/-}$ genetic background were maintained in the University of Washington South Lake Union aquatics facility at 27.5 ºC on a 14h/10h light-dark cycle. Fish used for experiments were male and female siblings between 9-20 months old.

Generation of transgenic zebrafish

The transgenic lines *Tg(gnat2:GCaMP3)* (Ma et al., 2013) (Ma et al., 2013), *Tg(gnat2:ER-GFP)* (George et al., 2014) (George et al., 2014), and *Tg(gnat2:EGFP)* (Kennedy et al., 2007) (Kennedy et al., 2007) have been described previously. DNA constructs expressing mito-GCaMP3 (Esterberg et al., 2014) or mito-cpYFP (Wang et al., 2008) downstream of the zebrafish cone transducin promoter *gnat2* were generated using the Gateway-Tol2 system (Kwan et al., 2007). These constructs were injected into embryos at the 1-2 cell stage with Tol2 transposase mRNA. Mosaic larvae isolated at 5 days post-fertilization were raised to adulthood and a germline carrier with a single insertion was identified for each strain, *Tg(gnat2:mito-GCaMP3) and Tg(gnat2:mito-cpYFP)*.

Zebrafish retinal slice preparation

Transgenic adult zebrafish were dark adapted >1 h, euthanized, enucleated, and the retinas immediately dissected away under red light into cold oxygenated Ringer's solution (133 mM NaCl, 2.5 mM KCl, 1.5 mM NaH_2PO_4, 2 mM $CaCl_2$, 1.5 mM $MgCl_2$, 10 mM HEPES, 10 mM D-glucose, 1 mM sodium lactate, 0.5 mM L-glutamine, 0.5 mM reduced glutathione, 0.5 mM sodium pyruvate, 0.3 mM sodium ascorbate, pH 7.4). Isolated retinas were mounted on filter paper (0.45 µm pore, mixed cellulose, Millipore), flattened with gentle suction, stained 10 min at 20-22 °C with dilute BODIPY 558/568 C12 (Molecular Probes) and washed with excess Ringer's solution. Flat-mounted retinas were either imaged directly, or sliced into 400-µm slices using a tissue slicer (Stoelting). Slices were rotated 90° and the filter paper edges buried in strips of wax on a coverslip for imaging experiments. To assay cell viability, retinal slices without BODIPY were stained with 7.5 µM propidium iodide (PI, Invitrogen) 20 min at 20-22°C and washed three times prior to imaging.

Ca^{2+} imaging

Retinal slices were imaged in either static Ringer's solution, or in a flow chamber attached to an injection apparatus and perfusion system flowing freshly oxygenated Ringer's solution between 20-22 °C. Experiments involving Ca^{2+} free conditions were conducted with a modified Ringer's solution containing 0.4 µM EGTA instead of $CaCl_2$

(pH 7.4). Experiments involving Na^+-free conditions were conducted using another modified isotonic Ringer's solution (147 mM Tris, ~120 mM HCl, 1 mM KCl, 2 mM $CaCl_2$, 1.5 mM $MgCl_2$, 1.5 mM KH_2PO_4, 10 mM HEPES, 10 mM D-glucose, 0.5 mM L-glutamine, 0.5 mM reduced glutathione, pH 7.4). Flat mounts and slices were imaged on either an Olympus FV1000 or Leica LSP8 confocal microscope with a 40X water objective; excitation/emission wavelengths were 488/510 nm for fluorescent proteins, and 559/594 nm for BODIPY and PI. Olympus FluoView (RRID:SCR_014215) or Leica LAS-X (RRID:SCR_013673) software was used to acquire images, and time-lapses were imaged every 10 s. For quantification of absolute mito-GCaMP fluorescence, z-stacks of retinal sections were generated from 10-20 1 µm slices.

Pharmacological treatments

Ca^{2+} modulators were injected into the perfusion chamber after two minutes of baseline time-lapse imaging, followed by a single pump of the syringe to aid mixing. For KCl depolarization experiments, a concentrated solution of KCl in Ringer's solution was injected into perfusion chamber to reach a final concentration of 10 mM. Sildenafil citrate (Sigma) was stored in DMSO at 20 mM and used at a working concentration of 25 µM. Thapsigargin (Sigma) was stored in DMSO at 10 mM and used at a working concentration of 1 µM. 50 mM KB-R7943 mesylate (Tocris) was prepared fresh each day in DMSO and used at final concentration of 100 µM. Ru360 (Millipore) was prepared fresh for each experiment, first dissolved in cold deoxygenated water to 5 mM and stored on ice < 3 h; immediately prior to incubation it was diluted in Ringer's solution to 10 µm. Where indicated, retinal slices were incubated 1 h in 10 µm Ru360 at 20-22°C before imaging, and maintained in 10 µm Ru360 throughout the duration of experiments.

Electron microscopy

Adult zebrafish eyes were enucleated, the anterior half was dissected away, and the eyecup was cut in half. Tissue was fixed in 4% glutaraldehyde in 0.1M sodium cacodylate buffer pH 7.2 at room temperature (RT), then stored overnight at 4 °C. Samples were washed four times in sodium cacodylate buffer, postfixed in osmium ferrocyanide (2% osmium tetroxide/3% potassium ferrocyanide in buffer) for 1 h on ice,

washed, incubated in 1% thiocarbohydrazide for 20 m, and washed again. Following incubation in 2% osmium tetroxide for 30 min at RT, samples were washed and en bloc stained with 1% aqueous uranyl acetate overnight at 4°C. Samples were finally washed and en bloc stained with Walton's lead aspartate for 30 min at 60°C, dehydrated in a graded ethanol series, and embedded in Durcupan resin. Serial sections were cut at 60 nm thickness, and imaged with 6 nm pixel size using a Zeiss Sigma VP scanning electron microscope fitted with a Gatan 3View2XP ultramicrotome apparatus. Imaged stacks were concatenated and aligned using TrakEM2 (RRID:SCR_008954). Unless stated, five washes with water were used for all wash steps.

Image processing and analysis

Time-lapse images were analyzed using ImageJ software (RRID:SCR_002285). Time-lapses were corrected for XY drift using the MultiStackReg plugin, and regions of interest (ROIs) selected around individual cell compartments. Separate red and green kymographs were generated as described previously (Ma et al., 2013) from ROIs for the synapse, cell body and outer segment, or ellipsoid regions and were used to quantify fluorescence changes in single cells. Data were compiled using Microsoft Excel. To account for focal plane variance and drift in the z-direction, the green GCaMP fluorescence signal was divided by the red BODIPY fluorescence signal at each time point. Fold change was calculated from t=0 using the equation $F/F_0 = (510_t/594_t)/(510_0/594_0)$. For z-stacks, absolute mito-GCaMP fluorescence was measured from frames at the widest part of individual mitochondrial clusters. Brightness and contrast were adjusted equally in the presented images to ease visualization.

Statistics

Results are reported as mean ± standard error of the mean (SE). R (RRID:SCR_001905) with R Commander (Fox, 2005) was used to perform one-way ANOVA for multiple comparisons, or two-tailed T-tests with a 99% confidence interval for pairwise comparisons.

Acknowledgments

The work described in this chapter was published in the Journal of Neuroscience. The other authors that contributed to this study were Whitney M. Cleghorn (co-first author), Stephanie R. Sloat, James B. Hurley, and Susan E. Brockerhoff. We thank Ed Parker for generating serial block-face SEM images, Ralph Nelson for guidance in preparing adult zebrafish retinal slices, and Eva Ma and Gail Stanton for assistance generating mito-GCaMP and mito-cpYFP transgenic zebrafish. This work was supported by NSF GRFP #2013158531 (M.G.), NIH NEI 5T32EY007031 (W.C. and M.G.) and EY026020 (J.H. and S.B.).

Chapter 4

Preparing fresh retinal slices from adult zebrafish for *ex vivo* imaging experiments

Introduction

The zebrafish (*Danio rerio*) has become widely used in medical and basic scientific research (Lieschke and Currie, 2007), owing to its small size, rapid development and vertebrate organ systems. The natural transparency of zebrafish larvae combined with established methods for transgenesis have enabled detailed visualization of cellular processes in a living animal. A number of genetically encoded fluorescent biosensors have been targeted to specific zebrafish cells to detect Ca^{2+} (Ma et al., 2013), hydrogen peroxide (Niethammer et al., 2009), apoptotic activation (Andrews et al., 2016) and ATP (Kioka et al., 2014).

In vivo imaging of zebrafish larvae has led to breakthroughs in the field of neuroscience, including mapping of brain circuitry (Muto et al., 2013) and drug development for central nervous system disorders (Stewart et al., 2014). Zebrafish are well suited for vision research because their retinas feature the laminar structure and neuron types of higher vertebrates, and they display robust visual behaviors (Neuhauss, 2002; Zou et al., 2010). Several types of retinal degenerations analogous to human disease have been modeled successfully and studied in zebrafish (Gross and Perkins, 2007; Stearns et al., 2007), including live imaging of individual photoreceptors degenerating within a retina (Lewis et al., 2010; Ma et al., 2013).

While *in vivo* larval zebrafish imaging is a valuable tool, it becomes more challenging as fish grow and develop pigmentation, and some pharmacological treatments cannot permeate an entire animal. Further, certain cellular processes change with development and age, making later time points critical for understanding function and the progression of disease in adult animals. Biochemical methods such as immunoblot, quantitative PCR, O_2 consumption, and metabolomic analyses can provide important

clues about biology of the retina as a whole, but it is difficult to discern contributions of individual cell types affected by disease. Imaging isolated retinal tissue *ex vivo* bypasses these issues, and while imaging flat mounted retinas affords a view of the outer retina (Wang et al., 2014), deeper inner retinal features are obscured. Transverse retinal slices, such as those presented in fixed immunohistochemical analyses, enable a clear view of all layers and cell types but only offer a single snapshot in the dynamic processes involved in normal function and disease.

Here, we present a method for generating *ex vivo* transverse retinal slices from adult zebrafish for imaging. It is similar to methods for preparing amphibian and zebrafish retinal slices for electrophysiological and morphological studies (Connaughton, 2003; Van Hook and Thoreson, 2013), with important modifications for time-lapse imaging *ex vivo* using confocal microscopy. Fluorescence responses of biosensors or dyes in slices are monitored in real time with a confocal microscope while delivering pharmacological agents using perfusion. While the method was developed for imaging photoreceptors, it may be feasible to use it for visualizing Müller cells, bipolar cells, horizontal cells, amacrine cells, or retinal ganglion cells with appropriate fluorescent markers. Additionally, slices can be loaded with fluorescent cell-permeable dyes to report cell viability, vesicular transport, mitochondrial function, or redox state. This versatile preparation allows visualization of a wide range of subcellular processes throughout the retina, including Ca^{2+} dynamics, signal transduction and metabolic state.

Protocol

All animal experiments were approved by the University of Washington Institutional Animal Care and Use Committee.

1. Preparing Animals and Equipment

1.1. The retinal pigment epithelium (RPE) is a dark sheet of tissue surrounding the outside of the retina whose pigmentation can obscure retinal features and damage the tissue when confocal imaging *ex vivo*. In darkness the RPE of zebrafish is retracted away from the retina; dark adapt fish to facilitate future removal of the RPE from the retina before slicing and imaging.

1.1.1. Transfer fish to a spawning tank filled with fish water, then wrap the spawning tank with dark fabric or place it in a dark cabinet.

1.1.2. Dark adapt zebrafish for at least 1 h prior to euthanasia to allow near complete separation of RPE from the retina. 30 min dark adaptation is sufficient to remove most RPE, though pieces of it may remain intercalated between photoreceptors.

1.2. Melt ~ 15 mL petroleum jelly in a 50 mL beaker on a hot plate and then draw 3 mL liquid into a 3-mL slip tip syringe. Invert syringe, place in a test tube rack, and allow petroleum jelly to cool.

1.3. Make a reusable slicing chamber on a plain 7 cm X 2.5 cm microscope slide.

1.3.1. Using clear nail polish, paint narrow lines to create a 3 cm X 2.5 cm rectangle in the center of the slide, allow it to dry, and then add another layer of nail polish to the lines.

1.4. Prepare imaging ladders on cover slips to hold slices during imaging. The slices will form the “rungs” of the ladder.

1.4.1 For static imaging or injection experiments with minimal solution flow, make petroleum jelly ladders consisting of two flat wide parallel strips of petroleum jelly on 18 mm square glass cover slips. Use the syringe to apply two flattened ~ 1 cm long smears of cooled petroleum jelly 0.5 cm apart on the cover slip.

1.5. Ready the tissue slicer.

1.5.1. Clean a double edge razor blade with ethanol and allow it to air dry. Cut it into quarters with scissors, first lengthwise into halves then across each blade.

1.5.2. Place the slicing chamber on the stage of the tissue slicer, center it horizontally on the stage and mark a long edge with permanent marker for alignment.

1.5.3. Load a blade section onto the tissue slicer arm, ensure the blade lies flat and centered on the slide without touching the nail polish, then gently tighten the blade apparatus. Lower the blade arm by adjusting the knob ¼ turn, then place a scrap of filter paper in the center of the imaging chamber and test cut it. If the paper isn’t cut fully through remount the blade.

1.6. Using the syringe, place a single small dot of cooled petroleum jelly in a 10 cm petri dish ~ 1.5 cm to the right of the center. Press an imaging ladder into it using forceps with the petroleum jelly facing up. Make another small petroleum jelly dot ~ 1 cm from the inlet edge of the imaging chamber.

1.7. Fit the petroleum jelly syringe with a 20g needle and uncap it. Hold the needle onto the syringe and use it to make two 1 cm long thin parallel strips of petroleum jelly lengthwise in the center of the slicing chamber. Space the strips ~ 1 cm apart.

1.8. Make a reusable wire eye loop tool by wrapping the center of a ~ 4 cm segment of 30g tungsten wire around a pair of closed forceps once tightly. Adjust the diameter of the loop by sliding the wire up or down the forceps until it is slightly larger than a zebrafish eye, typically ~ 2-3 mm. Twist the wire ends and secure them to the end of a 6 cm wooden stick using laboratory tape.

1.9. Prepare Ringer's solution.

1.9.1. Thaw 50X supplement stock solution (Table 4.1) and add it fresh to HEPES-buffered, non-bicarbonate Ringer's solution (Table 4.2) the morning of the experiment; dilute 200 µL of supplement stock solution in every 10 mL of Ringer's solution in a conical centrifuge tube or sterile glass bottle. For static imaging experiments, prepare at least 30 mL of Ringer's solution per experiment. The volume of Ringer's solution needed for perfusion experiments will depend on the flow rate and total experiment time.

1.9.2. Check that the pH of the supplemented solution is 7.4 using a digital pH probe or pH paper, and adjust accordingly with dilute NaOH or HCl.

1.9.3. Oxygenate supplemented Ringer's solution on ice by bubbling with 100% oxygen gas for at least 5 min using a standard medical oxygen tank and regulator fitted with a hose, or the optional gas bubbler manifold used for perfusion. Store oxygenated Ringer's solution on ice in a sealed conical centrifuge tube or sterile glass bottle near the dissection microscope; use this solution for dissection, imaging, and to dilute dyes or pharmacological agents.

1.9.4. If other solutions are being used in the experiment, such as Na^+-free Ringer's solution (Table 4.3), repeat steps 1.9.1.-1.9.3.

1.10. Gather petri dishes, forceps, micro-scissors and other tools near the dissection microscope, and prepare a fish water ice bath for zebrafish euthanasia.

2. Preparing retinal slices (see Fig 4.1)

2.1. Working under red ambient light to minimize light adaptation (which can make the RPE stick more tightly to the retina), euthanize zebrafish by immersion in the ice bath until touch response is lost (typically 1-2 min), then transfer the fish to a petri dish. Cervically dislocate but do not decapitate the fish with a scalpel.

2.2. Use the wire loop to loosen connective tissue around one eye, then pull the eye forward gently with the loop in one hand. Using micro-scissors in the other hand, cut the white optic nerve under the eye, taking care not to cut the back of the eye.

2.3. Transfer the eye using forceps to a petri dish of cold Ringer's solution on ice, and repeat for the second eye. Keep the eyes in darkness or under red light until RPE is removed.

2.4. Dissect eyecups under a low power dissection microscope in a drop of cold Ringer's solution on a plain glass slide in a petri dish.

2.4.1. Pierce the cornea with fine forceps, then gently remove pieces of clear, brittle cornea and silvery sclera with forceps or scissors. Remove and discard the lens and most of the sclera (see Fig 4.1A), and handle the isolated eyecup minimally.

2.4.2. Pieces of fat, small bits of sclera, and black RPE can remain attached to the eyecup and removed from the retina later. Should the retina separate from the RPE in step 2.4.1. proceed with the same steps and use extra caution not to damage the delicate isolated retina.

2.4.2. Position eyecup open side down (RPE up) on the slide, and cut into thirds or quarters with a fresh single edge razor blade in one motion (see Fig 4.1B). Discard pieces of tissue that are highly curved.

2.5. Flat mount retina on filter paper.

2.5.1. Wet a piece of filter paper with Ringer's solution and place it on the slide next to the eyecup pieces. Use flat forceps when handling the intact wet filter paper to avoid puncturing it. Add cold Ringer's solution to cover both the filter paper and tissue.

2.5.2. Using forceps in each hand, carefully drag the filter paper underneath each eyecup piece with the RPE and photoreceptors facing up, i.e. with the back of the eye facing up. Position the eyecup pieces in a single line along the center of the filter paper (see Fig 4.1C). Handle the eyecup pieces gently with fine forceps only near an edge or corner.

2.5.3. To help retinas adhere to the filter paper, place the wet filter paper on a dry paper towel for 3 sec to wick moisture downward, but don't let the tissue become dry. Repeat until eyecup pieces lie flat on the filter paper. Applying gentle suction to the underside of the filter paper helps flatten the retina, but this step is not essential.

2.6. If black sheets of RPE remain on the eyecup pieces, use fine forceps to gently peel it away starting from one corner (see Fig 4.1D) while the tissue is sitting in a drop of Ringer's solution. Should the retina lift off the filter paper, repeat the wicking step in 2.5.3. The retina may appear pink due to unbleached visual pigments.

2.7. Repeat retina dissection and flat mounting steps in 2.4-2.6 for the second eye, if desired, keeping the first flat-mounted retina immersed in cold Ringer's solution. To streamline the slicing procedure, pieces of both retinas may be placed on one filter

paper. Once the RPE has been removed, the protocol can be carried out under normal room light unless experiments necessitate darkness.

2.8. Place the filter paper on a slide and trim it into a rectangle with a single edge razor blade, leaving ~ 0.5 cm of filter paper on either side of the line of retinas. Move the filter paper to the prepared slicing chamber, push the long filter paper edges into the thin petroleum jelly lines using forceps, and immerse the retinas in 3-4 drops of cold Ringer's solution.

2.9. Some dyes, such as lipophilic dyes, are best loaded into flat mounts at this stage prior to slicing. These can be loaded, wicked away with a tissue, and washed in the slicing chamber.

2.9.1. For instance, C^{12} 558/568 BODIPY™ intensely stains retinal cell membranes and photoreceptor outer segments (see Fig 4.4A) when loaded at ~ 5 µg / mL for 15 min at room temperature (typically 23-27 ºC), followed by a wash in excess Ringer's solution.

2.10. Transfer the slicing chamber to the tissue slicer stage, position the long edge along the marked line, and secure the chamber ends to the stage with laboratory tape. Starting at one end, cut the retina and filter paper using firm, gentle pressure on the slicing arm. Check that the first slice was cut fully, then use the micrometer to cut ~ 400 µm slices.

2.11. Assemble the imaging ladder.

2.11.1. Place the slicing chamber with sliced retinal sections in the petri dish from step 1.7 adjacent to the imaging ladder. Fill the dish with cold Ringer's solution to submerge its contents (see Fig 4.1E).

2.11.2. Using forceps and keeping slices submerged, gently transfer strips of filter paper and retina to the ladder by sliding the petri dish from left to right. Take care not to touch retinas directly. Rotate the slices 90º and bury the filter paper edges in petroleum jelly.

2.11.3. Finely position retinal slices in the ladder with forceps so that retinal layers are clearly visible under the dissection microscope (see Fig 4.1G). For slices on each end of the ladder, ensure that the tissue is facing inward toward the other slices to minimize motion of the tissue during injection or flow. Discard any retinal slices that are not well adhered to the filter paper (see Fig 4.2A).

2.12. If desired, dyes can be loaded into retinal slices at this stage and washed in excess Ringer's solution prior to imaging.

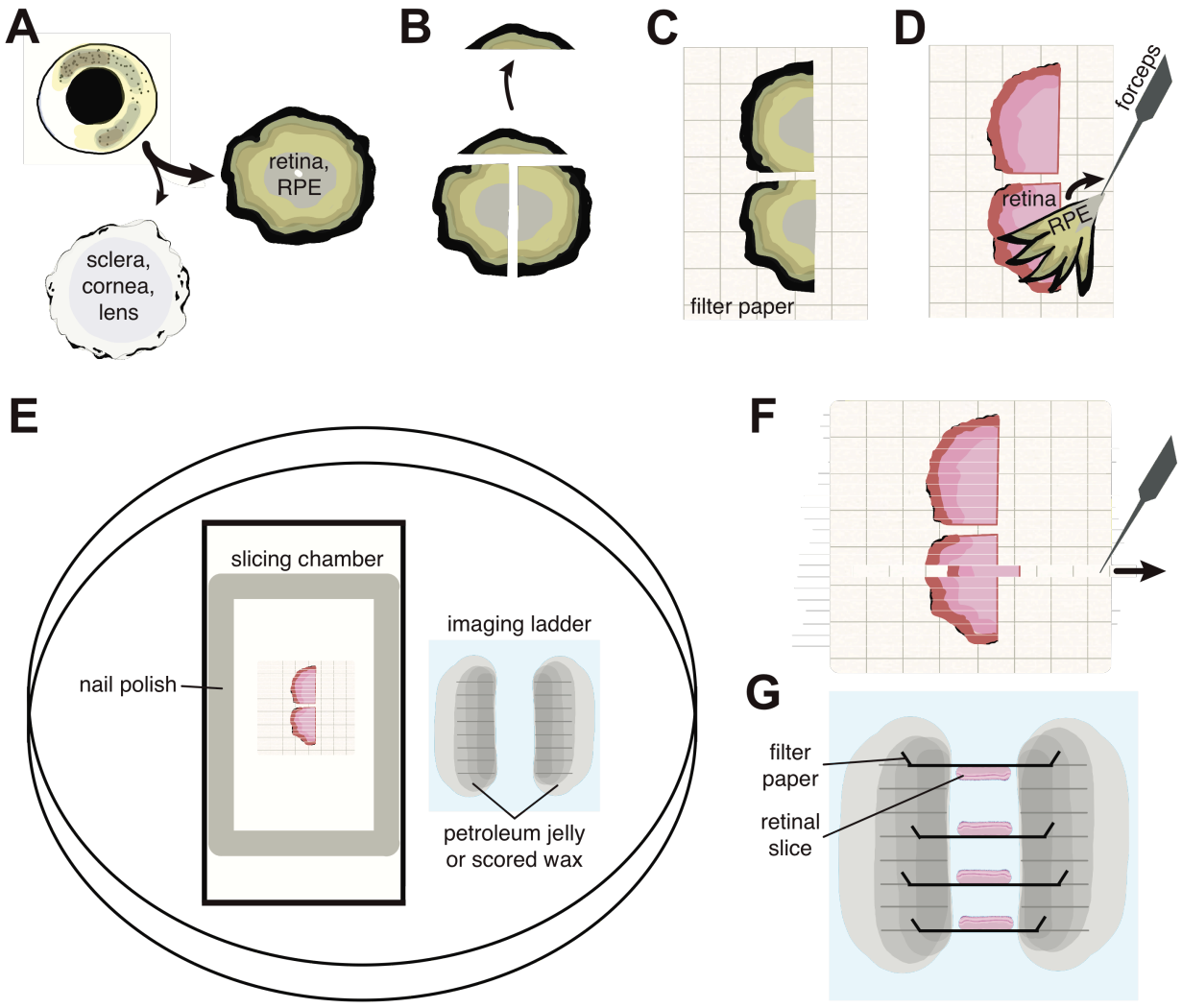

Figure 4.1. Schematic for preparing fresh zebrafish retinal slices. (A) Dissect away the eyecup, and discard lens and sclera (step 2.4.1). (B) Cut the eyecup into three pieces; discard small edge piece (step 2.4.2). (C) Drag filter paper under eyecup pieces with the inner retina facing toward the filter paper (step 2.5.1-2.5.2). (D) Flatten retina by using a paper towel to wick Ringer's solution downward through the filter paper (step 2.5.3), then gently peel away remaining RPE with forceps (step 2.6). Move the filter paper to the slicing chamber on the tissue slicer stage and cut 400 µm slices (steps 2.8, 2.10). (E) Transfer slicing chamber with slices and a wax or petroleum jelly ladder to a petri dish of Ringer's solution (step 2.11.1). (F) Use fine forceps to slide single slices from the slicing chamber to the ladder while keeping slices submerged. (G) Rotate filter paper strips (black) 90º and bury the edges of the filter paper in wax or petroleum jelly (steps 2.11.2-2.11.3). (H) Schematic of the final imaging chamber loaded with a ladder and slices.

2.12.1. Propidium iodide (PI) and Hoechst 33342 robustly stain nuclei of dead and all cells, respectively (see Fig 4.2B), when incubated with retinal slices at 5 µg / mL for 20

min at room temperature. Tetramethylrhodamine (TMRM) accumulates in actively respiring mitochondria throughout the retina when incubated at 1 nM for 30 min at room temperature.

2.13. While the slices are staining, prepare the imaging chamber and injection apparatus. Use the syringe to flush the tubing with Ringer's solution and purge bubbles, attach the open end of the tubing to the imaging chamber inlet, and close the stopcock. Remove the syringe and fill it with reagent(s) for injection, then reattach it to the tubing.

2.14. Use forceps to transfer the coverslip with retinal slices to the imaging chamber, pressing the coverslip into the dot of petroleum jelly near the inlet edge of the imaging chamber (see Fig 4.1H). Fill the imaging chamber with Ringer's solution to cover slices.

3. Imaging retinal slices

3.1. Place the filled imaging chamber with the connected injection apparatus on the stage of an upright confocal microscope equipped with a 20 or 40X water dipping lens. Secure the imaging chamber with stage clips.

3.2. Lower the dipping lens over the ladder, and focus on a slice at one end of the ladder under dim trans-illuminated light. Examine each slice for transverse orientation, presence of photoreceptor outer segments, and secure adhesion to the filter paper.

3.3. Select the best slice for time lapse imaging and configure the microscope software for time lapse image acquisition. Table 4 outlines typical imaging settings for various fluorescent markers and dyes.

3.3.1. The rate of image acquisition will vary depending on the microscope, fluorescent marker(s), and biological process being studied. For instance, 800x800 pixel resolution, 2 µs/pixel scan speed, and a 10 sec frame rate is sufficient for imaging calcium dynamics in photoreceptors with GCaMP3 and a red dye.

3.3.2. If available, use the software to trace physical landmarks in the slice (photoreceptor outer segments, cell bodies, nuclei) to aid potential reorientation during the time lapse. Also set up the software to monitor real-time fluorescence across the slice.

3.4. Begin imaging and monitor baseline fluorescence. When fluorescence across the slice stabilizes (typically within 2-5 min), proceed with the experiment. For injection, open the syringe stopcock, then slowly depress and draw back on the plunger twice to aid mixing.

3.4.1. For instance, mitochondrial function can be abolished by injecting a concentrated solution of the protonophore CCCP to reach a final concentration of 1 µM in the imaging chamber. This induces a robust Ca^{2+} burst in photoreceptor cytosol reported by

GCaMP, then a steady decrease in mitochondrial membrane potential reported by TMRM.

3.5. Closely monitor slices for drift during the experiment, and use the software to make micro-adjustments according to physical landmarks. Typically drift in the Z-direction during injection or perfusion is < 5 μm.

4. Imaging retinal slices during perfusion experiments where solutions are changed or flowed continuously is similar to setup for static imaging or injection experiments, with the following modifications.

4.1. Instead of petroleum jelly ladders described in step 1.4, sturdier wax ladders help to hold retinal slices steady during solution flow.

4.1.1. Place two small parallel cylinders of unflavored dental wax ~ 0.5 cm apart on a coverslip. On a flat surface, use a thumb to press each cylinder down and out toward the parallel edge of the coverslip. Score both flattened cylinders horizontally with a #1 coverslip (see Fig 4.1E, right side) then smear a thin layer of petroleum jelly between the wax strips with a spatula.

4.1.2. When assembling the imaging ladder in step 2.11.2, press the sliced filter paper edges into the wax scores using fine forceps (Fig 4.1G).

4.2. To set up for perfusion in step 2.13, fill syringe reservoirs with preoxygenated solutions, or use the optional gas manifold to oxygenate solutions in each reservoir. Flush all tubing with Ringer's solution, ensure all lines flow when opened and purge large bubbles.

4.3. Before filling the imaging chamber in step 2.14, use the syringe to place another dot of petroleum jelly over each exposed corner of the coverslip to prevent it from sliding laterally during flow.

4.4. When the imaging chamber is filled and mounted on the microscope stage, turn on the aspirator and connect the aspirator tubing. Test the flow of the Ringer's solution and use the micropositioner to situate the aspirator tube over the outflow chamber so that small amounts of liquid are drawn off before the chamber overflows (typically ~ 1 mm above the solution surface for a 2 mL/min flow rate). Keep Ringer's solution flowing while selecting slices in step 3.4.

4.5. To conduct the experiment in step 3.4 for perfusion, switch flow of solutions by closing the stopcock of the first solution while opening that of the second solution.

4.5.1. For instance, to deplete extracellular Na^+ from the imaging chamber, use two syringe reservoirs filled with Ringer's solution or Na^+-free solution (Table 4.3). Flow Ringer's solution to establish baseline, then switch to Na^+-free solution. This results in

large cytosolic Ca^{2+} increases in photoreceptor outer segments and cell bodies (see Fig 4.4).

4.6. For gravity-fed perfusion systems, monitor the level of solution in each reservoir so the flow rate is constant during imaging. Top off reservoirs as needed with oxygenated solutions, or maintain continuous oxygen bubbling with the gas manifold.

Representative Results

Stable positioning and transverse orientation of slices are key to successful imaging with injection or perfusion of pharmacological agents. Carefully examine and reposition slices prior to confocal imaging as needed to ensure all retinal layers are visible (Fig 4.2A, slice ii). If a slice is rotated slightly forward (Fig 4.2A, slice iii), bundles of outer segments will be visible and small adjustments can be made with forceps to bring the desired retinal layers into focus. Slices poorly adhered to the filter paper (Fig 4.2A, slice i) or retaining RPE (Fig 4.2A, slice iv) should not be used for time-lapse imaging. Example confocal images of fresh retinal slices with double and triple fluorescent labeling are presented in Figure 4.3.

Cell viability is paramount to observing physiological processes *ex vivo*; a cell viability stain such as propidium iodide (PI) is recommended to assay cell health while practicing retina slicing. Dead cells near the cut edge of all slices will accumulate PI in their nuclei (Fig 4.2B, left panels), while 5-10 µm deeper into the slice, healthy cells with normal morphology and no PI staining can be imaged. For example in photoreceptors, PI negative cells below the cut edge commonly display a stereotypical polarized, elongated morphology (Fig 4.2B, right panels). Photoreceptors remain viable in retinal slices for at least 4 h when stored in oxygenated Ringer's solution.

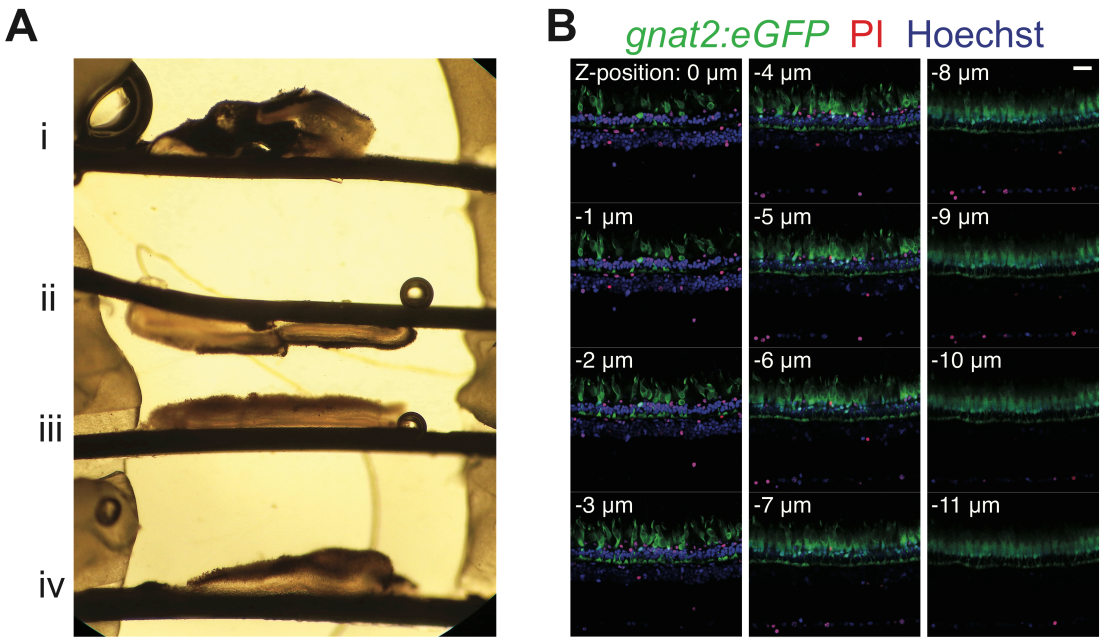

Figure 4.2. Examples of fresh zebrafish retinal slices displaying proper adhesion to the filter paper and cell viability. (A) Brightfield image of fresh retinal slices in a petroleum jelly ladder. Slices ii and iii display good adhesion and transverse retinal layers. Slices i and iv have retained substantial RPE, or are highly curved and not well-adhered to the filter paper, and should not be imaged. Scale bar = 200 µm. (B) Top-down Z montage of a fresh retinal slice from transgenic zebrafish expressing eGFP in cone photoreceptors (*(gnat2:eGFP)*, RRID:ZDB-FISH-150901-6625). Hoechst dye labels all nuclei; propidium iodide (PI) counterstaining labels nuclei of dead cells, which appear near the cut edge of the slice (left). Z-stack step size = 1 µm; scale bar = 20 µm. Fluorescent imaging conditions are outlined in Table 4.4.

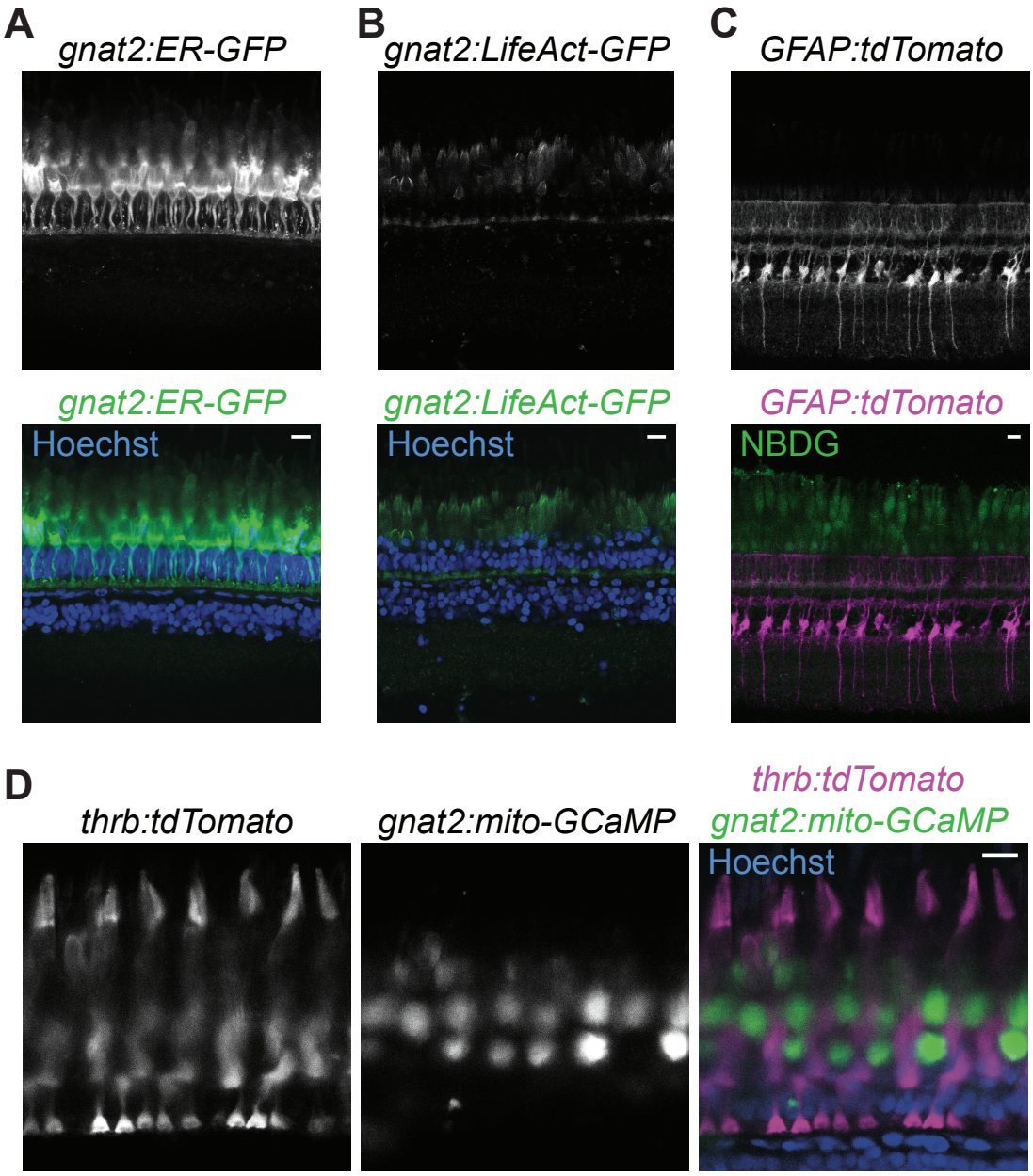

Figure 4.3. Sample confocal images of double- and triple-labeled *ex vivo* retinal slices from transgenic adult zebrafish. (A) Two-color imaging scheme employing transgenic GFP tagged endoplasmic reticulum in cones (*Tg(gnat2:calr-GFP)*, RRID:ZDB-FISH-150901-7809, top) with Hoechst nuclear counterstain (blue, bottom). (B) GFP tagged actin in cones (*Tg(gnat2:LifeAct-GFP)* (George, 2015), top) with Hoechst nuclear counterstain (blue, bottom). (C) RFP labeled Müller cells (*Tg(GFAP:tdTomato)*, RRID:ZDB-FISH-150901-17843, top) from a zebrafish fed fluorescent glucose (NBDG) demonstrating glucose uptake into cones (Giarmarco et al., 2015) (green, bottom). (D) Example of three-color imaging using double transgenic zebrafish. Left, RFP targeted to long-wavelength cone photoreceptors (*Tg(trβ2:tdTomato*) (Ma et al., 2013)). Center, calcium biosensor GCaMP targeted to cone photoreceptor mitochondria (*Tg(gnat2:mito-GCaMP3)* (Giarmarco et al., 2017)).

Right, overlaid images of tdTomato (magenta), mito-GCaMP (green), and Hoechst nuclear counterstain (blue). Images are maximum intensity Z-projections of 9 frames over a 7 µm tissue depth; scale bars represent 10 µm. Fluorescent imaging conditions are outlined in Table 4.4.

Under static conditions fluorescence of markers in retinal slices should remain stable, although photobleaching can occur during imaging. Care should be taken to minimize laser exposure during time lapses by refining parameters such as laser intensity, scan speed, and frame rate. Imaging controls are recommended for each fluorescent marker used. Controls include injecting or perfusing Ringer's solution without pharmacological agents in separate experiments, or conducting imaging experiments with non-biosensor markers that fluoresce constitutively. Figure 4.4A shows retinal slices expressing the Ca^{2+} sensor GCaMP (top) or control eGFP (bottom) in cone photoreceptors. When Na^{+} is depleted from the imaging chamber using perfusion, GCaMP reflects large increases in cytosolic Ca^{2+} for the cell body and outer segment, while eGFP fluorescence remains stable (Fig 4.4B).

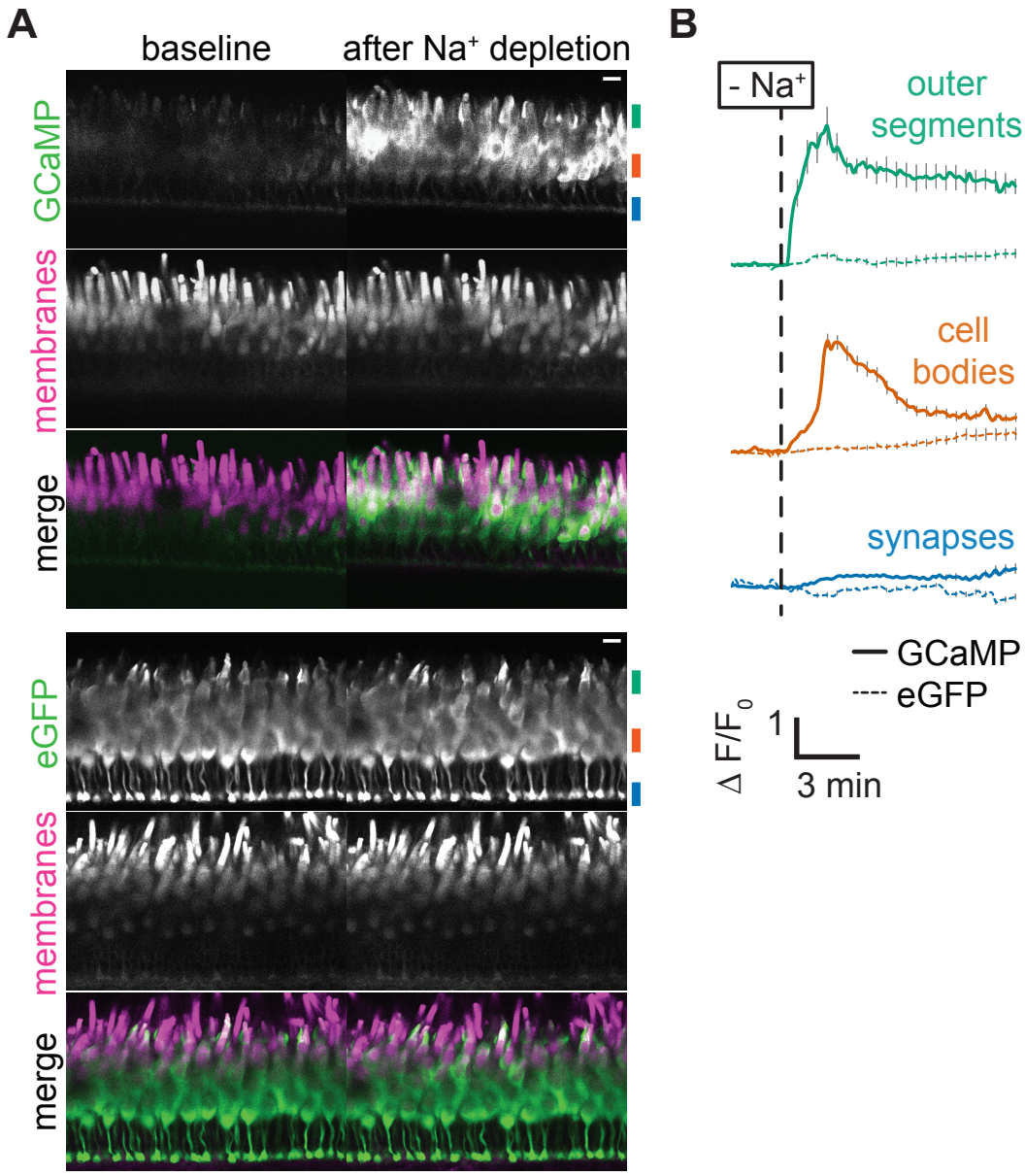

Figure 4.4. Ca^{2+} imaging with GCaMP and control eGFP. (A) Representative images of fresh retinal slices expressing the fluorescent Ca^{2+} biosensor GCaMP (*gnat2:GCaMP3*, RRID:ZDB-FISH-150901-1755, top) or eGFP (bottom) in cone photoreceptors. Left, slices at baseline; right, slices 2 min after Na^+ was isotonically depleted from the imaging chamber using perfusion of a TRIS-based Ringer's solution, which traps Ca^{2+} in photoreceptors. Scale bars = 10 µm. Fluorescent imaging conditions are outlined in Table 4.4. (B) Mean fluorescence changes of single photoreceptor compartments (outer segments, cell bodies, and synapses) during time lapse imaging of sodium depletion. Slices were imaged every 10 s, stacks were processed using ImageJ, and fluorescence of GCaMP or eGFP was normalized to signal from the membrane dye. Solid lines, GCaMP (n for outer segments = 15, cell bodies = 24, synapses = 26); dashed lines, eGFP (n for outer segments = 26, cell bodies = 20, synapses = 31). Error bars represent SE.

Discussion

Ex vivo imaging of fresh zebrafish retinal slices has proven to be a versatile tool for studying photoreceptor biology (Giarmarco et al., 2015; 2017), and is unique in that it enables analysis of single cells in a mature, fully differentiated retina. With practice it is possible to conduct multiple experiments with tissue from a single fish, even using serial slices from the same part of the retina. In addition to the challenges and suggestions regarding preparation of amphibian retinal slices for electrophysiology studies (Van Hook and Thoreson, 2013), there are important considerations for imaging experiments.

For photoreceptors, cell viability generally correlates with cell morphology, so it is important to handle the delicate retina minimally, particularly after the RPE has been removed. After slicing, use fine forceps to carefully slide slices horizontally away from the slicing chamber (Fig 4.1F) to transfer them to the ladder rather than lifting slices straight up, and always keep slices submerged in Ringer's solution. If possible, assemble the ladder of retinal slices near the confocal microscope to minimize damage to slices from shaking during transport.

Strong adhesion of retinal tissue to the filter paper is critical for creating slices that will remain stable during injection or perfusion experiments. It is necessary to carefully inspect each slice for morphology and stability just prior to imaging (Fig 4.2A); gently tapping the microscope table while viewing slice movement through the confocal ocular lens reveals stability of a particular slice. Despite precautions, drift in the Z-direction during injection or perfusion can present challenges for analysis, so it is useful to load a control dye, such as lipophilic dyes for membranes and mitochondria, to stably label an identifiable cell structure for normalization (Fig 4.4A, magenta). If slices drift > 10 μm in the Z-direction it may not be possible to extract usable single-cell data. Moderate drift in the X-Y direction can be corrected in post-processing using registration software such as MultiStackReg for ImageJ (RRID:SCR_002285).

Depending on the confocal excitation laser being used, pigments in the RPE can contribute to autofluorescence and even generate heat during imaging, so it is important

to remove most of this tissue prior to slicing. Dark-adapting animals aids in removal of the RPE while minimizing damage to the underlying retina. Inability to image the RPE is a limitation of this slice preparation, though this may be overcome by using albino animals with a transparent RPE. Another limitation is that retinal ganglion cells and end feet of Müller cells may become obscured from view by the filter paper; as an alternative preparation retinas may be flat mounted with the photoreceptor side down on the filter paper and then sliced to provide a clearer view of the innermost retina. It is also important to note that long horizontal projections of some cells, such as wide field amacrine cells, may be severed during dissection or slicing. A final limitation is that many fluorescent dyes accumulate nonspecifically in photoreceptor outer segments, so for this part of the retina it is advisable to use genetically encoded biosensors rather than indicator dyes.

Given the wide range of available fluorescent cell reporter dyes (Johnson and Rabinovitch, 2012; Uckermann et al., 2003) for tissue and genetically encoded fluorescent biosensors used successfully in zebrafish (Andrews et al., 2016; Kioka et al., 2014; Ma et al., 2013; Niethammer et al., 2009), this slice preparation could be used to study numerous biological processes in several retinal cell types (see examples in Figs 4.3, 4.4). Imaging fresh retinal slices using live cell super-resolution microscopy could also provide exciting new insights to retinal function and health on a subcellular level. Further, our preliminary work suggests this method can be adapted for *ex vivo* imaging of mouse retinal slices. While successful preparation of fresh retinal slices requires practice, it is a powerful tool that is useful for addressing a wide range of cell-specific biological questions in a mature retina.

Table of Specific Materials & Equipment

(available at: https://www.jove.com/pdf-materials/56977/jove-materials-56977-preparing-fresh-retinal-slices-from-adult-zebrafish-for-ex-vivo)

Item	Company	Catalog Number	Notes
zebrafish	Univeristy of Washington South Lake Union Aquatics Facility		stocks maintained in-house as stable transgenic lines
petroleum jelly	Fisher Scientific	19-090-843	for petroleum jelly syringe
3-mL slip tip syringe	Fisher Scientific	14-823-436	for petroleum jelly syringe
20g 3.8 cm slip tip needle	Fisher Scientific	14-826-5B	for petroleum jelly syringe
plain 7 cm X 2.5 cm microscope slide	Fisher Scientific	12-550-A3	for eyecup dissection, slicing chamber
Seche Vite clear nail polish	Amazon	B00150LT40	for slicing chamber
18 mm X 18 mm #1 glass coverslips	Fisher Scientific	12-542A	for imaging ladders
unflavored dental wax	Amazon	B01K8WNL5A	for imaging ladders
double edge razor blades	Stoelting	51427	for tissue slicing
tissue slicer with digital micrometer	Stoelting	51415	for tissue slicing
filter paper - white gridded mixed cellulose, 13 mm diameter, 0.45 μm pore size	EMD Millipore	HAWG01300	filter paper for mounting retinas
10 cm petri dish	Fisher Scientific	FB0875712	for fish euthanasia, dissection, imaging ladder assembly
15 cm plain-tipped wood applicator stick	Fisher Scientific	23-400-112	for wire eye loop tool
30g (0.25 mm diameter) tungsten wire	Fisher Scientific	AA10408G6	for wire eye loop tool
D-glucose	Sigma Aldrich	G8270	component of supplement stock solution
sodium L-lactate	Sigma Aldrich	L7022	component of supplement stock solution
sodium pyruvate	Sigma Aldrich	P2256	component of supplement stock solution
L-glutamine	Sigma Aldrich	G3126	component of supplement stock solution
L-glutathione, reduced	Sigma Aldrich	G4251	component of supplement stock solution
L-ascorbic acid	Sigma Aldrich	A5960	component of supplement stock solution
NaCl	Sigma Aldrich	S7653	component of Ringer's solution
KCl	Sigma Aldrich	P9333	component of Ringer's solution
$CaCl_2 \cdot 2H_2O$	Sigma Aldrich	C3881	component of Ringer's solution
NaH_2PO_4	Sigma Aldrich	S8282	component of Ringer's solution
$MgCl_2 \cdot 6H_2O$	Sigma Aldrich	M0250	component of Ringer's solution
HEPES	Sigma Aldrich	H3375	component of Ringer's solution
Tris base	Fisher Scientific	BP152	component of Na^+-free Ringer's solution
6 N HCl	Fisher Scientific	02-003-063	component of Na^+-free Ringer's solution
KH_2PO_4	Sigma Aldrich	P5655	component of Na^+-free Ringer's solution
50 mL conical centrifuge tube	Denville Scientific	C1062-P	container for Ringer's solution
Vannas scissors - 8 cm, angled 5 mm blades	World Precision Instruments	501790	micro-scissors for eyecup dissection
Swiss tweezers - #5, 11 cm, straight, 0.06 X 0.07 mm tips	World Precision Instruments	504510	fine forceps for eyecup dissection and slice manipulation
single edge razor blades	Fisher Scientific	12-640	for eyecup dissection and trimming filter paper
EMD Millipore filter forceps	Fisher Scientific	XX6200006P	flat forceps for handling wet filter paper
C^{12} 558/568 BODIPY™	Fisher Scientific	D3835	stains live cell nuclei; incubate 5 µg/mL for 15 min at room temperature
propidium iodide (PI)	Fisher Scientific	P3566	stains dead cell nuclei; incubate 5 µg/mL for 20 min at room temperature
Hoechst 33342	Fisher Scientific	62249	stains live cell nuclei; incubate 5 µg/mL for 20 min at room temperature
Tetramethylrhodamine, methyl ester (TMRM)	Fisher Scientific	T668	stains functional, negatively-charged mitochondria; incubate 1 nM for 30 min at room temperature
tissue perfusion chamber	Cell MicroControls	BT-1-18/BT-1-18BV [-SY]	imaging chamber for injection or perfusion
2-(N-(7-Nitrobenz-2-oxa-1,3-diazol-4-yl)Amino)-2-Deoxyglucose (NBDG)	Fisher Scientific	N13195	fluorescent glucose analog adminitered orally to zebrafish 30 min prior to euthanasia
Olympus laser scanning confocal microscope	Olympus	FV1000	confocal microscope for visualizing fluorescence of slices at single-cell resolution
Carbonyl cyanide 3-chlorophenylhydrazone (CCCP)	Sigma Aldrich	C2759	experimental reagent which ablates mitochondrial respiration; treat slices to a final concentration of 1 µM
miniature aspirator positioner	Cell MicroControls	FL-1	for perfusion
perfusion manifold, gas bubbler manifold, flow valve, 60cc syringe holder	Warner Instruments	various	for perfusion

Table 4.1 – Recipe for Supplement Solution

Supplement Solution		
	50X stock* concentration (mM)	working concentration (mM)
D-glucose	500	10
sodium lactate	50	1
sodium pyruvate	25	0.5
L-glutamine	25	0.5
reduced glutathione	25	0.5
ascorbic acid	15	0.3

* store aliquots at -20ºC < 6 months; add fresh to Ringer's solution

Table 4.2 – Recipe for Standard Ringer's Solution

Ringer's Solution	
	concentration (mM)
NaCl	133
KCl	2.5
$CaCl_2 \cdot 2H_2O$	2
NaH_2PO_4	1.5
$MgCl_2 \cdot 6H_2O$	1.5
HEPES	10

pH to 7.4 using NaOH

store at 4°C in sterile bottle < 1 month

Table 4.3 – Recipe for Na^+-free Ringer's Solution

Na^+-Free Ringer's Solution	
	concentration (mM)
TRIS	147
HCl	120
KCl	1
$CaCl_2 \cdot 2H_2O$	2
KH_2PO_4	1.5
$MgCl_2 \cdot 6H_2O$	1.5
HEPES	10

pH to 7.4 using HCl

store at 4°C in sterile bottle < 1 month

Table 4.4 – Example Confocal Imaging Settings for Retinal Slices (Olympus FluoView)

Confocal Imaging Settings			
Fluorophore	Excitation		Emission Filter
	Wavelength	Laser Intensity	
GFP (including GCaMP)	488 nm	2 - 5%	eGFP or AlexaFluor 488
tdTomato	559 nm	5%	AlexaFluor 594
PI	559 nm	2%	PI
Hoechst 33342	405 nm	1%	DAPI
NBDG	488 nm	10%	eGFP or AlexaFluor 488
C^{12} 558/568 BODIPY™	559 nm	1%	AlexaFluor 594
TMRM	559 nm	3%	RFP

Acknowledgments

The work described in this chapter was published in the Journal of Visualized Experiments. The other authors that contributed to this study were Whitney M. Cleghorn, James B. Hurley, and Susan E. Brockerhoff. We thank Ralph Nelson and Daniel Possin for thoughtful guidance while developing this protocol, and Eva Ma, Ashley George and Gail Stanton for generation of stable transgenic zebrafish lines. The work was supported by NSF GRFP 2013158531 to M.G., NIH NEI 5T32EY007031 to W.C. and M.G., and EY026020 to J.H. and S.B.

Together, these studies using zebrafish and mice provide important clues into the unique metabolic programs and mitochondrial functions of RPE cells and photoreceptors. RPE cell mitochondria are adapted to use a variety of fuels, including lactate released from photoreceptors. Glucose is the primary fuel for photoreceptors, which generate that lactate using a different metabolic scheme. The localization and Ca^{2+} uptake capacity of photoreceptor mitochondria task them with more than metabolism: they also maintain distinct Ca^{2+} signaling compartments within the cell. Breakdown of these mitochondrial specializations could affect the metabolic relationships between the RPE and photoreceptors, and contribute to retinal disease.

Chapter 5

Conclusions and Future Directions

RPE and photoreceptor cells use distinct and complementary metabolic schemes

Previous studies have suggested that excess lactate made by photoreceptors can translocate through RPE cells and into the choriocapillaris (Adler and Southwick, 1992; Alm and Törnquist, 1985; Philp et al., 1998). We have provided the first direct evidence that RPE cells can intercept some of that lactate and convert it into pyruvate to fuel mitochondrial respiration. This can diminish the amount of glucose that is oxidized by RPE cells, so that more glucose can be exported toward the retina. Breakdown of this hypothesized "metabolic ecosystem" (see Figure 2.10) may contribute to some forms of retinal degeneration.

To test this hypothesis, we used a variety of techniques including the retinal slice preparation described in Chapter 4 to show that photoreceptors specifically are able to take up glucose *in vivo* (Figures 2.1, 2.2). Retinas convert glucose primarily to lactate, while RPE cells oxidize glucose to fuel mitochondrial respiration (Figures 2.3, 2.4). RPE cells can also use lactate to fuel mitochondrial respiration (Figures 2.5, 2.6), and this can suppress consumption of glucose by glycolysis (Figures 2.7, 2.8). Lastly, we showed that exogenous lactate can enhance glucose transport across RPE cells (Figure 2.9).

Metabolic specialization in retinal and RPE cells may be crucially linked to biological functions. It has been suggested that aerobic glycolysis in photoreceptors can support synthesis of molecules needed for new OS disks (Chinchore et al., 2017). Actively respiring mitochondria in RPE cells are poised to generate ATP from lactate (Kanow et al., 2017), amino acids (Chao et al., 2017), or fatty acids (Reyes-Reveles et al., 2017). Future studies should address what mitochondrial adaptations confer these metabolic

specializations, and what capacity the RPE has to store unused glucose. These avenues could provide the basis of broad therapies for retinal degenerative diseases.

Cone mitochondria do more than just make ATP

Photoreceptors and RPE cells use their mitochondria differently, and it has been proposed that another role of photoreceptor mitochondria could be to buffer cytosolic Ca^{2+} (Ma et al., 2013; Szikra and Krizaj, 2007). The capacity for free Ca^{2+} uptake into cone mitochondria has been estimated to be several hundred nanomolar (Szikra and Krizaj, 2007). Other tissues store large amounts of Ca^{2+} in mitochondria as inorganic phosphate salts (Greenawalt et al., 1964). Cone photoreceptor mitochondria are spatially poised to buffer high Ca^{2+} from the OS, forming a dense cluster at its base (Figure 3.3) (Cohen, 1961; Dowling, 1965; Nag and Wadhwa, 2016; Perkins et al., 2003; Tarboush et al., 2012). We provided evidence that cone mitochondria take up Ca^{2+} with the MCU, and that this separates IS and OS Ca^{2+} pools.

Using the retinal slice preparation described in Chapter 4 with transgenic zebrafish expressing a fluorescent Ca^{2+} sensor in cones (Figures 3.1, 3.2), we performed imaging experiments to modulate $[Ca^{2+}]_i$ and Ca^{2+} uptake into mitochondria. Pharmacological manipulations can raise $[Ca^{2+}]_i$ in either the IS (Figure 3.4) or OS (Figures 3.5, 3.6), but the change in $[Ca^{2+}]_i$ is confined to the compartment in which it is initiated. When Ca^{2+} uptake into mitochondria is blocked with the MCU inhibitor Ru360, Ca^{2+} redistributes throughout the cell and into other compartments. This suggests that changes in $[Ca^{2+}]_i$ in cones are mediated by mitochondria via MCU.

Ca^{2+} uptake into mitochondria of many cell types can have diverse effects, stimulating processes from metabolism (Wan et al., 1989) to cell death (Orrenius et al., 2003). Cone mitochondria appear to have a particularly large capacity for Ca^{2+} uptake compared to rods (Szikra and Krizaj, 2007), but in other cells $[Ca^{2+}]_i$ must be in the micromolar range to activate MCU (Williams et al., 2013). While MCU activation and regulation in cones is not understood, in our study large MCU-dependent increases in free $[Ca^{2+}]_m$ were seen only when cytosolic $[Ca^{2+}]_i$ was at a maximum (Table 3.1, Figure

3.6D-F). Future studies should address the regulation of MCU in photoreceptors, the possible existence of Ca^{2+} microdomains at ER-mitochondrial contact sites, and the capacity of photoreceptor mitochondria to store and release Ca^{2+}.

Retinal slices are useful for studying cell-specific processes

The complicated structure and large number of cell types in the retina present major challenges for studying a subset of cells like photoreceptors. Traditional biochemical methods to analyze metabolic function, protein content, or gene expression utilize the entire retina, making it difficult to determine the contributions of a particular cell type. Useful imaging approaches such as immunostaining (Gospe et al., 2010; Morgan et al., 2006) and enzyme histochemistry (Andrews et al., 1999; Lowry et al., 1961; Matschinsky et al., 1968) provide a transverse view of retinal layers and can incorporate cell-specific markers, but cannot report activities in live cells.

Fresh retinal slices are a tool for both imaging (Kulkarni et al., 2015) and electrophysiological (Connaughton, 2003; Van Hook and Thoreson, 2013) studies, and an expanding palette of genetically encoded sensors are emerging to detect Ca^{2+} (Akerboom et al., 2013) and other important molecules (Andrews et al., 2016; Díaz-García et al., 2017; Kioka et al., 2014; Niethammer et al., 2009) in live cells. Zebrafish, amenable to transgenesis and with a retina dominated by cones, are ideal for conducting slice prep experiments to understand biological functions in live cones. We developed and published a detailed protocol (see Chapter 4) for generating fresh retinal slices from adult zebrafish specifically for *ex vivo* imaging. This slice preparation was used in Chapter 2 to demonstrate glucose uptake into photoreceptors of both mice and zebrafish *in vivo*, and in Chapter 3 to explore Ca^{2+} dynamics in cone cytosol and mitochondria *ex vivo*. With a range of cell-specific promoters and fluorescent sensors available for use in the retina, this method is broadly adaptable for extracting single-cell information from a complicated living tissue.

Does Ca^{2+} sequestration by cone mitochondria affect phototransduction or the progression of retinal disease?

The finding that cone mitochondria can buffer Ca^{2+} from the OS indicates that mitochondria could play some role in phototransduction, which involves large and rapid changes in $[Ca^{2+}]_i$. Curiously, eliminating the only known OS Ca^{2+} efflux route in rods (Vinberg et al., 2015) or cones (Sakurai et al., 2016) by NCKX knockout did not result in severe retinal degeneration, and animals showed a small degree of phototransduction recovery, indicating that Ca^{2+} can still slowly leave the OS. These findings, together with the results in Chapter 3, suggest that mitochondria could be taking up that Ca^{2+}.

Future electrophysiological studies will elucidate the potential role of MCU in the visual response, using isolated retinas (Vinberg et al., 2014) treated with Ru360, or using MCU knockout (Pan et al., 2013) and overexpressing (Hutto et al., 2018) animals. The MCU complex includes several regulatory subunits which fine-tune its affinity for Ca^{2+} (Kamer and Mootha, 2015; Tomar et al., 2016), and expression of these regulators varies widely across tissues to match cellular function (De Stefani et al., 2011; Paillard et al., 2017). Determining how MCU is regulated in the retina and photoreceptors will shed light on how, when, and where mitochondrial Ca^{2+} uptake happens.

Mitochondrial Ca^{2+} uptake may also affect retinal disease progression, as high $[Ca^{2+}]_m$ induces apoptosis in most cells (Orrenius et al., 2003) including other zebrafish sensory neurons (Esterberg et al., 2016). Canonical apoptosis has been implicated in retinal degeneration resulting from light damage (Hafezi et al., 1997) or diabetes (Barber et al., 1998), but in many retinal degeneration models the typical hallmarks of apoptosis are absent (Arango-Gonzalez et al., 2014). In a phototransduction mutant zebrafish model of retinitis pigmentosa, cytosolic Ca^{2+} spikes in cones were surprisingly reduced compared to wild-type cones (Ma et al., 2013), a phenomenon that could be explained by enhanced Ca^{2+} uptake into mitochondria. Future studies using MCU overexpressing and knockout animals will explore what happens when cone mitochondria become overloaded with Ca^{2+}, and how mitochondrial Ca^{2+} uptake affects progression of retinal disease.

How do Ca^{2+}, light, and time of day influence mitochondrial metabolism in the retina and RPE?

Responding to fluctuations in light level and subsequently $[Ca^{2+}]_i$ is the most unique and important function of photoreceptors. Additionally photoreceptors undergo daily circadian cycles of gene expression regardless of light exposure (Cahill and Besharse, 1995). In other cells, important functions like mitochondrial biogenesis and respiration (Schmitt et al., 2018) fluctuate on a 24-hour circadian cycle. Photoreceptors consume more ATP in darkness (Okawa et al., 2008), when mitochondrial respiration is most active in the retina (Du et al., 2016a; Perkins et al., 2003). The types of mitochondrial adaptations facilitating this switch, and their regulation by light, Ca^{2+} or the circadian clock are not understood.

Preliminary studies in zebrafish cones using serial block-face SEM have revealed that mitochondria may increase in number in darkness (Sloat et al., 2016). In addition to Ca^{2+}-stimulated flux through the TCA cycle (Wan et al., 1989), mitochondria of other cells can rearrange their cristae (Perkins et al., 2010) or form hyperfused networks (Glancy et al., 2015) to meet ATP demands. In cones of some species, light is filtered and guided to the OS using oil droplets (Toomey and Corbo, 2017) or specialized organelles (MacNichol et al., 1978) derived from mitochondria; mitochondrial adaptations occurring during a circadian cycle may have effects apart from metabolism (Hoang et al., 2002). Future studies should address mitochondrial biogenesis, cristae organization, and respiration in photoreceptors throughout the day. Phototransduction-deficient animals (Kennedy et al., 2007) and retinal slice experiments with genetically-encoded sensors for ATP (Tsuyama et al., 2013) or NADH (Zhao and Yang, 2015) could help to parse the metabolic effects from phototransduction or Ca^{2+}, respectively.

The metabolic relationship between cells of the retina and RPE may also change throughout the day. OS disks are shed and phagocytosed by RPE cells on a 24-hour cycle, regardless of light exposure (LaVail, 1976), necessitating anabolism in photoreceptors and fatty acid oxidation by RPE cells. How this metabolic shift occurs and how it affects glucose flow into the retina is an open question. As cones are

thought to be more dependent on glucose (Aït-Ali et al., 2015; Nihira et al., 1995) and mitochondrial respiration (Perkins et al., 2004), it is also possible that rods and cones employ different metabolic programs throughout the day.

.

References

Ablonczy, Z., Dahrouj, M., Tang, P.H., Liu, Y., Sambamurti, K., Marmorstein, A.D., and Crosson, C.E. (2011). Human retinal pigment epithelium cells as functional models for the RPE *in vivo*. Invest. Ophthalmol. Vis. Sci. *52*, 8614–8620.

Adijanto, J., and Philp, N.J. (2014). Cultured primary human fetal retinal pigment epithelium (hfRPE) as a model for evaluating RPE metabolism. Exp. Eye Res. *126*, 77–84.

Adler, A.J., and Southwick, R.E. (1992). Distribution of glucose and lactate in the interphotoreceptor matrix. Ophthalmic Res. *24*, 243–252.

Aït-Ali, N., Fridlich, R., Millet-Puel, G., Clérin, E., Delalande, F., Jaillard, C., Blond, F., Perrocheau, L., Reichman, S., Byrne, L.C., et al. (2015). Rod-derived cone viability factor promotes cone survival by stimulating aerobic glycolysis. Cell *161*, 817–832.

Akerboom, J., Carreras Calderón, N., Tian, L., Wabnig, S., Prigge, M., Tolö, J., Gordus, A., Orger, M.B., Severi, K.E., Macklin, J.J., et al. (2013). Genetically encoded calcium indicators for multi-color neural activity imaging and combination with optogenetics. Front Mol Neurosci *6*, 2.

Akimoto, M., Cheng, H., Zhu, D., Brzezinski, J.A., Khanna, R., Filippova, E., Oh, E.C.T., Jing, Y., Linares, J.-L., Brooks, M., et al. (2006). Targeting of GFP to newborn rods by Nrl promoter and temporal expression profiling of flow-sorted photoreceptors. Proc Natl Acad Sci USA *103*, 3890–3895.

Alm, A., and Törnquist, P. (1985). Lactate transport through the blood-retinal and the blood-brain barrier in rats. Ophthalmic Res. *17*, 181–184.

Ames, A., Li, Y.Y., Heher, E.C., and Kimble, C.R. (1992). Energy metabolism of rabbit retina as related to function: high cost of Na+ transport. J. Neurosci. *12*, 840–853.

Andrews, N., Ramel, M.-C., Kumar, S., Alexandrov, Y., Kelly, D.J., Warren, S.C., Kerry, L., Lockwood, N., Frolov, A., Frankel, P., et al. (2016). Visualising apoptosis in live zebrafish using fluorescence lifetime imaging with optical projection tomography to map FRET biosensor activity in space and time. J. Biophoton *9*, 414–424.

Andrews, R.M., Griffiths, P.G., Johnson, M.A., and Turnbull, D.M. (1999). Histochemical localisation of mitochondrial enzyme activity in human optic nerve and retina. British Journal of Ophthalmology *83*, 231–235.

Antinucci, P., and Hindges, R. (2016). A crystal-clear zebrafish for in vivo imaging. Sci Rep *6*, 29490.

Arango-Gonzalez, B., Trifunović, D., Sahaboglu, A., Kranz, K., Michalakis, S., Pietro Farinelli, Koch, S., Koch, F., Cottet, S., Janssen-Bienhold, U., et al. (2014). Identification of a Common Non-Apoptotic Cell Death Mechanism in Hereditary Retinal Degeneration. PLoS ONE *9*, e112142.

Augustine, G.J., Santamaria, F., and Tanaka, K. (2003). Local calcium signaling in neurons. Neuron *40*, 331–346.

Badr, G.A., Tang, J., Ismail-Beigi, F., and Kern, T.S. (2000). Diabetes downregulates GLUT1 expression in the retina and its microvessels but not in the cerebral cortex or its microvessels. Diabetes *49*, 1016–1021.

Barber, A.J., Lieth, E., Khin, S.A., Antonetti, D.A., Buchanan, A.G., and Gardner, T.W. (1998). Neural apoptosis in the retina during experimental and human diabetes. Early onset and effect of insulin. J. Clin. Invest. *102*, 783–791.

Baughman, J.M., Perocchi, F., Girgis, H.S., Plovanich, M., Belcher-Timme, C.A., Sancak, Y., Bao, X.R., Strittmatter, L., Goldberger, O., Bogorad, R.L., et al. (2011). Integrative genomics identifies MCU as an essential component of the mitochondrial calcium uniporter. Nature *476*, 341–345.

Beckers, C.J., and Balch, W.E. (1989). Calcium and GTP: essential components in vesicular trafficking between the endoplasmic reticulum and Golgi apparatus. J. Cell Biol. *108*, 1245–1256.

Blenkinsop, T.A., Saini, J.S., Maminishkis, A., Bharti, K., Wan, Q., Banzon, T., Lotfi, M., Davis, J., Singh, D., Rizzolo, L.J., et al. (2015). Human adult retinal pigment epithelial stem cell-derived RPE monolayers exhibit key physiological characteristics of native tissue. Invest. Ophthalmol. Vis. Sci. *56*, 7085–7099.

Booth, C., and Koch, G.L. (1989). Perturbation of cellular calcium induces secretion of luminal ER proteins. Cell *59*, 729–737.

Bramall, A.N., Wright, A.F., Jacobson, S.G., and McInnes, R.R. (2010). The genomic, biochemical, and cellular responses of the retina in inherited photoreceptor degenerations and prospects for the treatment of these disorders. Annu. Rev. Neurosci. *33*, 441–472.

Brockerhoff, S.E., Dowling, J.E., and Hurley, J.B. (1998). Zebrafish retinal mutants. Vision Res. *38*, 1335–1339.

Burgess, E.A., and Sylven, B. (1962). Glucose, lactate, and lactic dehydrogenase activity in normal interstitial fluid and that of solid mouse tumors. Cancer Res. *22*, 581–588.

Burnside, B., Wang, E., Pagh-Roehl, K., and Rey, H. (1993). Retinomotor movements in isolated teleost retinal cone inner-outer segment preparations (CIS-COS): effects of light, dark and dopamine. Exp. Eye Res. *57*, 709–722.

Cahill, G.M., and Besharse, J.C. (1995). Circadian Rhythmicity in Vertebrate Retinas: Regulation by a Photoreceptor Oscillator. Progress in Retinal and Eye Research *14*, 267–291.

Casson, R.J., Wood, J.P.M., Han, G., Kittipassorn, T., Peet, D.J., and Chidlow, G. (2016). M-type pyruvate kinase isoforms and lactate dehydrogenase A in the mammalian retina: Metabolic implications. Invest. Ophthalmol. Vis. Sci. *57*, 66–80.

Chang, B., Hawes, N.L., Hurd, R.E., Davisson, M.T., Nusinowitz, S., and Heckenlively, J.R. (2002). Retinal degeneration mutants in the mouse. Vision Res. *42*, 517–525.

Chao, J.R., Knight, K., Engel, A.L., Jankowski, C., Wang, Y., Manson, M.A., Gu, H., Djukovic, D., Raftery, D., Hurley, J.B., et al. (2017). Human retinal pigment epithelial cells prefer proline as a nutrient and transport metabolic intermediates to the retinal side. J. Biol. Chem. *292*, 12895–12905.

Chen, M., Van Hook, M.J., and Thoreson, W.B. (2015). Ca^{2+} diffusion through endoplasmic reticulum supports elevated intraterminal Ca^{2+} levels needed to sustain synaptic release from rods in darkness. J. Neurosci. *35*, 11364–11373.

Chinchore, Y., Begaj, T., Wu, D., Drokhlyansky, E., and Cepko, C.L. (2017). Glycolytic reliance promotes anabolism in photoreceptors. eLife *6*.

Cohen, A.I. (1961). The fine structure of the extrafoveal receptors of the Rhesus monkey. Exp. Eye Res. *1*, 128–136.

Collymore, C., Rasmussen, S., and Tolwani, R.J. (2013). Gavaging adult zebrafish. JoVE e50691.

Connaughton, V.P. (2003). Zebrafish retinal slice preparation. Methods Cell Sci *25*, 49–58.

Contreras, L., Drago, I., Zampese, E., and Pozzan, T. (2010). Mitochondria: the calcium connection. Biochim. Biophys. Acta *1797*, 607–618.

Contreras, L., Gomez-Puertas, P., Iijima, M., Kobayashi, K., Saheki, T., and Satrústegui, J. (2007). Ca^{2+} Activation Kinetics of the Two Aspartate-Glutamate Mitochondrial Carriers, Aralar and Citrin. J. Biol. Chem. *282*, 7098–7106.

Csordás, G., Várnai, P., Golenár, T., Roy, S., Purkins, G., Schneider, T.G., Balla, T., and Hajnóczky, G. (2010). Imaging Interorganelle Contacts and Local Calcium Dynamics at the ER-Mitochondrial Interface. Molcel *39*, 121–132.

De Stefani, D., Raffaello, A., Teardo, E., Szabò, I., and Rizzuto, R. (2011). A forty-kilodalton protein of the inner membrane is the mitochondrial calcium uniporter. Nature *476*, 336–340.

Dizhoor, A.M. (2000). Regulation of cGMP synthesis in photoreceptors: role in signal

transduction and congenital diseases of the retina. Cell. Signal. *12*, 711–719.

Díaz-García, C.M., Mongeon, R., Lahmann, C., Koveal, D., Zucker, H., and Yellen, G. (2017). Neuronal Stimulation Triggers Neuronal Glycolysis and Not Lactate Uptake. Cell Metabolism *26*, 361–374.e364.

Dowling, J.E. (1965). Foveal receptors of the monkey retina: fine structure. Science *147*, 57–59.

Dowling, J.E. (1987). The retina: an approachable part of the brain (Cambridge: Harvard University Press).

Dowling, J.E., and Boycott, B.B. (1966). Organization of the primate retina: electron microscopy. Proc. R. Soc. Lond., B, Biol. Sci. *166*, 80–111.

Du, J., Cleghorn, W.M., Contreras, L., Lindsay, K., Rountree, A.M., Chertov, A.O., Turner, S.J., Sahaboglu, A., Linton, J., Sadilek, M., et al. (2013a). Inhibition of mitochondrial pyruvate transport by zaprinast causes massive accumulation of aspartate at the expense of glutamate in the retina. J. Biol. Chem. *288*, 36129–36140.

Du, J., Cleghorn, W., Contreras, L., Linton, J.D., Chan, G.C.-K., Chertov, A.O., Saheki, T., Govindaraju, V., Sadilek, M., and Satrústegui, J. (2013b). Cytosolic reducing power preserves glutamate in retina. Proc. Natl. Acad. Sci. U.S.A. *110*, 18501–18506.

Du, J., Linton, J.D., and Hurley, J.B. (2015). Probing metabolism in the intact retina using stable isotope tracers. Meth. Enzymol. *561*, 149–170.

Du, J., Rountree, A., Cleghorn, W.M., Contreras, L., Lindsay, K.J., Sadilek, M., Gu, H., Djukovic, D., Raftery, D., Satrústegui, J., et al. (2016a). Phototransduction influences metabolic flux and nucleotide metabolism in mouse retina. J. Biol. Chem. *291*, 4698–4710.

Du, J., Yanagida, A., Knight, K., Engel, A.L., Vo, A.H., Jankowski, C., Sadilek, M., Tran, V.T.B., Manson, M.A., Ramakrishnan, A., et al. (2016b). Reductive carboxylation is a major metabolic pathway in the retinal pigment epithelium. Proc. Natl. Acad. Sci. U.S.A. *113*, 14710–14715.

Ennis, S.R., Johnson, J.E., and Pautler, E.L. (1982). In situ kinetics of glucose transport across the blood-retinal barrier in normal rats and rats with streptozocin-induced diabetes. Invest. Ophthalmol. Vis. Sci. *23*, 447–456.

Esterberg, R., Hailey, D.W., Rubel, E.W., and Raible, D.W. (2014). ER-mitochondrial calcium flow underlies vulnerability of mechanosensory hair cells to damage. J. Neurosci. *34*, 9703–9719.

Esterberg, R., Linbo, T., Pickett, S.B., Wu, P., Ou, H.C., Rubel, E.W., and Raible, D.W. (2016). Mitochondrial calcium uptake underlies ROS generation during aminoglycoside-induced hair cell death. J. Clin. Invest. *126*, 3556–3566.

Fadool, J.M. (2003). Development of a rod photoreceptor mosaic revealed in transgenic zebrafish. Developmental Biology *258*, 277–290.

Ferrington, D.A., Kapphahn, R.J., Leary, M.M., Atilano, S.R., Terluk, M.R., Karunadharma, P., Chen, G.K.-J., Ratnapriya, R., Swaroop, A., Montezuma, S.R., et al. (2016). Experimental Eye Research. Exp. Eye Res. *145*, 269–277.

Fox, J. (2005). Getting started with the R commander: a basic-statistics graphical user interface to R. Journal of Statistical Software *14*.

Geiger, T., Velic, A., Macek, B., Lundberg, E., Kampf, C., Nagaraj, N., M, U., Cox, J., and Mann, M. (2013). Initial quantitative proteomic map of 28 mouse tissues using the SILAC mouse. Mol Cell Proteomics *12*, 1709–1722.

George, A.A. (2015). Synaptojanin1 is involved in endolysosomal trafficking in cone photoreceptors (Doctoral dissertation). *Retrieved from http://hdl.handle.net/1773/33102*.

George, A.A., Hayden, S., Holzhausen, L.C., Ma, E.Y., Suzuki, S.C., and Brockerhoff, S.E. (2014). Synaptojanin 1 is required for endolysosomal trafficking of synaptic proteins in cone photoreceptor inner segments. PLoS ONE *9*, e84394.

Giarmarco, M.M., Cleghorn, W.M., Hurley, J.B., and Brockerhoff, S.E. (2018). Preparing Fresh Retinal Slices from Adult Zebrafish for *Ex Vivo* Imaging Experiments. JoVE.

Giarmarco, M.M., Cleghorn, W.M., Sloat, S.R., Hurley, J.B., and Brockerhoff, S.E. (2017). Mitochondria Maintain Distinct Ca^{2+} Pools in Cone Photoreceptors. J. Neurosci. *37*, 2061–2072.

Giarmarco, M.M., Lindsay, K.J., Du, J., Cleghorn, W.M., Brockerhoff, S.E., and Hurley, J.B. (2015). Imaging Real-time Glucose Uptake in Retina Reveals Distinct Transport Among Cell Types. Invest. Ophthalmol. Vis. Sci. *56*.

Glancy, B., and Balaban, R.S. (2012). Role of mitochondrial Ca^{2+} in the regulation of cellular energetics. Biochemistry *51*, 2959–2973.

Glancy, B., Hartnell, L.M., Malide, D., Yu, Z.-X., Combs, C.A., Connelly, P.S., Subramaniam, S., and Balaban, R.S. (2015). Mitochondrial reticulum for cellular energy distribution in muscle. Nature *523*, 617–620.

Gorczyca, W.A., Polans, A.S., Surgucheva, I.G., Subbaraya, I., Baehr, W., and Palczewski, K. (1995). Guanylyl Cyclase Activating Protein: A calcium-sensitive regulator of phototransduction. J. Biol. Chem. *270*, 22029–22036.

Gospe, S.M., Baker, S.A., and Arshavsky, V.Y. (2010). Facilitative glucose transporter Glut1 is actively excluded from rod outer segments. Journal of Cell Science *123*, 3639–3644.

Greenawalt, J.W., Rossi, C.S., and Lehninger, A.L. (1964). Effect of active accumulation

of calcium and phosphate ions on the structure of rat liver mitochondria. J. Cell Biol. *23*, 21–38.

Gross, J.M., and Perkins, B.D. (2007). Zebrafish mutants as models for congenital ocular disorders in humans. Mol. Reprod. Dev. *75*, 547–555.

Gunter, T.E., and Gunter, K.K. (2001). Uptake of calcium by mitochondria: transport and possible function. IUBMB Life *52*, 197–204.

Hafezi, F., Marti, A., Munz, K., and Remé, C.E. (1997). Light-induced apoptosis: differential timing in the retina and pigment epithelium. Exp. Eye Res. *64*, 963–970.

Hamasaki, M., Furuta, N., Matsuda, A., Nezu, A., Yamamoto, A., Fujita, N., Oomori, H., Noda, T., Haraguchi, T., Hiraoka, Y., et al. (2013). Autophagosomes form at ER–mitochondria contact sites. Nature *495*, 389–393.

Hanein, S., Perrault, I., Gerber, S., Tanguy, G., Barbet, F., Ducroq, D., Calvas, P., Dollfus, H., Hamel, C., Lopponen, T., et al. (2004). Leber congenital amaurosis: Comprehensive survey of the genetic heterogeneity, refinement of the clinical definition, and genotype-phenotype correlations as a strategy for molecular diagnosis. Hum. Mutat. *23*, 306–317.

Heidelberger, R., Thoreson, W.B., and Witkovsky, P. (2005). Synaptic transmission at retinal ribbon synapses. Progress in Retinal and Eye Research *24*, 682–720.

Hoang, Q.V., Linsenmeier, R.A., Chung, C.K., and Curcio, C.A. (2002). Photoreceptor inner segments in monkey and human retina: mitochondrial density, optics, and regional variation. Vis. Neurosci. *19*, 395–407.

Hung, Y.P., Albeck, J.G., Tantama, M., and Yellen, G. (2011). Imaging cytosolic NADH-NAD^+ redox state with a genetically encoded fluorescent biosensor. Cell Metabolism *14*, 545–554.

Hurley, J.B., Lindsay, K.J., and Du, J. (2015). Glucose, lactate, and shuttling of metabolites in vertebrate retinas. J. Neurosci. Res. *93*, 1079–1092.

Hutto, R., Bisbach, C.M., Hurley, J.B., and Brockerhoff, S.E. (2018). Overexpression of the mitochondrial Ca^{2+} uniporter in cones alters Ca^{2+} and mitochondrial homeostasis. Invest. Ophthalmol. Vis. Sci. *(in press)*.

Iwamoto, T., Watano, T., and Shigekawa, M. (1996). A novel isothiourea derivative selectively inhibits the reverse mode of Na^+/Ca^{2+} exchange in cells expressing NCX1. J. Biol. Chem. *271*, 22391–22397.

Johnson, J.E., Jr, Perkins, G.A., Giddabasappa, A., Chaney, S., Xiao, W., White, A.D., Brown, J.M., Waggoner, J., Ellisman, M.H., and Fox, D.A. (2007). Spatiotemporal regulation of ATP and Ca^{2+} dynamics in vertebrate rod and cone ribbon synapses. Molecular Vision *13*, 887.

Johnson, L.V., Forest, D.L., Banna, C.D., Radeke, C.M., Maloney, M.A., Hu, J., Spencer, C.N., Walker, A.M., Tsie, M.S., Bok, D., et al. (2011). Cell culture model that mimics drusen formation and triggers complement activation associated with age-related macular degeneration. Proc. Natl. Acad. Sci. U.S.A. *108*, 18277–18282.

Johnson, S., and Rabinovitch, P. (2012). *Ex vivo* imaging of excised tissue using vital dyes and confocal microscopy. Curr Protoc Cytom *Chapter 9*, Unit9.39.

Jouaville, L.S., Pinton, P., Bastianutto, C., Rutter, G.A., and Rizzuto, R. (1999). Regulation of mitochondrial ATP synthesis by calcium: Evidence for a long-term metabolic priming. Proc. Natl. Acad. Sci. U.S.A. *96*, 13807–13812.

Joyal, J.-S., Sun, Y., Gantner, M.L., Shao, Z., Evans, L.P., Saba, N., Fredrick, T., Burnim, S., Kim, J.S., Patel, G., et al. (2016). Retinal lipid and glucose metabolism dictates angiogenesis through the lipid sensor Ffar1. Nat. Med. *22*, 439–445.

Jung, S.-R., Reed, B.J., and Sweet, I.R. (2009). A highly energetic process couples calcium influx through L-type calcium channels to insulin secretion in pancreatic β-cells. AJP: Endocrinology and Metabolism *297*, E717–E727.

Kamer, K.J., and Mootha, V.K. (2015). The molecular era of the mitochondrial calcium uniporter. Nat Rev Mol Cell Biol *16*, 545–553.

Kanow, M.A., Giarmarco, M.M., Jankowski, C.S.R., Tsantilas, K., Engel, A.L., Du, J., Linton, J.D., Farnsworth, C.C., Sloat, S.R., Rountree, A., et al. (2017). Biochemical adaptations of the retina and retinal pigment epithelium support a metabolic ecosystem in the vertebrate eye. eLife *6*.

Karlsson, J., Hofsten, von, J., and Olsson, P.-E. (2001). Generating Transparent Zebrafish: A Refined Method to Improve Detection of Gene Expression During Embryonic Development. Marine Biotechnology *3*, 0522–0527.

Kawamura, S., and Murakami, M. (1991). Calcium-dependent regulation of cyclic GMP phosphodiesterase by a protein from frog retinal rods. Nature *349*, 420–423.

Kennedy, B.N., Alvarez, Y., Brockerhoff, S.E., Stearns, G.W., Sapetto-Rebow, B., Taylor, M.R., and Hurley, J.B. (2007). Identification of a zebrafish cone photoreceptor-specific promoter and genetic rescue of achromatopsia in the nof mutant. Invest. Ophthalmol. Vis. Sci. *48*, 522–529.

Kim, J., Lee, E., Chang, B.S., Oh, C.S., Mun, G.H., Chung, Y.H., and Shin, D.H. (2005). The presence of megamitochondria in the ellipsoid of photoreceptor inner segment of the zebrafish retina. Anatom Histol Embryol *34*, 339–342.

Kioka, H., Kato, H., Asano, Y., Sakata, Y., and Kitakaze, M. (2014). *In vivo* visualization of ATP dynamics under hypoxia reveals that G0/G1 switch gene 2 provides ischemic tolerance through the increase of ATP production. Circulation 130:A12840.

Kirichok, Y., Krapivinsky, G., and Clapham, D.E. (2004). The mitochondrial calcium uniporter is a highly selective ion channel. Nature *427*, 360–364.

Koch, S.F., Duong, J.K., Hsu, C.-W., Tsai, Y.-T., Lin, C.-S., Wahl-Schott, C.A., and Tsang, S.H. (2017). Genetic rescue models refute nonautonomous rod cell death in retinitis pigmentosa. Proc. Natl. Acad. Sci. U.S.A. *114*, 5259–5264.

Kolko, M., Vosborg, F., Henriksen, U.L., Hasan-Olive, M.M., Diget, E.H., Vohra, R., Gurubaran, I.R.S., Gjedde, A., Mariga, S.T., Skytt, D.M., et al. (2015). Lactate transport and receptor actions in retina: potential roles in retinal function and disease. Neurochem Res *41*, 1229–1236.

Kourennyi, D.E., and Barnes, S. (2000). Depolarization-induced calcium channel facilitation in rod photoreceptors is independent of G proteins and phosphorylation. J. Neurophysiol. *84*, 133–138.

Krebs, H.A. (1927). On the metabolism of the retina. Biochemische Zeitschrift *189*, 57–59.

Krizaj, D., and Copenhagen, D.R. (1998). Compartmentalization of calcium extrusion mechanisms in the outer and inner segments of photoreceptors. Neuron *21*, 249–256.

Krizaj, D., and Copenhagen, D.R. (2002). Calcium regulation in photoreceptors. Frontiers in Bioscience: a Journal and Virtual Library *7*, d2023–d2044.

Krizaj, D., Demarco, S.J., Johnson, J., Strehler, E.E., and Copenhagen, D.R. (2002). Cell-specific expression of plasma membrane calcium ATPase isoforms in retinal neurons. J. Comp. Neurol. *451*, 1–21.

Kulkarni, M., Schubert, T., Baden, T., Wissinger, B., Euler, T., and Paquet-Durand, F. (2015). Imaging Ca^{2+} Dynamics in Cone Photoreceptor Axon Terminals of the Mouse Retina. JoVE.

Kurihara, T., Westenskow, P.D., Gantner, M.L., Usui, Y., Schultz, A., Bravo, S., Aguilar, E., Wittgrove, C., Friedlander, M.S., Paris, L.P., et al. (2016). Hypoxia-induced metabolic stress in retinal pigment epithelial cells is sufficient to induce photoreceptor degeneration. eLife *5*.

Kwan, K.M., Fujimoto, E., Grabher, C., Mangum, B.D., Hardy, M.E., Campbell, D.S., Parant, J.M., Yost, H.J., Kanki, J.P., and Chien, C.-B. (2007). The Tol2kit: A multisite gateway-based construction kit forTol2 transposon transgenesis constructs. Dev. Dyn. *236*, 3088–3099.

Kwong, R.W.M., and Perry, S.F. (2015). Hydrogen sulfide promotes calcium uptake in larval zebrafish. AJP: Cell Physiology ajpcell.00053.2015.

Laughlin, S.B., de Ruyter van Steveninck, R.R., and Anderson, J.C. (1998). The metabolic cost of neural information. Nat Neurosci *1*, 36–41.

LaVail, M.M. (1976). Rod outer segment disk shedding in rat retina: relationship to cyclic lighting. Science *194*, 1071–1074.

Lee, A., Wang, S., Williams, B., Hagen, J., Scheetz, T.E., and Haeseleer, F. (2015). Characterization of CaV1.4 complexes (α1 1.4, β2, and α2δ4) in HEK293T cells and in the retina. J. Biol. Chem. *290*, 1505–1521.

Lefevere, E., Toft-Kehler, A.K., Vohra, R., Kolko, M., Moons, L., and Van Hove, I. (2017). Mitochondrial dysfunction underlying outer retinal diseases. Mitochondrion *36*, 66–76.

Lehmann, G.L., Benedicto, I., Philp, N.J., and Rodriguez-Boulan, E. (2014). Plasma membrane protein polarity and trafficking in RPE cells: past, present and future. Exp. Eye Res. *126*, 5–15.

Lenkowski, J.R., and Raymond, P.A. (2014). Müller glia: Stem cells for generation and regeneration of retinal neurons in teleost fish. Progress in Retinal and Eye Research *40*, 94–123.

Lewis, A., Williams, P., Lawrence, O., Wong, R.O.L., and Brockerhoff, S.E. (2010). Wild-type cone photoreceptors persist despite neighboring mutant cone degeneration. J. Neurosci. *30*, 382–389.

Lieschke, G.J., and Currie, P.D. (2007). Animal models of human disease: zebrafish swim into view. Nat Rev Genet *8*, 353–367.

Lindsay, K.J., Du, J., Sloat, S.R., Contreras, L., Linton, J.D., Turner, S.J., Sadilek, M., Satrústegui, J., and Hurley, J.B. (2014). Pyruvate kinase and aspartate-glutamate carrier distributions reveal key metabolic links between neurons and glia in retina. Proc. Natl. Acad. Sci. U.S.A. *111*, 15579–15584.

Linton, J.D., Holzhausen, L.C., Babai, N., Song, H., Miyagishima, K.J., Stearns, G.W., Lindsay, K., Wei, J., Chertov, A.O., Peters, T.A., et al. (2010). Flow of energy in the outer retina in darkness and in light. Proc. Natl. Acad. Sci. U.S.A. *107*, 8599–8604.

Llorente-Folch, I., Rueda, C.B., Amigo, I., del Arco, A., Saheki, T., Pardo, B., and Satrústegui, J. (2013). Calcium-regulation of mitochondrial respiration maintains ATP homeostasis and requires ARALAR/AGC1-malate aspartate shuttle in intact cortical neurons. J. Neurosci. *33*, 13957–13971.

Lowry, O.H., Roberts, N.R., Schulz, D.W., Clow, J.E., and Clark, J.R. (1961). Quantitative histochemistry of retina. II. Enzymes of glucose metabolism. J. Biol. Chem. *236*, 2813–2820.

Lytton, J., Westlin, M., and Hanley, M.R. (1991). Thapsigargin inhibits the sarcoplasmic or endoplasmic reticulum Ca-ATPase family of calcium pumps. J. Biol. Chem. *266*, 17067–17071.

Ma, E.Y., Lewis, A., Barabas, P., Stearns, G., Suzuki, S., Krizaj, D., and Brockerhoff, S.E. (2013). Loss of Pde6 reduces cell body Ca^{2+} transients within photoreceptors. Cell Death and Disease *4*, e797.

MacAskill, A.F., Rinholm, J.E., Twelvetrees, A.E., Arancibia-Carcamo, I.L., Muir, J., Fransson, A., Aspenstrom, P., Attwell, D., and Kittler, J.T. (2009). Miro1 Is a calcium sensor for glutamate receptor-dependent localization of mitochondria at synapses. Neuron *61*, 541–555.

MacNichol, E.F., Kunz, Y.W., Levine, J.S., Hárosi, F.I., and Collins, B.A. (1978). Ellipsosomes: organelles containing a cytochrome-like pigment in the retinal cones of certain fishes. Science *200*, 549–552.

Mammucari, C., Gherardi, G., Zamparo, I., Raffaello, A., Boncompagni, S., Chemello, F., Cagnin, S., Braga, A., Zanin, S., Pallafacchina, G., et al. (2015). The mitochondrial calcium uniporter controls skeletal muscle trophism *in vivo*. Cell Reports *10*, 1269–1279.

Mantych, G.J., Hageman, G.S., and Devaskar, S.U. (1993). Characterization of glucose transporter isoforms in the adult and developing human eye. Endocrinology *133*, 600–607.

Marcu, R., Wiczer, B.M., Neeley, C.K., and Hawkins, B.J. (2014). Mitochondrial matrix Ca^{2+} accumulation regulates cytosolic NAD^+/NADH metabolism, protein acetylation, and sirtuin expression. Molecular and Cellular Biology *34*, 2890–2902.

Masuda, T., Wada, Y., and Kawamura, S. (2016). ES1 is a mitochondrial enlarging factor contributing to form mega-mitochondria in zebrafish cones. Sci Rep *6*, 22360.

Matlib, M.A., Zhou, Z., Knight, S., Ahmed, S., and Choi, K.M. (1998). Oxygen-bridged dinuclear ruthenium amine complex specifically inhibits Ca^{2+} uptake into mitochondria in vitro and in situ in single cardiac myocytes. J. Biol. Chem. *273*, 10223–10231.

Matschinsky, F.M., Passonneau, J.V., and Lowry, O.H. (1968). Quantitative histochemical analysis of glycolytic intermediates and cofactors with an oil well technique. J. Histochem. Cytochem. *16*, 29–39.

Mattapallil, M.J., Wawrousek, E.F., Chan, C.-C., Zhao, H., Roychoudhury, J., Ferguson, T.A., and Caspi, R.R. (2012). The Rd8 mutation of the Crb1 gene is present in vendor lines of C57BL/6N mice and embryonic stem cells, and confounds ocular induced mutant phenotypes. Invest. Ophthalmol. Vis. Sci. *53*, 2921–2927.

Medrano, C.J., and Fox, D.A. (1995). Oxygen consumption in the rat outer and inner retina: light- and pharmacologically-induced inhibition. Exp. Eye Res. *61*, 273–284.

Mercurio, A.M., and Holtzman, E. (1982). Smooth endoplasmic reticulum and other agranular reticulum in frog retinal photoreceptors. J. Neurocytol. *11*, 263–293.

Metallo, C.M., Walther, J.L., and Stephanopoulos, G. (2009). Evaluation of ^{13}C isotopic tracers for metabolic flux analysis in mammalian cells. Journal of Biotechnology *144*, 167–174.

Morgan, J.L., Dhingra, A., Vardi, N., and Wong, R.O.L. (2006). Axons and dendrites originate from neuroepithelial-like processes of retinal bipolar cells. Nat Neurosci *9*, 85–92.

Mullen, R.J., and LaVail, M.M. (1976). Inherited retinal dystrophy: primary defect in pigment epithelium determined with experimental rat chimeras. Science *192*, 799–801.

Murgia, M., and Rizzuto, R. (2015). Molecular diversity and pleiotropic role of the mitochondrial calcium uniporter. Cell Calcium *58*, 11–17.

Muto, A., Ohkura, M., Abe, G., Nakai, J., and Kawakami, K. (2013). Real-time visualization of neuronal activity during perception. Current Biology *23*, 307–311.

Nag, T.C., and Wadhwa, S. (2016). Immunolocalisation pattern of complex I-V in ageing human retina: Correlation with mitochondrial ultrastructure. Mitochondrion. *31*, 20–32.

Nashine, S.R., Cohen, P., Chwa, M., Lu, S., Nesburn, A.B., Kuppermann, B.D., and Kenney, M.C. (2017). Humanin G (HNG) protects age-related macular degeneration (AMD) transmitochondrial ARPE-19 cybrids from mitochondrial and cellular damage. Cell Death and Disease 1–12.

Neuhauss, S.C.F. (2002). Behavioral genetic approaches to visual system development and function in zebrafish. J. Neurobiol. *54*, 148–160.

Niethammer, P., Grabher, C., Look, A.T., and Mitchison, T.J. (2009). A tissue-scale gradient of hydrogen peroxide mediates rapid wound detection in zebrafish. Nature *459*, 996–999.

Nihira, M., Anderson, K., Gorin, F.A., and Burns, M.S. (1995). Primate rod and cone photoreceptors may differ in glucose accessibility. Invest. Ophthalmol. Vis. Sci. *36*, 1259–1270.

Okawa, H., Sampath, A.P., Laughlin, S.B., and Fain, G.L. (2008). ATP consumption by mammalian rod photoreceptors in darkness and in light. Curr. Biol. *18*, 1917–1921.

Orrenius, S., Zhivotovsky, B., and Nicotera, P. (2003). Calcium: Regulation of cell death: the calcium–apoptosis link. Nat Rev Mol Cell Biol *4*, 552–565.

Paillard, M., Csordás, G., Szanda, G., Golenár, T., Debattisti, V., Bartok, A., Wang, N., Moffat, C., Seifert, E.L., Spät, A., et al. (2017). Tissue-Specific Mitochondrial Decoding of Cytoplasmic Ca. Cell Reports *18*, 2291–2300.

Pan, X., Liu, J., Nguyen, T., Liu, C., Sun, J., Teng, Y., Fergusson, M.M., Rovira, I.I., Allen, M., Springer, D.A., et al. (2013). The physiological role of mitochondrial calcium

revealed by mice lacking the mitochondrial calcium uniporter. Nat Cell Biol *15*, 1464–1472.

Perkins, G.A., Tjong, J., Brown, J.M., Poquiz, P.H., Scott, R.T., Kolson, D.R., Ellisman, M.H., and Spirou, G.A. (2010). The Micro-Architecture of Mitochondria at Active Zones: Electron Tomography Reveals Novel Anchoring Scaffolds and Cristae Structured for High-Rate Metabolism. J. Neurosci. *30*, 1015–1026.

Perkins, G.A., Ellisman, M.H., and Fox, D.A. (2003). Three-dimensional analysis of mouse rod and cone mitochondrial cristae architecture: bioenergetic and functional implications. Molecular Vision *9*, 60–73.

Perkins, G.A., Ellisman, M.H., and Fox, D.A. (2004). The structure–function correlates of mammalian rod and cone photoreceptor mitochondria: observations and unanswered questions. Mitochondrion *4*, 695–703.

Phelan, J.K., and Bok, D. (2000). A brief review of retinitis pigmentosa and the identified retinitis pigmentosa genes. Molecular Vision *6*, 116–124.

Philp, N.J., Yoon, H., and Grollman, E.F. (1998). Monocarboxylate transporter MCT1 is located in the apical membrane and MCT3 in the basal membrane of rat RPE. Am. J. Physiol. *274*, R1824–R1828.

Poitry-Yamate, C.L., Poitry, S., and Tsacopoulos, M. (1995). Lactate released by Muller glial cells is metabolized by photoreceptors from mammalian retina. J. Neurosci. *15*, 5179–5191.

Punzo, C., Kornacker, K., and Cepko, C.L. (2009). Stimulation of the insulin/mTOR pathway delays cone death in a mouse model of retinitis pigmentosa. Nat Neurosci *12*, 44–52.

Punzo, C., Xiong, W., and Cepko, C.L. (2012). Loss of daylight vision in retinal degeneration: Are oxidative stress and metabolic dysregulation to blame? J. Biol. Chem. *287*, 1642–1648.

Qi, H., Li, L., and Shuai, J. (2015). Optimal microdomain crosstalk between endoplasmic reticulum and mitochondria for Ca^{2+} oscillations. Sci Rep *5*, 7984.

Qiu, J., Tan, Y.-W., Hagenston, A.M., Martel, M.-A., Kneisel, N., Skehel, P.A., Wyllie, D.J.A., Bading, H., and Hardingham, G.E. (2013). Mitochondrial calcium uniporter MCU controls excitotoxicity and is transcriptionally repressed by neuroprotective nuclear calcium signals. Nat Comms *4*.

Rajala, R.V.S., Rajala, A., Kooker, C., Wang, Y., and Anderson, R.E. (2016). The Warburg effect mediator pyruvate kinase M2 expression and regulation in the retina. Sci Rep *6*, 37727.

Rattner, A., Sun, H., and Nathans, J. (1999). Molecular genetics of human retinal

disease. Annu. Rev. Genet. *33*, 89–131.

Raymond, P.A., Colvin, S.M., Jabeen, Z., Nagashima, M., Barthel, L.K., Hadidjojo, J., Popova, L., Pejaver, V.R., and Lubensky, D.K. (2014). Patterning the cone mosaic array in zebrafish retina requires specification of ultraviolet-sensitive cones. PLoS ONE *9*, e85325.

Reyes-Reveles, J., Dhingra, A., Alexander, D., Bragin, A., Philp, N.J., and Boesze-Battaglia, K. (2017). Phagocytosis-dependent ketogenesis in retinal pigment epithelium. J. Biol. Chem. *292*, 8038–8047.

Rieke, F., and Schwartz, E.A. (1996). Asynchronous transmitter release: control of exocytosis and endocytosis at the salamander rod synapse. The Journal of Physiology *493.1*, 1–8.

Riepe, R.E., and Norenburg, M.D. (1977). Müller cell localisation of glutamine synthetase in rat retina. Nature *268*, 654–655.

Rizzolo, L.J. (2008). Glucose Transporters in Retinal Pigment Epithelium Development *Ocular Transporters in Ophthalmic Diseases and Drug Delivery*. (Humana Press)

Rowland, A.A., and Voeltz, G.K. (2012). Endoplasmic reticulum–mitochondria contacts: function of the junction. Nat Rev Mol Cell Biol *13*, 607–615.

Rueda, E.M., Johnson, J.E., Giddabasappa, A., Swaroop, A., Brooks, M.J., Sigel, I., Chaney, S.Y., and Fox, D.A. (2016). The cellular and compartmental profile of mouse retinal glycolysis, tricarboxylic acid cycle, oxidative phosphorylation, and ~P transferring kinases. Molecular Vision *22*, 847–885.

Rutter, G.A., and Pinton, P. (2014). Mitochondria-associated endoplasmic reticulum membranes in insulin signaling. Diabetes *63*, 3163–3165.

Sakurai, K., Vinberg, F., Wang, T., Chen, J., and Kefalov, V.J. (2016). The Na^+/Ca^{2+}, K^+ exchanger 2 modulates mammalian cone phototransduction. Sci Rep *6*, 32521.

Sampath, A.P., Matthews, H.R., Cornwall, M.C., Bandarchi, J., and Fain, G.L. (1999). Light-dependent changes in outer segment free-Ca^{2+} concentration in salamander cone photoreceptors. J. Gen. Physiol. *113*, 267–277.

SanGiovanni, J.P., Arking, D.E., Iyengar, S.K., Elashoff, M., Clemons, T.E., Reed, G.F., Henning, A.K., Sivakumaran, T.A., Xu, X., DeWan, A., et al. (2009). Mitochondrial DNA Variants of Respiratory Complex I that Uniquely Characterize Haplogroup T2 Are Associated with Increased Risk of Age-Related Macular Degeneration. PLoS ONE *4*, e5508.

Santos, L.R.B., Muller, C., de Souza, A.H., Takahashi, H.K., Spégel, P., Sweet, I.R., Chae, H., Mulder, H., and Jonas, J.-C. (2017). NNT reverse mode of operation mediates glucose control of mitochondrial NADPH and glutathione redox state in mouse

pancreatic. Molecular Metabolism *6*, 535–547.

Satrústegui, J., Contreras, L., Ramos, M., Marmol, P., del Arco, A., Saheki, T., and Pardo, B. (2007). Role of aralar, the mitochondrial transporter of aspartate-glutamate, in brain N-acetylaspartate formation and Ca^{2+} signaling in neuronal mitochondria. J. Neurosci. Res. *85*, 3359–3366.

Scharfe, C., Lu, H.H.-S., Neuenburg, J.K., Allen, E.A., Li, G.-C., Klopstock, T., Cowan, T.M., Enns, G.M., and Davis, R.W. (2009). Mapping Gene Associations in Human Mitochondria using Clinical Disease Phenotypes. PLoS Comp Biol *5*, e1000374.

Schmitt, K., Grimm, A., Dallmann, R., Oettinghaus, B., Restelli, L.M., Witzig, M., Ishihara, N., Mihara, K., Ripperger, J.A., Albrecht, U., et al. (2018). Circadian Control of DRP1 Activity Regulates Mitochondrial Dynamics and Bioenergetics. Cell Metabolism 1–16.

Schmitz, F. (2014). Presynaptic [Ca^{2+}] and GCAPs: aspects on the structure and function of photoreceptor ribbon synapses. Front Mol Neurosci *7*, 3.

Schnetkamp, P.P., Szerencsei, R.T., and Basu, D.K. (1991). Unidirectional Na^+, Ca^{2+}, and K^+ fluxes through the bovine rod outer segment Na-Ca-K exchanger. J. Biol. Chem. *266*, 198–206.

Schon, E.A., DiMauro, S., and Hirano, M. (2012). Human mitochondrial DNA: roles of inherited and somatic mutations. Nat Rev Genet *13*, 878–890.

Senanayake, P.D., Calabro, A., Hu, J.G., Bonilha, V.L., Darr, A., Bok, D., and Hollyfield, J.G. (2006). Glucose utilization by the retinal pigment epithelium: Evidence for rapid uptake and storage in glycogen, followed by glycogen utilization. Exp. Eye Res. *83*, 235–246.

Sengillo, J., Justus, S., Cabral, T., and Tsang, S. (2017). Correction of Monogenic and Common Retinal Disorders with Gene Therapy. Genes *8*, 53.

Shin, J., Chen, J., and Solnica-Krezel, L. (2014). Efficient homologous recombination-mediated genome engineering in zebrafish using TALE nucleases. Development *141*, 3807–3818.

Sloat, S.R., Jankowski, C., Hutto, R., Giarmarco, M., Cleghorn, W., Shandar, G., Brockerhoff, S.E., and Hurley, J.B. (2016). Quantification of Mitochondrial Structure in Photoreceptors. Invest. Ophthalmol. Vis. Sci. *57*, 566.

Sonoda, S., Spee, C., Barron, E., Ryan, S.J., Kannan, R., and Hinton, D.R. (2009). A protocol for the culture and differentiation of highly polarized human retinal pigment epithelial cells. Nature Protocols *4*, 662–673.

Stearns, G., Evangelista, M., Fadool, J.M., and Brockerhoff, S.E. (2007). A mutation in the cone-specific pde6 gene causes rapid cone photoreceptor degeneration in

zebrafish. J. Neurosci. *27*, 13866–13874.

Stewart, A.M., Braubach, O., Spitsbergen, J., Gerlai, R., and Kalueff, A.V. (2014). Zebrafish models for translational neuroscience research: from tank to bedside. Trends in Neurosciences *37*, 264–278.

Strauss, O. (1995). The Retinal Pigment Epithelium. In The Retinal Pigment Epithelium, (Salt Lake City (UT): Webvision: The Organization of the Retina and Visual System).

Szikra, T., and Krizaj, D. (2007). Intracellular organelles and calcium homeostasis in rods and cones. Vis. Neurosci. *24*, 1–11.

Takagi, H., Tanihara, H., Seino, Y., and Yoshimura, N. (1994). Characterization of glucose transporter in cultured human retinal pigment epithelial cells: gene expression and effect of growth factors. Invest. Ophthalmol. Vis. Sci. *35*, 170–177.

Tarboush, R., Chapman, G.B., and Connaughton, V.P. (2012). Ultrastructure of the distal retina of the adult zebrafish, Danio rerio. Tissue and Cell *44*, 264–279.

Tarboush, R., Novales Flamarique, I., Chapman, G.B., and Connaughton, V.P. (2014). Variability in mitochondria of zebrafish photoreceptor ellipsoids. Vis. Neurosci. *31*, 11–23.

Taylor, W.R., and Morgans, C. (1998). Localization and properties of voltage-gated calcium channels in cone photoreceptors of Tupaia belangeri. Vis. Neurosci. *15*, 541–552.

Terluk, M.R., Kapphahn, R.J., Soukup, L.M., Gong, H., Gallardo, C., Montezuma, S.R., and Ferrington, D.A. (2015). Investigating mitochondria as a target for treating age-related macular degeneration. J. Neurosci. *35*, 7304–7311.

Thoreson, W.B., Rabl, K., Townes-Anderson, E., and Heidelberger, R. (2004). A highly Ca^{2+}-sensitive pool of vesicles contributes to linearity at the rod photoreceptor ribbon synapse. Neuron *42*, 595–605.

Tomar, D., Dong, Z., Shanmughapriya, S., Koch, D.A., Thomas, T., Hoffman, N.E., Timbalia, S.A., Goldman, S.J., Breves, S.L., Corbally, D.P., et al. (2016). MCUR1 Is a Scaffold Factor for the MCU Complex Function and Promotes Mitochondrial Bioenergetics. Cell Reports *15*, 1673–1685.

Toomey, M.B., and Corbo, J.C. (2017). Evolution, Development and Function of Vertebrate Cone Oil Droplets. Front. Neural Circuits *11*, 793.

Törnquist, P., Alm, A., and Bill, A. (1990). Permeability of ocular vessels and transport across the blood-retinal-barrier. Eye (Lond) *4 (Pt 2)*, 303–309.

Tsuyama, T., Kishikawa, J.-I., Han, Y.-W., Harada, Y., Tsubouchi, A., Noji, H., Kakizuka, A., Yokoyama, K., Uemura, T., and Imamura, H. (2013). In vivo fluorescent

adenosine 5'-triphosphate (ATP) imaging of Drosophila melanogaster and Caenorhabditis elegans by using a genetically encoded fluorescent ATP biosensor optimized for low temperatures. Anal. Chem. *85*, 7889–7896.

Uckermann, O., Iandiev, I., Francke, M., Franze, K., Grosche, J., Wolf, S., Kohen, L., Wiedemann, P., Reichenbach, A., and Bringmann, A. (2003). Selective staining by vital dyes of Müller glial cells in retinal wholemounts. Glia *45*, 59–66.

Uhlén, M., Fagerberg, L., Hallström, B.M., Lindskog, C., Oksvold, P., Mardinoglu, A., Sivertsson, Å., Kampf, C., Sjöstedt, E., Asplund, A., et al. (2015). Proteomics. Tissue-based map of the human proteome. Science *347*, 1260419–1260419.

Van Hook, M.J., and Thoreson, W.B. (2013). Simultaneous whole-cell recordings from photoreceptors and second-order neurons in an amphibian retinal slice preparation. JoVE.

Van Hook, M.J., and Thoreson, W.B. (2014). Endogenous calcium buffering at photoreceptor synaptic terminals in salamander retina. Synapse *68*, 518–528.

Vecino, E., Rodriguez, F.D., Ruzafa, N., Pereiro, X., and Sharma, S.C. (2015). Progress in Retinal and Eye Research. Progress in Retinal and Eye Research 1–39.

Venkatesh, A., Ma, S., Le, Y.Z., Hall, M.N., Rüegg, M.A., and Punzo, C. (2015). Activated mTORC1 promotes long-term cone survival in retinitis pigmentosa mice. J. Clin. Invest. *125*, 1446–1458.

Vinberg, F., Kolesnikov, A.V., and Kefalov, V.J. (2014). *Ex vivo* ERG analysis of photoreceptors using an *in vivo* ERG system. Vision Res. *101*, 108–117.

Vinberg, F., Wang, T., Molday, R.S., Chen, J., and Kefalov, V.J. (2015). A new mouse model for stationary night blindness with mutant Slc24a1 explains the pathophysiology of the associated human disease. Human Molecular Genetics *24*, 5915–5929.

Wacharasint, P., Nakada, T.-A., Boyd, J.H., Russell, J.A., and Walley, K.R. (2012). Normal-range blood lactate concentration in septic shock is prognostic and predictive. Shock *38*, 4–10.

Wan, B., LaNoue, K.F., Cheung, J.Y., and Scaduto, R.C. (1989). Regulation of citric acid cycle by calcium. J. Biol. Chem. *264*, 13430–13439.

Wang, C., Xie, N., Wang, Y., Li, Y., Ge, X., and Wang, M. (2015). Role of the mitochondrial calcium uniporter in rat hippocampal neuronal death after pilocarpine-induced status epilepticus. Neurochem Res *40*, 1739–1746.

Wang, L., Törnquist, P., and Bill, A. (1997a). Glucose metabolism in pig outer retina in light and darkness. Acta Physiologica Scandinavica *160*, 75–81.

Wang, L., Törnquist, P., and Bill, A. (1997b). Glucose metabolism of the inner retina in

pigs in darkness and light. Acta Physiologica Scandinavica *160*, 71–74.

Wang, T.-M., Holzhausen, L.C., and Kramer, R.H. (2014). Imaging an optogenetic pH sensor reveals that protons mediate lateral inhibition in the retina. Nat Neurosci *17*, 262–268.

Wang, W., Fang, H., Groom, L., Cheng, A., Zhang, W., Liu, J., Wang, X., Li, K., Han, P., Zheng, M., et al. (2008). Superoxide flashes in single mitochondria. Cell *134*, 279–290.

Wang, W., Lee, S.J., Scott, P.A., Lu, X., Emery, D., Liu, Y., Ezashi, T., Roberts, M.R., Ross, J.W., Kaplan, H.J., et al. (2016). Two-Step Reactivation of Dormant Cones in Retinitis Pigmentosa. Cell Reports *15*, 372–385.

Warburg, O., Posener, K., and Negrelein, E. (1924). The metabolism of carcinoma cells. Bioschemische Zeitschrift *152*, 309–344.

Wei, H., Xun, Z., Granado, H., Wu, A., and Handa, J.T. (2016). An easy, rapid method to isolate RPE cell protein from the mouse eye. Exp. Eye Res. *145*, 450–455.

Wiczer, B.M., Marcu, R., and Hawkins, B.J. (2014). KB-R7943, a plasma membrane Na^+/Ca^{2+} exchanger inhibitor, blocks opening of the mitochondrial permeability transition pore. Biochemical and Biophysical Research Communications *444*, 44–49.

Williams, G.S.B., Boyman, L., Chikando, A.C., Khairallah, R.J., and Lederer, W.J. (2013). Mitochondrial calcium uptake. Proc. Natl. Acad. Sci. U.S.A. *110*, 10479–10486.

Winkler, B.S. (1981). Glycolytic and oxidative metabolism in relation to retinal function. J. Gen. Physiol. *77*, 667–692.

Winkler, B.S., Starnes, C.A., Twardy, B.S., Brault, D., and Taylor, R.C. (2008). Nuclear Magnetic Resonance and Biochemical Measurements of Glucose Utilization in the Cone-Dominant Ground Squirrel Retina. Invest. Ophthalmol. Vis. Sci. *49*, 4613.

Wohl, S.G., and Reh, T.A. (2016). The microRNA expression profile of mouse Müller glia. Sci Rep 1–13.

Yang, H.H., St-Pierre, F., Sun, X., Ding, X., and Lin, M.Z. (2016). Subcellular imaging of voltage and calcium signals reveals neural processing *in vivo*. Cell *166*, 1–13.

Yoshioka, K., Takahashi, H., Homma, T., Saito, M., Oh, K.B., Nemoto, Y., and Matsuoka, H. (1996). A novel fluorescent derivative of glucose applicable to the assessment of glucose uptake activity of Escherichia coli. Biochim. Biophys. Acta *1289*, 5–9.

Zhang, L., Du, J., Justus, S., Hsu, C.-W., Bonet-Ponce, L., Wu, W.-H., Tsai, Y.-T., Wu, W.-P., Jia, Y., Duong, J.K., et al. (2016). Reprogramming metabolism by targeting sirtuin 6 attenuates retinal degeneration. J. Clin. Invest. *126*, 4659–4673.

Zhang, X., Feng, Q., and Cote, R.H. (2005). Efficacy and selectivity of phosphodiesterase-targeted drugs in inhibiting photoreceptor phosphodiesterase (PDE6) in retinal photoreceptors. Invest Ophthalmol *46*, 3060–3066.

Zhao, C., Yasumura, D., Li, X., Matthes, M., Lloyd, M., Nielsen, G., Ahern, K., Snyder, M., Bok, D., Dunaief, J.L., et al. (2011a). mTOR-mediated dedifferentiation of the retinal pigment epithelium initiates photoreceptor degeneration in mice. J. Clin. Invest. *121*, 369–383.

Zhao, Y., Araki, S., Wu, J., Teramoto, T., Chang, Y.-F., Nakano, M., Abdelfattah, A.S., Fujiwara, M., Ishihara, T., Nagai, T., et al. (2011b). An expanded palette of genetically encoded Ca^{2+} indicators. Science *333*, 1888–1891.

Zhao, Y., and Yang, Y. (2015). Profiling metabolic states with genetically encoded fluorescent biosensors for NADH. Current Opinion in Biotechnology *31*, 86–92.

Zou, S.-Q., Yin, W., Zhang, M.-J., Hu, C.-R., Huang, Y.-B., and Hu, B. (2010). Using the optokinetic response to study visual function of zebrafish. JoVE.